Check for updates

Synthetic routes of clean hydrocarbons fuels and oxygenates by catalytic conversions of carbon oxides

Hyun Seung Jung [a,b,1], Byeong Gi Kim [a,1], Jong Wook Bae [a,*]

[a] School of Chemical Engineering, Sungkyunkwan University (SKKU), Seobu-ro 2066, Suwon, Gyeonggi-do, 16419, Republic of Korea
[b] Department of Chemistry, Northwestern University, 2145 Sheridan Road, Evanston, IL 60208, United States

ARTICLE INFO

ABSTRACT

The emission controls of carbon oxides (CO_x) are crucial to fulfill carbon neutrality, where CO_x is a useful building block for chemical synthesis. Therefore, CO_x conversions have been intensively investigated to reduce carbon emissions and to produce alternative fuels such as dimethyl ether, C_{5+} higher hydrocarbons, and higher alcohols by using heterogeneous catalysts. There are lots of advantages in catalytic conversion strategies, which can be largely affected by reaction conditions and types of catalysts. In the paper, catalytic activities and reaction mechanisms of CO_x conversions are briefly summarized to elucidate recent progresses of various catalytic reactions. Furthermore, the strategies to improve catalytic activity and stability as well as adjustments of final products selectivity are summarized. Various tandem reactions with well-designed hybridized catalysts to efficiently utilize CO/CO_2 containing syngas are summarized to explain recent synthetic strategies for the productions of value-added hydrocarbon fuels and oxygenates by using environmentally benign catalytic processes.

1. Introduction

Due to severe global warming problems, net zero emission of greenhouse gases (GHG) has been largely investigated through carbon capture and utilization (CCU) based on C1 chemistry. GHG such as carbon dioxide (CO_2) and methane (CH_4) can be generated by incomplete combustion of hydrocarbons which are required to be properly removed for environmental preservations. For the combustion processes, carbon monoxide (CO) can be also generated and it should be removed due to its toxicity [1–3]. Meanwhile, the conversions of CO/CO_2 (CO_x, carbon oxides), which are generally contained in synthetic gas (syngas) with hydrogen (H_2), have been largely studied to produce value-added petrochemicals involving methanol (MeOH), ethanol (EtOH), dimethyl ether (DME), heavier hydrocarbons and higher alcohols through electrocatalysis, photocatalysis as well as thermocatalysis and so on [1–6]. Recently, various electrocatalysts and photocatalysts have been developed to utilize CO_x by CO_2 electrolysis to form CO/formic acid/C_{2+} products or photocatalytic CO_x conversion. Even though the present photocatalysts and electrocatalysts can produce higher alcohols and heavier hydrocarbons, however, the commercialization strategies of the productions of higher alcohols or heavier

hydrocarbons by electrocatalysis and photocatalysis should be more investigated [3–6]. For the electrocatalysts, non-noble metal-based catalysts have been required to have sufficient faradaic efficiency (selectivity) and current density for industrial applications with efficient and scalable electrodes, membrane, electrolyte and cell architectures. For the photocatalysts, redox potential and stability should be properly considered and it is desirable to operate photocatalytic systems by visible light because only about 5% of solar light can be derived from UV and visible light. Therefore, various factors for the utilization of electrocatalysis as well as photocatalysis systems are still required to progress with an easy scalability and commercialization [7–11].

However, traditional thermocatalysts are more appropriate to produce various petroproducts and the thermocatalysis has been welldeveloped for the commercialization such as stream reforming of methane (SRM), water gas shift (WGS) reaction or Fischer-Tropsch synthesis (FTS) reaction [12–14]. In addition, CO_x as useful platform chemicals can be converted into various chemicals and fuels such as gasoline-range hydrocarbons and oxygenates including ethanol and higher alcohols, which are regarded as one of the promising alternative fuels owing to smaller pollutant emissions with high octane number by revealing more economically feasible and environmentally friendly

processes [15,16]. Especially, ethanol has been widely utilized as an alternative fuel additive in several countries with higher demand, and higher hydrocarbons ad oxygenates are also regarded as important fuels [15–22]. Therefore, in the present review, the diverse CO/CO_2 conversions routes to ethanol, heavier hydrocarbons and higher alcohols are summarized to show recent research trends.

Since there are lots of possible reaction routes for CO/CO_2 conversions to hydrocarbons and oxygenates [17–24], the selection of proper reaction conditions and types of catalysts are crucial to enhance the productivity of desired petrochemical intermediates. For example, ethanol by thermocatalysis can be selectively produced via various indirect methods or synthesized with other mixed alcohols directly [24]. One indirect synthesis route is following by CO/CO_2 hydrogenation to methanol production and its successive dehydration to dimethyl ether (DME) [25–28], where the DME is known as solvent or clean fuel with non-toxic and non-carcinogenic character. The formed DME can be further transformed to methyl acetate (MA) intermediate, which can be subjected to hydrogenation for ethanol synthesis with its higher yield above 35 C-mol% based on CO conversion [29]. In addition, CO/CO_2 can be directly converted into mixed alcohols with various higher alcohols on heterogeneous catalysts, where the syngas conversion to ethanol can be also carried out with homogeneous catalytic system, however, heterogeneous catalysts showed higher production rate of C_3-C_4 alcohols [30,31]. The C_2-C_5 alcohols including ethanol are useful alternative fuel and solvent, however, the syntheses of C_{2+} higher alcohols by direct CO/CO_2 hydrogenation have been still not well-developed because of its difficult selectivity control to specific alcohols [30–33]. On the other hands, heavier hydrocarbons as clean fuels can be produced by CO/CO_2 hydrogenation by FTS reaction, and the FTS reaction is composed of CO/CO_2 hydrogenation and (reverse) water gas shift reaction ((R)WGS) by altering product distributions, where the roles of heterogeneous catalysts are important to determine the reaction pathways and to maximize catalytic activity with narrow hydrocarbons distributions [21,34–36].

Therefore, the present review paper is briefly to introduce recently reported catalytic systems with their typical reaction conditions for the conversions of CO_x into alternative fuels and value-added chemicals. Furthermore, the activities of those catalysts are also summarized in the view of single or tandem reactions, where the tandem reactions are regarded as advanced technology to maximize process efficiency and selectivity toward desirable products.

2. Indirect CO_x hydrogenation for selective production of ethanol by multistep reactions

CO_x hydrogenation to produce value-added fuels and petrochemicals has been widely studied due to the increasing demands for alternative feedstocks and CO_2 reduction even though those thermo-catalytic conversions of the thermodynamically stable CO_2 are still challenging reactions [4,18]. In addition, the carbon oxides, which have been largely produced from petrochemical industries, can be converted into ethanol via direct or indirect conversion pathways, which is a promising alternative clean fuel or petrochemical intermediate. The demand for ethanol production is getting increased because many countries are urged to use ethanol as a fuel additive to reduce fossil fuel usage, where the ethanol is usually produced by biomass-based fermentation technologies. Furthermore, the ethanol can be also produced by using CO_x conversions, which are highly required in terms of the production of carbon net-zero ethanol product [1,22]. Therefore, the direct or indirect cascade tandemly-coupled reactions for selective ethanol production is briefly summarized in the following section, which are mainly carried out by CO_x hydrogenation or multistep cascade reactions with various chemical intermediates such as methanol, dimethyl ether (DME), methyl acetate (MA), acetic acid (AA) or dimethyl oxalate (DMO) and so on [17–29].

Lots of indirect pathways for conversion of CO/CO_2 to ethanol have

been intensively studied, and some important thermocatalytic pathways through indirect cascade reaction for selective production of ethanol via intermediate-mediated routes such as methyl acetate (MA), dimethyl oxalate (DMO) or acetic acid (AcOH or AA) with their characteristics of catalysts and activities are briefly summarized in Tables 1–4 and the reaction schemes are displayed in Fig. 1. In case of the MA-mediated route (syngas → DME → MA → ethanol), CO_x containing syngas can be converted to DME followed by a gas-phase DME carbonylation to MA, which is transformed to ethanol by successive hydrogenation [21–29]. The indirect ethanol synthesis route can start from syngas conversion to DME which is also composed of two-step reactions of CO/CO_2 hydrogenation to methanol and its dehydration to DME [21,22,26–28,37,38].

2.1. CO_x conversions to methanol

For CO_2 hydrogenation, many Cu-based catalysts have been largely studied with well-developed processes. For example, methanol production from CO_2 emission plants was initiated in Iceland, and "Mitsui Chemicals Inc." in Japan reported to produce ~100 metric tons of methanol per year by CO_2 hydrogenation. In addition, the "Korea Institute of Science and Technology (KIST)" and "Dalian Institute of Chemical Physics (DICP)" in China developed the plants for CO_2 hydrogenation to methanol, where DICP also reported to produce 1500 tons of methanol per year by using ZnO-ZrO_2-based catalysts. The DICP also established an indirect ethanol production from coal via syngas/DME/MA route. Although the processes for methanol and ethanol synthesis from syngas (CO or CO_2) have been well-developed, those processes are getting important owing to its carbon net-zero emissions which are still crucial to utilize CO_2 properly with carbon neutrality [18,33,39]. In addition, Shanghai Advanced Research Institute (SARI) reported an industrial demonstration of methanol production by CO_2 hydrogenation with 5000 tons of methanol per year for 2400 h by using LDH-derived Cu catalysts [39,40]. Therefore, CO_2 hydrogenation over Cu-based catalysts seems to be quite mature technology, however, it is still difficult to improve catalytic activity and stability due to a facile sintering nature of Cu species under higher temperatures (> 300 °C). Moreover, the Cu nanoparticles can also promote WGS-RWGS side reactions. Although the Cu-based catalysts showed higher CO_x conversion, methanol selectivity is decreased along with an increase of reaction temperature due to an enhanced RWGS reaction with a fast catalyst deactivation by water formed [41,42]. Recently, zirconium oxide-based supports were utilized for methanol synthesis and ZnO-ZrO_2 mixed metal oxides as solid solution catalyst as shown in Fig. 2A were suggested to overcome the limitations of monometal oxides of ZnO and ZrO_2 because the catalytic activity of ZnO-ZrO_2 was found to be much superior. Especially, on the ZnO-ZrO_2 with $Zn/(Zn+Zr)$ molar ratio of 0.13, the catalytic activity and stability were maximized with CO_2 conversion of 10% and methanol selectivity of 86–91%. In addition, the ZnO-ZrO_2 was found to be much more stable than $Cu/ZnO/Al_2O_3$, which revealed stable CO_2 hydrogenation activity to methanol for 500 h on stream without deactivation. The synergetic effects of the solid solution of ZnO-ZrO_2 were conducive to improve CO_2 hydrogenation ability, where the formate intermediates could be hydrogenated to methanol over ZnO-ZrO_2 catalyst, however, it was not clearly confirmed up to date that formate was the major active intermediate [43]. The ZrO_2 was also used to prepare $MZrOx$ (M = Cd or Ga) by coprecipitation method, and 11.5%M such as $CdZrOx$ and $GaZrOx$ were found to be optimum catalysts. The positive effects of Cd or Ga metal oxides and ZrO_2 were to increase heterolytic H_2 dissociation by enhancing catalytic activity and methanol selectivity as unraveled by DFT computation [44].

In addition, the In_2O_3 metal oxides were also applied for the methanol synthesis by CO_2 hydrogenation as promising catalyst on account of the creation of oxygen vacant sites. For example, the In_2O_3 (9 wt%In) supported on ZnO_2, denotated as In_2O_3/ZrO_2 with highly crystalline structures (Fig. 2B-1), showed a higher methanol selectivity of 99.8% at CO_2 conversion of 5.2% (0.295 $g_{Methanol}h^{-1}g_{cat}^{-1}$). The formations of

Table 1

Summarized catalytic activities and reaction conditions for methanol or DME synthesis by CO/CO$_2$ hydrogenation.

Catalyst	Preparation method	Conversion (CO/CO$_2$)	Selectivity and yield (STY)	Reaction conditions	Reference
13% ZnO-ZrO$_2$	Coprecipitation +wet impregnation	10% (CO$_2$)	86 – 91% (methanol)	315 – 320 °C, 5.0 MPa, 24,000 mL/(g·h), H$_2$/CO$_2$ = 3:1 or 4:1	[43]
11.5% CdZrO$_x$ 11.5% GaZrO$_x$	Coprecipitation	4.3 – 12.4% (CO$_2$)	80% (methanol)	300 °C, 5.0 MPa, 24,000 h^{-1}, H$_2$/CO$_2$ = 3/1	[44]
In$_2$O$_3$/ZrO$_2$ (9 wt % In)	Precipitation + impregnation	5.2% (CO$_2$)	99.8% (methanol)	300 °C, 5.0 MPa, 16,000 h^{-1}, H$_2$/CO$_2$ = 4/1	[45]
h-In$_2$O$_3$-R	Precipitation	17.6% (CO$_2$)	92.4% (methanol)	300 °C, 5.0 MPa, 9000 mL/(g·h), H$_2$/CO$_2$ = 6	[46]
In$_2$O$_3$/m-ZrO$_2$	Precipitation + wet impregnation	4.8% (CO$_2$)	84% (methanol) 4.44 g$_{methanol}$ /(h·g$_{In}$) (STY$_{Methanol}$)`	280 °C, 5.0 MPa, 24,000 cm^3/(h·g$_{cat}$), H$_2$: CO$_2$ = 4	[47]
Cu/m-GaAl Cu/m-ZnAl Cu/m-Al	evaporation-induced self-assembly (EISA)	23.4% (CO$_2$) 24.5% (CO$_2$) 22.0% (CO$_2$)	41.2% (methanol) / 11.9% (DME) 45.2% (methanol) / 13.2% (DME) 38.9% (methanol) / 12.6% (DME)	250 °C, 5.0 MPa, H$_2$/CO$_2$ = 3, SV = 2000 L/(kg$_{cat}$•h)	[48]
CZM(20)/γ-Al$_2$O$_3$	Coprecipitation + physical mixing	37% (CO)	83% (DME)	260 °C, 3.0 MPa, 2000 mL/(g$_{cat}$•h), H$_2$/CO = 1.5	[49]
Cat-16	Coprecipitation	53.84% (CO)	82.12% (DME) / 11.08% (CO$_2$)	280 °C, 4.0 MPa, 100 mL/min, H$_2$/CO = 1/1	[50]
5.0%Pd/ZnAl$_2$O$_4$	Hydrolysis method + incipient wetness impregnation	22.3% (CO)	51.9% (DME)	330 °C, 3.0 MPa, 3600 mL/(g$_{cat}$•h), H$_2$/CO/N$_2$ = 60/30/10	[51]
CZZ-FER	Hydrothermal synthesis + coprecipitation + physical mixing	26% (CO$_2$)	55.7% (DME)	260 °C, 5.0 MPa, 8800 NL/(kg$_{cat}$•h), CO$_2$/H$_2$/N$_2$ = 3/9/1	[52]
OX-FER/2	Coprecipitation	23.6% (CO$_2$)	47% (DME) / 15% (methanol)	260 °C, 5.0 MPa, 8800 NL/(kg$_{cat}$•h), CO$_2$/H$_2$/N$_2$ = 3/9/1	[53]
CZA/NSFER	Hydrothermal synthesis + coprecipitation	50.3% (CO)	89.0% (DME)	270 °C, 5.0 MPa, 5000 L/(kg$_{cat}$·h), CO/CO$_2$/H$_2$/N$_2$ = 21/9/66/4	[54]

oxygen vacancy (O$_{defect}$) were increased when the reduced ZrOx centers abstract O atoms from the active phases, and the ZrO$_2$ support also prevented the sintering of the In$_2$O$_3$ phases, which resulted in an enhanced catalytic stability for 1000 h (Fig. 2B-2) [45]. For more details, the specific In$_2$O$_3$ metal oxide phases were scrutinized and novel hexagonal In$_2$O$_3$ nanorod-containing {104} surfaces (denoted as h-In$_2$O$_3$-R were responsible for superior CO$_2$ conversion and methanol selectivity, and CO$_2$ hydrogenation mechanisms over the different In$_2$O$_3$ phases such as cubic In$_2$O$_3$ (c-(110) and c-(111)) and hexagonal In$_2$O$_3$ (h-(104) and h-(012)) were described in Fig. 2C based on the DFT computations and experiments [46]. Furthermore, the ZrO$_2$ and In$_2$O$_3$ as the promising metal oxides for CO$_2$ hydrogenation were utilized as well by preparing ZrO$_2$-In$_2$O$_3$ mixed metal oxides, where the ZrO$_2$ support could boost up the catalytic activity of the In$_2$O$_3$ phases during CO$_2$ hydrogenation. Particularly, the monoclinic ZrO$_2$ support helped an epitaxial growth of In$_2$O$_3$ phases in the form of subnanometric islands with copious and diverse oxygen vacant sites on the In$_2$O$_3$, which was helpful for a facile CO$_2$ adsorption followed by hydrogenation (Fig. 2D) [47].

2.2. CO$_x$ conversion to DME and carbonylation of dimethyl ether (DME)

DME is also one of the important platform chemicals, which can be converted into MA and ethanol, and it is a promising alternative fuel with many merits, therefore it seems to be worthy of studying the recently reported catalysts for DME synthesis from syngas as summarized in Table 1 [26–28]. Since DME can be successively synthesized by methanol dehydration over solid acid catalysts, one-step CO or CO$_2$ conversion over hybridized catalysts containing dual-active sites such as CO or CO$_2$ hydrogenation on metal (oxides) sites to form methanol and its dehydration to DME on acidic sites has been also largely investigated, where the one-step syngas to DME reaction (STD) is more thermodynamically favored as well [48,49]. The γ-Al$_2$O$_3$ has been widely used for one-step CO$_2$ to DME reaction on Cu-incorporated alumina (m-Al), where the Al$_2$O$_3$ was prepared by an evaporation-induced self-assembly (EISA) method to generate highly ordered mesoporous structures for

preventing the aggregations of Cu nanoparticles with the help of Ga or Zn oxide promoter. Those metal oxides-promoted Cu/m-GaAl and Cu/m-ZnAl showed good CO$_2$ conversion such as 23.4% and 24.5% than the pristine Cu/m-Al (CO$_2$ conversion of 22.0%) with DME (methanol) selectivity of 11.9 (41.2)% and 13.1 (45.2)% on Cu/m-GaAl and Cu/m-ZnAl, respectively (Table 1). The newly formed spinel-type CuAl$_2$O$_4$ phases revealed an enhanced thermal stability of Cu nanoparticles with an improved catalyst stability [48]. MgO promoter for STD reaction on CuO/ZnO/MgO catalyst (CZM) prepared by co-precipitation method showed the uniformly dispersed and accessible malachite crystallite structures as shown with TEM images of Fig. 3 A, which were responsible for medium acidic sites and small pore size at an optimum Cu/Zn molar ratio with favorable heat capacity due to an appropriate MgO content [49]. The CZM(20) composed of 20 wt% MgO hybridized with commercial γ-Al$_2$O$_3$ in weight ratio of 2:1 showed a higher CO conversion of 37% and DME selectivity of 83% with smaller byproducts selectivity of 14%. In addition, Sn-modified Cu-based catalysts with different Sn content also revealed the suppressed catalytic activity for water-gas-shift (WGS) reaction during STD reaction, which were attributed to the partial passivation of active metallic Cu sites with adjusted surface acidic sites by decreasing CO$_2$ selectivity with a higher DME selectivity [50].

In addition, typical ZnAl$_2$O$_4$ mixed metal oxides prepared by hydrolysis method followed by successive impregnation of active Pd metal in the range of 0.5 – 15 wt% selectively formed the active PdZn$_\beta$ phases reduced at higher temperature of 500 °C, which were known as active sites for syngas conversion to methanol and DME [51]. Zeolitic materials possessing various surface acidic sites have been also largely utilized for STD reaction. For example, Mordenite (MOR), Ferrierite (FER) or MFI type zeolites have been applied to prepare physically mixed hybrid catalysts such as CuZnZrOx metal oxides (CZZ) prepared by coprecipitation hybridized with hydrothermally synthesized zeolites (weight ratio of CuZnZrOx/zeolite = 2/1). The FER-based CZZ-FER catalyst revealed the best catalytic activity due to a larger population of Lewis basic sites for CO$_2$ activation and easier accessibility to Brønsted acid sites for methanol dehydration [52] as summarized in Fig. 3B, which

Table 2
Summarized catalytic activities and reaction conditions for a gas-phase DME carbonylation to methyl acetate (MA).

Catalyst	Zeolite type		Conversion	Selectivity and yield (STY)	Reaction conditions	Reference
	Framework	Channel				
SAR-25	Mordenite (MOR)	8-MR (5.7 × 2.6 Å)	96% (DME, max)	> 90% (MA)	190 °C, 2.0 MPa, 2000 h^{-1}, DME/CO = 1/50	[56]
SAR= 8		12-MR (7.0 × 6.5 Å)	37.2% (DME@1.5 h)	100% (MA@1.5 h)	200 °C, 1.5 MPa, 100 mL/min (500 mg catalyst), DME/CO = 1/49	[57]
H-MOR-UT			70% (DME)	100% (MA)	220 °C, 1.5 MPa, 20 mL/min (500 mg catalyst), Ar/DME/CO (3.10%Ar, 4.13%DME, 92.77% CO)	[58]
M-0.5			-	98.5% (MA) / deactivation rate: −9.3	190 °C, 1.5 MPa, 2000 h^{-1}, DME/CO = 2.0/ 98.0 (%)	[59]
3TMA-H-MOR			-	8.2 mol(MA)/(mol(H$^+$)·h) @ ~210 h	200 °C, 2.0 MPa, 2250 mL/(g$_{cat}$·h), DME/CO/ N$_2$ = 5/35/60	[60]
1Cu-4Zn/H-MOR			-	~90% (MeOAc) / 14.24 kg$_{MeOAc}$/ (kg$_{cat}$·h) (max. 240 g$_{MeOAc}$/(kg$_{cat}$·h)) for 86 h	210 °C, 2.0 MPa, 2.1 h^{-1}, CO/DME/H$_2$/He = 50.0/2.4/2.9/44.7 (%)	[61]
2Ce-M			61.0% (DME)	~98% (MA) / STY$_{MA}$ = 0.48 g/(g•h)	200 °C, 1.5 MPa, 6000 h^{-1}, DME/CO = 1/49	[62]
PEG-6000			~100% (DME)	~98.8% (MA) for 44 h	190 °C, 2.0 MPa, 2000 h^{-1}, DME/CO = 2/98	[63]
HMOR-C-3			67.0% (DME)	99% (MA) / STY$_{MA}$ = 482 g/(kg$_{cat}$·h) / TOF$_{MA}$ = 7.3 h^{-1}	200 °C, 1.5 MPa, 6000 h^{-1}, DME/CO = 1/49	[64]
MOR-TEAOH			90% (DME)	98% (MAc) / 3.60 mol(MAc)/ (mol$_{acid}$·h)	200 °C, 2.0 MPa, 1500 mL/(g·h), DME/CO/H$_2$ = 5/35/60 (Pyridine treatment: 200 °C, 1.3% pyridine−98.7% N$_2$ mixture for 1 h and N$_2$ flush for 1 h)	[65]
MOR(13.8)			-	STY$_{MA}$ = 7.2 mmol/(h·g)	200 °C, 2.0 MPa, 3600 mL/(g·h), DME/CO = 5/ 35 (Pyridine treatment: 200 °C, pyridine–Ar mixture for 20 min and Ar flush at 200 – 500 °C)	[66]
Catalyst B			36.4% (DME @50 h)	~100% (MA)	200 °C, 1.5 MPa, DME/CO = 1/47, 3000 h^{-1}, 0.5 g$_{cat}$ (Pyridine treatment: 50 °C, saturated pyridine vapor in N$_2$ for 2 h)	[67]
FER@FER	Ferrierite (FER)	8-MR (4.2 × 5.4 Å)	-	99.2% (MA) / 2.94 mmol(MA)/(g$_{cat}$·h) / TOF = 4.90 × 10^{-4} s^{-1}	220 °C, 1.0 MPa, 2000 L/(kg$_{cat}$·h), DME/CO/N$_2$ (mol%) = 5/45/50	[68]
FER-S1		12-MR (3.5 × 4.8 Å)	30.4% (DME, max)	96.8% (MA) / STY$_{MA}$ = 1.2 mmol (MA)/(g$_{cat}$·h)	220 °C, 1.0 MPa, 2000 L/(kg$_{cat}$·h), DME/CO/N$_2$ (mol%) = 5/45/50	[69]
FER(S7)			34.3% (DME, max)	97.6% (MA, max)	220 °C, 1.0 MPa, 2000 L/(kg$_{cat}$·h), DME/CO/N$_2$ (mol%) = 5/45/50	[70]
HEU-12	ETL	8-MR (4.6 × 2.8 Å) 8-MR (5.0 × 2.7 Å) 8-MR (4.8 × 3.3 Å)	15.7% (DME)	> 90% (MA)	220 °C, 1.5 MPa, 0.5 g catalyst, Ar/DME/CO (%) = 3.03/4.13/92.84	[71]
SSZ-13(9)	Chabazite (CHA)	8-MR (3.8 × 3.8 Å) 8-MR (3.8 × 3.8 Å) 8-MR (3.8 × 3.8 Å)	-	-	165 °C, 0.1 MPa, DME/He(Ar)/CO = 2/3/95	[72]
K-modified HSUZ-4 (KAl = 0.132)	SZR	10-MR (4.1 × 5.2 Å) 8-MR (3.2 × 4.8 Å) 8-MR (3.0 × 4.8 Å)	26% (DME)	> 95% (MA)	220 °C, 2.0 MPa, 1250 mL/(g·h), DME/CO/Ar/ He (vol%) = 5/50/2.5/42.5	[73]
Al-RUB-41(54) @SiO$_2$	RRO	8-MR (5.0 × 2.7 Å) 10-MR (6.5 × 4.0 Å)	25% (DME, max)	96.76% (MA)	200 °C, 1.5 MPa, 2400 mL/(g·h), DME/CO/Ar/ N$_2$ (vol%) = 1.94/45.55/2.51/50, 0.5 g catalyst,	[74]

was attributed to the suppression of mass-transfer limitation between metal oxides and zeolites. In addition, the best activity-selectivity patterns of OX-FER/2 catalyst (CuZnZrOx/FER system) was explained with the positive contributions of suitable particle size, proper number of acidic sites and more homogenous distribution of metal-oxide-acid sites [53]. Furthermore, various FERs with different morphology were also applied to prepare bifunctional catalysts such as the coprecipitated Cu-ZnO-Al$_2$O$_3$ (CZA) over nanosheet-structured FER (NSFER), mesoporous FER (m-FER) and commercial plate-like FER (CFER). The much higher catalytic activity on the CZA/NSFER was observed with CO conversion of 50.3% and DME selectivity of 89.0%, which was mainly

attributed to a higher dispersion of Cu nanoparticles over the more hydrophobic NSFER with a larger surface area and easy removal of water formed due to its specific morphology as displayed in Figs. 3C-1, 3C-2 and 3C-3. In addition, the highly dispersed ZnO moiety possessed more hydrophobic surface natures which was beneficial for STD reaction by suppressing reverse water gas shift (RWGS) activity as well [54].

In a summary, in addition to typical Cu/ZnO/Al$_2$O$_3$ catalysts for CO$_2$ hydrogenation and STD reaction applications, various mixed metal oxides have been reported as the effective CO$_2$ hydrogenation catalysts. The ZrO$_2$ and In$_2$O$_3$ have been paid more attention with some mixed metal oxides such as ZrO$_2$-In$_2$O$_3$, AlCeOx or GaZrOx. On those mixed
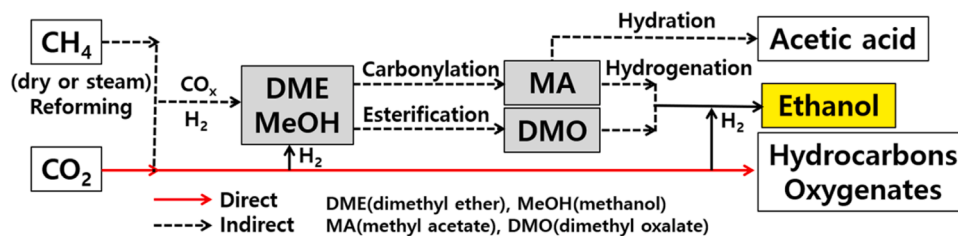
Table 3

Summarized catalytic activities and reaction conditions for hydrogenation of MA/DMO/AA with selective ethanol production.

Catalyst	Preparation method	Conversion	Selectivity and yield	Reaction conditions	Reference
30Cu@CeO$_2$	Sol-gel method	~100% (MA)	~100% (Ethanol)	215 °C, 2.5 MPa, H$_2$/MA (vol%) = 80, LHSV= 1.0 h^{-1}	[76]
Cu/SiO$_2$	Precipitation-gel method	96.2% MA	61.7% (Ethanol)	250 °C, 1.0 MPa, MA/H$_2$ (vol%) = 3/97, GHSV = 6000 mL/(g$_{cat}$·h)	[77]
Cu$_9$Zn$_1$-SiO$_2$	Hydrolysis precipitation method	-	STY = 1.024 g$_{Ethanol}$/(g$_{cat}$·h)	220 °C, 2.0 MPa, H$_2$/MA (mol) = 20	[78]
25Mo$_2$C/SiO$_2$	Hydrogen thermal treatment method	99.9% (MA) 100% (DMO)	70.8% (Ethanol) 76.4% (Ethanol)	200 °C, 2.5 MPa, LHSV = 0.2 h^{-1}, H$_2$/MA or H$_2$/DMO (mol) = 200	[79]
0.03Cu-Mo$_2$C	Solid-state pyrolysis	100% (DMO)	67.2% (Ethanol) / yield$_{Ethanol}$ = 67.2% / TOF = 0.58 h^{-1}	200 °C, P(H$_2$) = 2.5 MPa, LHSV = 0.2 h^{-1}, H$_2$/DMO (mol) = 200	[80]
FeNi$_3$-FeO$_x$/Ni-foam-(550/350)	Hydrothermal synthesis + incipient impregnation	100% (DMO)	98% (Ethanol)	230 °C, 2.5 MPa, SV$_{DMO}$ = 0.44 h^{-1}, H$_2$/DMO (mol) = 90 for 700 h	[81]
Fe@C	One-pot hydrothermal synthesis	> 95% (DMO)	84.3% (Ethanol)	270 °C, 3.5 MPa, LHSV = 0.19 h^{-1}, H$_2$/DMO (mol) = 180	[82]
Re$_5$-Cu$_{20}$/SiO$_2$	Ammonia evaporation-impregnation method	100% (DMO)	90% (Ethanol)	230 °C, 1.5 MPa, LHSV = 0.36 h^{-1}, H$_2$/DMO (mol) = 280 for 800 h	[83]
CuMgAl-LDH-1.25	Coprecipitation method	100% (DMO)	83% (Ethanol)	280 °C, 3.0 MPa, WHSV = 0.5 h^{-1}, H$_2$/DMO (mol) = 200	[84]
9Cu1In/SBA-15	Deposition-precipitation method	99.1% (AA)	90.9% (Ethanol)	350 °C, 2.5 MPa, LHSV = 1.25 h^{-1}, H$_2$/AA (mol) = 30	[85]
PtSn1.6/SiO$_2$-MTSG	Modified two-step sol-gel method	98.3% (AA)	91.8% (Ethanol)	270 °C, 2.6 MPa, WHSV$_{(AcOH)}$ = 2.0 h^{-1}, H$_2$/AcOH (mol) = 20	[86]
3Rh5Sn/Al$_2$O$_3$	Impregnation method	98% (AA)	74% (Ethanol)	275 °C, 2 MPa, LHSV = 0.9 h^{-1}, H$_2$:AcOH (mol) = 10:1	[87]
Pt/MIL-125-NH$_2$	Plasma deposition method	-	Yield = 31% (Ethanol)	200 °C, 1.0 MPa, H$_2$ gas with saturated vapor of AcOH, 3 sccm at 1.0 MPa	[88]

Table 4

Summarized catalytic activities and reaction conditions for indirect ethanol productions by tandem reactions.

Catalyst	Preparation method	Conversion	Selectivity and yield	Reaction conditions	Reference
ZnAl$_2$O$_4$|H-MOR|ZnAl$_2$O$_4$	Triple-bed separated by quartz wool	6% (CO)	52% (Ethanol)	430 °C, P = 3.0 MPa, 25 mL/min, H$_2$/CO (mol) = 1	[89]
CuZnAl-HZSM-5 + Zn-HMOR-20 + CuZnAl	Triple-bed separated by quartz wool	7% (CO)	52.0% (Ethanol at 200 h)	220 °C, 2.0 MPa, 2000 mL/(g$_{cat}$·h), H$_2$/CO = 2:1 (Pyridine treatment: 1.3% pyridine-98.7% N$_2$ mixture for 3 h and N$_2$ flush for 3 h)	[90]
NZ35 + CZA-D	Dual-bed separated by quartz sand	47.0% (DME)	45.6% (Ethanol)	220 °C, 2.5 MPa, 4800 mL/(g·h), DME/CO/H$_2$/Ar (mol%) = 2.1/46.4/50.0/1.5	[91]
Cu$_{0.55}$/HZSM-35 + Cu$_1$-Zn$_1$-Al$_{0.1}$	Dual-bed	27.1% (DME)	829.5 mmol(Ethanol)/(kg·h)	220 °C, 1.5 MPa, Ar/DME/CO/H$_2$ (mol%) = 1.51/2.00/46.49/50.00	[92]
CZ@Cu-MOR	Coprecipitation + hydrothermal synthesis method	26.8% (DME)	45.9% (Ethanol)	220 °C, 1.5 MPa, Ar/DME/CO/H$_2$ = 1.55/2.35/46.10/50.00	[93]
CuZnAl + FER	Dual-bed separated by quartz wool	42% (DME)	Ethanol 45% / Ethanol yield 19%	493 K, 1.5 MPa, Ar/DME/CO (molar ratio of 3/4/93, 20 mL/min) + H$_2$ (20 mL/min)	[94]
K$^+$-ZnO-ZrO$_2$ + H-MOR-DA-12MR + Pt-Sn/SiC,	Triple-bed separated by quartz wool	0.7% (CO) 4.0% (CO)	90% (Ethanol) 81% (Ethanol)	230 °C / 270 °C, 5.0 MPa, 25.0 mL/min, H$_2$/CO (mol) = 1:1	[95]

Fig. 1. Overall schemes of C1 gases conversions for the production of value-added chemicals and alternative fuels.

metal oxides, the extent of oxygen vacant sites and solid-solution phase formations largely affected CO$_2$ adsorption phenomena and formation of reaction intermediates during CO$_2$ hydrogenation. For STD reaction, Cu-based catalysts have been dominantly modified with additional promoters such as Ga, In, Mg and Sn and so on, which can be hybridized with solid acid zeolites. The Pd-based catalysts were also reported over zinc aluminate by unraveling the effects of PdZn phases. During STD reaction, the successive dehydration of methanol formed by CO$_2$

hydrogenation occurs over acidic sites, and the modulations of solid acid catalysts are also important and FER zeolite has been known as the interesting candidate possessing different chemical and morphological properties.

DME synthesized from direct syngas conversions can be further subjected to carbonylation reaction of DME to form methyl acetate (MA) over various zeolites (Table 2) which contains 8-membered ring (8-MR) channels with more active Brønsted acid sites (BAS) through the
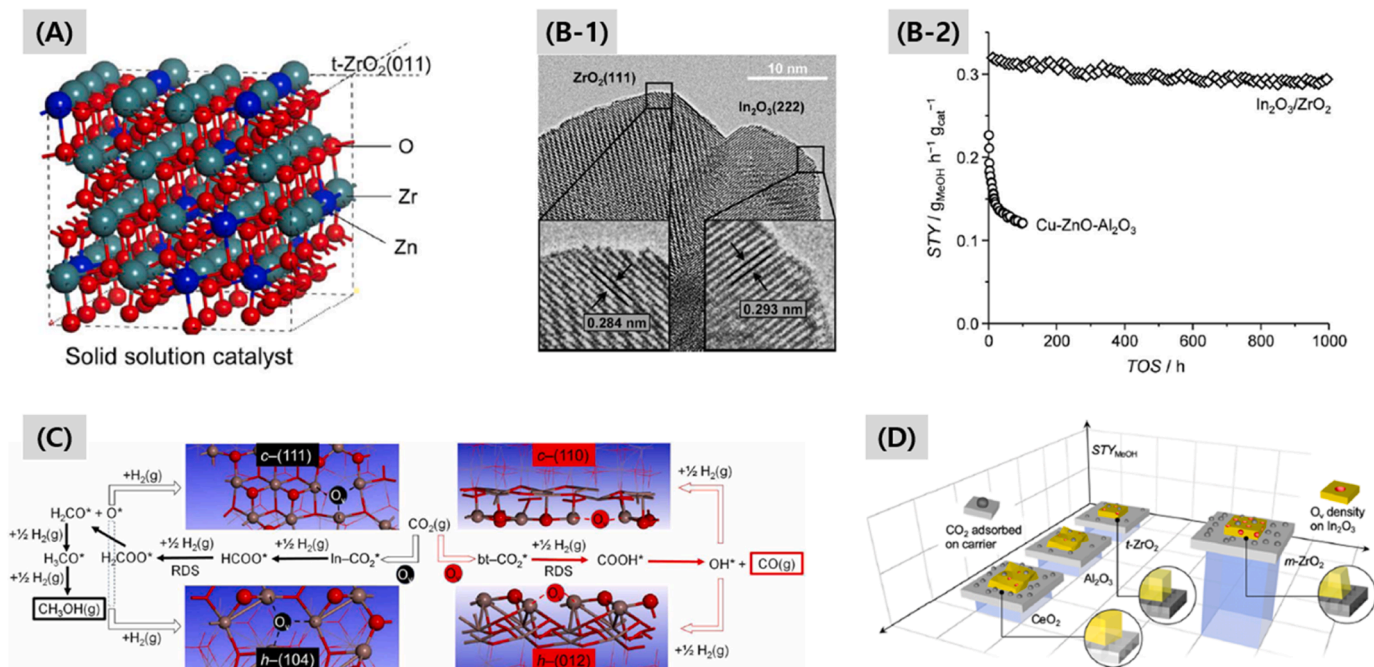
Fig. 2. Experimental results for CO_2 hydrogenation to methanol; (A) Models of ZnO-ZrO_2 solid solution (ref. [43]), (B-1) TEM images and (B-2) Catalytic activity on In_2O_3/ZrO_2 (ref. [45]), (C) DFT computations and reaction mechanisms over various In_2O_3 phases (ref. [46]) and (D) Oxygen vacant sites and CO_2 adsorption capacity on In_2O_3 (ref. [47]).
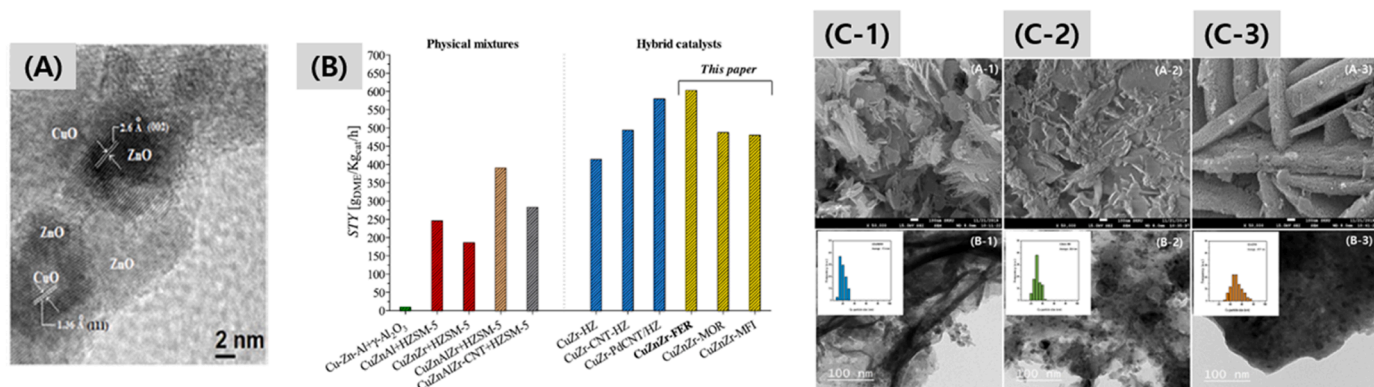

Fig. 3. (A) TEM image of CZM(20) catalyst (ref. [49]), (B) Catalytic activity on various Cu-based catalysts and zeolites (ref. [52]) and (C) SEM and TEM images of (1) CZA/NSFER, (2) CZA/m-FER and (3) CZA/CFER (ref. [54]) for one step CO/CO_2 hydrogenation to DME.

formations of surface methyl and acetyl intermediates formation [22,29, 55]. Typically, various Mordenite (MOR) zeolite has been studied in terms of the adjustments of surface acidic sites distribution, morphology, extra metal insertion and organic material modification [56–67]. The MOR zeolite with different SiO_2/Al_2O_3 ratio (x) in a synthesis gel, denoted as SAR-x, showed the decreased defect sites and smaller non-skeleton Al atoms, which were derived from the decreased Al atoms due to an increased SiO_2/Al_2O_3 ratio. The Al framework atoms were prone to be located in the medium and strong acidic sites in the 8-MR channels during the crystallization step by largely altering DME carbonylation activity, and the maximum DME conversion to MA was observed on the SAR-25 with a higher SiO_2/Al_2O_3 ratio of 25 [56]. In addition, H-MOR with different Si/Al ratio in the range of 8 – 26 was prepared by simple acid-treatment by using oxalic acid and ammonium hexafluorosilicate (AHFS), and best catalytic activity was obtained over the SAR= 8 (Si/Al ratio of 8) with 37.2% DME conversion and 100% MA selectivity, which were induced by the abundant stronger BAS in the 8-MR channels as quantified by DFT and FTIR-TPD method with NH_3

probe molecule. The stronger acidic sites enhanced DME carbonylation activity by decreasing activation barriers of CO insertion to form acetyl groups during DME carbonylation reaction [57]. The metal salt additive, crystallization temperature and crystallization time also changed the crystallinity of MOR zeolite, and the optimized MOR was synthesized by using NaCl and ultrasonic treatment after hydrothermal synthesis at 130 °C for 48 h (H-MOR-UT), which showed best catalytic activity such as DME conversion above 70% and MA selectivity of 100% due to smaller grain size and decreased external surface area with stronger acidic sites [58]. The alkaline-treated MOR (SiO_2/Al_2O_3 = 25) in NaOH solution with its different concentration (x, denoted as M-x) showed the formation of different sizes of mesopores as shown in Fig. 4A. The NaOH solution treatment of MOR was found to be effective to enhance the catalyst stability due to the selective elimination of stronger acid sites [59]. In addition, the ion exchange with TMA^+ ions (trimethyl amine) with different time (x), denoted as xTMA-H-MOR (excellent stability for x = 3 h treatment), also revealed the greatly improved catalytic stability during DME carbonylation. The acidic sites in the 12-MR channels on
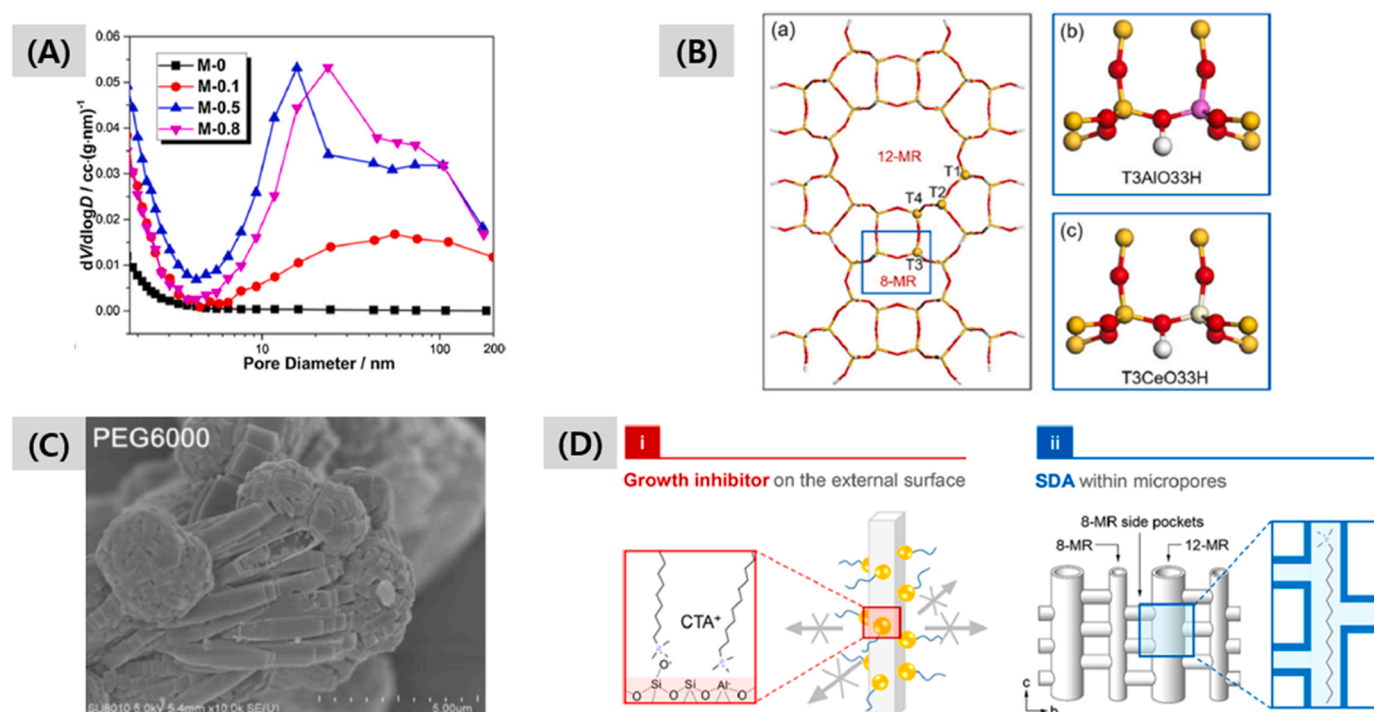
Fig. 4. Characteristics of Mordenite (MOR) catalysts for DME carbonylation to methyl acetate (MA); (A) Catalytic activity on M-*x* catalysts (ref. 59), (B) Model of *x*Ce-M catalyst from DFT calculations (ref. 62), (C) SEM image of PEG-6000 (MOR) catalyst (ref. 63) and (D) Schematic diagrams of roles of CTAB during HMOR-m synthesis (ref. 64).

the MOR were selectively removed by the ion exchange with TMA^+, which showed no sign of deactivation for 210 h reaction over 3TMA-H--MOR [60].

The Cu and Zn metal oxide-treated Cu-Zn/H-MOR also significantly enhanced the catalytic stability, where the 1Cu-4Zn/H-MOR showed a higher selectivity to MA and its yield of 14.24 kg_{MA}/kg_{cat} with longer lifetime for 86 h [61] and the Zn species on the Cu/H-MOR suppressed the formations of hard coke precursors. The incorporation of Ce species into MOR structures was carried out by facile one-pot hydrothermal synthesis method by adding Ce precursor into MOR synthesis gel, which adjusted acidic sites by increasing the active BAS in the 8-MR channels due to an increased Si-OH-Al frameworks in the 8-MR channels. In case of the *x*Ce-M catalyst, where *x* denoted mole percentage of Ce metal on the MOR, and the highest DME conversion and space time yield (STY_{MA}) of 0.48 g/(g•h) were observed on the 2Ce-M with MA selectivity of ~100% during DME carbonylation reaction. Because the Si-OH-Al and Si-OH-Ce showed a distinct acidity, the enrichment of the Si-OH-Al groups in the 8-MR channels improved catalytic activity as clearly proved by DFT computations by using T3AlO33H and T3CeO33H model structures as shown in Fig. 4B [62]. The MOR with special morphology such as nanosheet or spherical structures was applied for DME carbonylation, and nanosheet MOR was prepared by polyethylene glycol (PEG) addition, which was denoted as PEG-*x* (*x* = molecular weight of PEG). The surface morphology of PEG-6000 catalyst with SEM images is displayed in Fig. 4C, and the surface area and total pore volume were changed according to molecular weight of PEG with the larger specific surface area and pore volume of 80.3 m^2/h and 0.017 cm^3/g on the optimized PEG-6000 catalyst with longer stability. In addition, strong acidic sites were slightly increased after PEG addition, and the PEG-treated MOR showed ~100% DME conversion and 98.8% MA selectivity [63]. Cetyltrimethylammonium bromide (CTAB) was also known to be effective organic structure directing agent (SDA) to prepare nanosheet MOR such as HMOR-C-*m* (*m* = weight percentage of CTAB in synthesis gel with 0.5, 1, 3, 5). The roles of CTAB are illustrated in Fig. 4D and it acted as growth inhibitor on the external surfaces to

modulate morphology and less framework Al incorporation was observed by locating SDA within the micropores. The maximum DME conversion of 67.0%, STY_{MA} of 482 g/(kg_{cat}·h) and turn-over frequency (TOF_{MA} of 7.3 h^{-1}) with higher MA selectivity over 99% were observed on the HMOR-C-3 due to the alleviated diffusion limitations derived from the specific nanosheet morphology [64]. Spherical MOR zeolite was also synthesized by using tetraethylammonium hydroxide (TEAOH) through amine-assisted dry-gel transformation method. The synthesized spherical MOR with millimeter crystallite size and intergrowth of MOR crystallites in the sphere showed a good mechanical strength and well-retained morphology, which was attributed to organic amine in a synthesis vapor by promoting crystallization and by increasing Si/Al ratio. The abundant protons located in the 8-MR side pockets revealed better catalytic activity after the successive treatments like N_2 pre-treatment, pyridine purging and N_2 flushing step [65].

Therefore, the selective blockages of 12-membered ring (12-MR) channels of MOR were proposed with pyridine-pretreatment method since the acidic sites in 12-MR channels are prone to enhance side reactions resulted in rapid carbon depositions and catalyst deactivation. The pyridine molecules were treated on the MOR having different Si/Al ratios by purging with pyridine-Ar mixture at 200 °C followed by flushing with Ar until the pyridine molecules were completely removed in the temperature range of 200–500 °C. The catalytic stability of the pyridine-treated MOR having Si/Al ratio of 13.8 was largely enhanced with the higher yield of MA (7.2 mmol/(h·g)) [66]. Furthermore, DFT calculations revealed that the effects of pyridine modifications on the MOR were to change the strengths of Brønsted acid sites originated from two Al atoms through pyridine occupations, where the weakened Brønsted acid between two Al atoms after pyridine adsorption further enhanced the strength of another Brønsted acid sites. The stability of pyridine molecules was weakened when the pyridine molecules occluded two Brønsted acid sties because of their steric exclusion. In addition, coke precursors generated in the 12-MR channels also led to the desorption of closely adsorbed pyridine molecules due to their steric hinderance effects resulted in a fast catalyst deactivation. Therefore, the

enrichments of Brønsted acid sites in the 8-MR channels with less amounts of acidic sites in 12-MR channels are better to increase catalytic activity and stability as confirmed by DFT calculations [67].

In addition to MOR zeolite, ferrierite (FER) zeolite has been also largely used for a gas-phase DME carbonylation due to the copresence of the 8-MR and 10-MR channels, which suppress coke depositions during DME carbonylation compared to the 12-MR channels in MOR. In order to enhance the crystallinity of the FER zeolite with abundant Brønsted acid sites in the 8-MR channels, seed-derived synthesis methods have been largely applied by using various zeolite seeds [68]. Particularly, the seed-derived FER prepared with FER seed (FER@FER) revealed a superior catalytic activity owing to its higher crystallinity, where it was disclosed that the enhancement of FER@FER crystallinity also increased stable Brønsted acid sites assigned to the stable T2 sites in the 8-MR and 10-MR channels. In addition, the formation of defected Al sites, extra-framework Al species (EFAL), was suppressed after recrystallization of FER, and the slowest deactivation rate and highest TOF value was observed on the FER@FER due to the well-developed crystalline structures with the appropriate acidic properties [68]. The effects of recrystallization were also proved by testing the lab-made FER zeolite (FER-S0, Fig. 5A-1) as a seed and seed-derived FER (FER-S1, Fig. 5A-2) and FER-S1-derived FER after double successive recrystallization (FER-S2, Fig. 5A-3). The successive recrystallization steps caused the less depositions of coke precursors by creating more intensive Brønsted acid sites and less Lewis acidic EFAl sites due to the appropriate Al distributions and configurations in the 8-MR channels. However, the double successive recrystallization for FER-S2 caused the repulsive adsorption of DME molecules by generating less stable intermediates due to improper Al distributions and configurations. Especially, the distributions of Brønsted acid sites in the tetrahedral T2 sites with next-nearest Al-O-Si-O-Al configurations with two neighboring Al atoms affected acetyl intermediate formation and generation of coke precursors in the 8-MR and 10-MR channels. Therefore, proper Al distributions in the 8-MR channels and suppression of EFAl sites formations were achieved by recrystallization of the FER-S1 which were verified by DFT calculations after establishments of model FER structures (Figs. 5B, 5C and 5D) [69]. In addition, an appropriate seed weight (X) in the range of 3–30 wt% to prepare the seed-derived FER was also investigated, and the commercial FER (FER(C)) was used as a seed material

during a typical FER synthesis step to prepare FER(SX). The optimum seed weight percent was found to be 7 wt% (FER(S7)), which showed maximum DME conversion of 34.3% and MA selectivity of 97.6% during 100 h reaction. Furthermore, the relative amounts of coke precursors deposited on the external and internal acidic sites were quantified by combination of N_2-sorption and TGA method and the correlations between deactivation phenomena and amounts of external cokes were clearly observed, where the extents of external coke precursors were closely related with initial fast deactivation by blocking pore mouths [70].

Although lots of different MOR-based catalysts have been studied for DME carbonylation and the natures of Brønsted acid sites located in the 8-MR channels were found to be most essential to properly activate gas-phase DME and CO molecules to produce MA, another zeolite frameworks which contain the 8-MR channels have been more paid attentions to further enhance catalytic activity and stability. For example, EU-12 zeolite, which belongs to ETL type frameworks, was used for DME carbonylation since the ETL zeolite is composed of two-dimensional 8-MR channels (4.6 ×2.8 and 5.0 ×2.7 Å) where the smaller channels are connected with sinusoidal 8-MR channels (4.8 ×3.3 Å). The EU-12 zeolite showed its clear typical XRD patterns (Fig. 6A) denoted as HEU-12 and it showed 15.7% DME conversion and MA selectivity above 90% [71]. Chabazite (CHA)-type zeolite which contains the 8-MR channels (3.8 ×3.8 Å) with 3-dimentional structures, denoted as SSZ-13, was also applied for DME carbonylation, and the XRD patterns ascertained the specific CHA frameworks with different Si/Al ratios (Fig. 6B). As decrease of Si/Al ratio on the SSZ-13, MA production rate was increased and the best catalytic activity was observed on the SSZ-13 (9), where the DFT computations suggested that the lowest activation barrier for the RDS was the nucleophilic attack by CO at methoxy groups in the 8-MR channels [72]. In addition, SZR structures contain the 8-MR and 10-MR channels with 3-dimentional pore structures such as 4.1 × 5.2 Å for 10-MR channels and 3.2 × 4.8 Å and 3.0 × 4.8 Å for 8-MR channels as described in Fig. 6C. The SUZ-4 zeolite, which belongs to SZR-type zeolite, showed DME conversion over 26% on the rod-shape HSUZ-4 with MA selectivity above 95%. The good activity of the rod-shaped HSUZ-4 was explained by abundant pore openings with enhanced diffusion rates of molecules [73]. On the other hands, Al-modified RUB-41 (RRO structure) with 2D pore structures of the
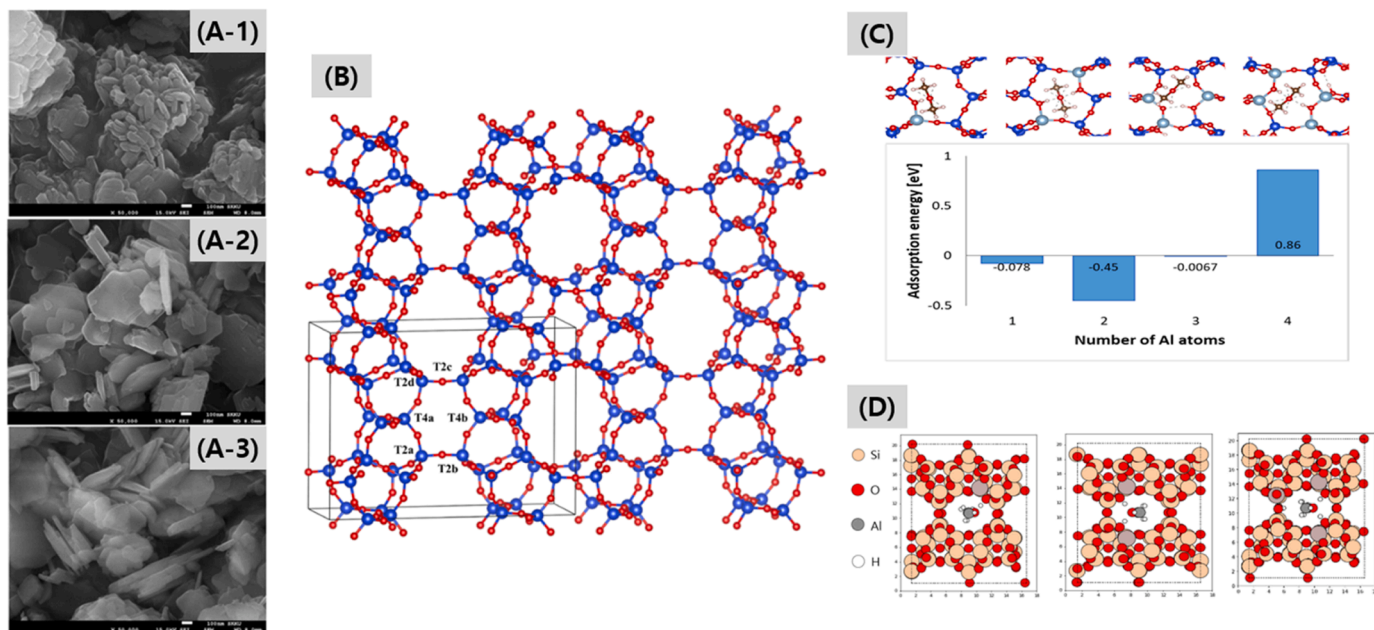

Fig. 5. SEM images of seed-derived FER zeolites; (A-1) FER-S0 (seed), (A-2) FER-S1 (first recrystallization with FER-S0) and (A-3) FER-S2 (second recrystallization with FER-S0), (B) Models of FER-S1, (C) Al distributions in FER-S1 and (D) DME adsorption energy on the model FER sites during DME carbonylation (**ref.** 69).
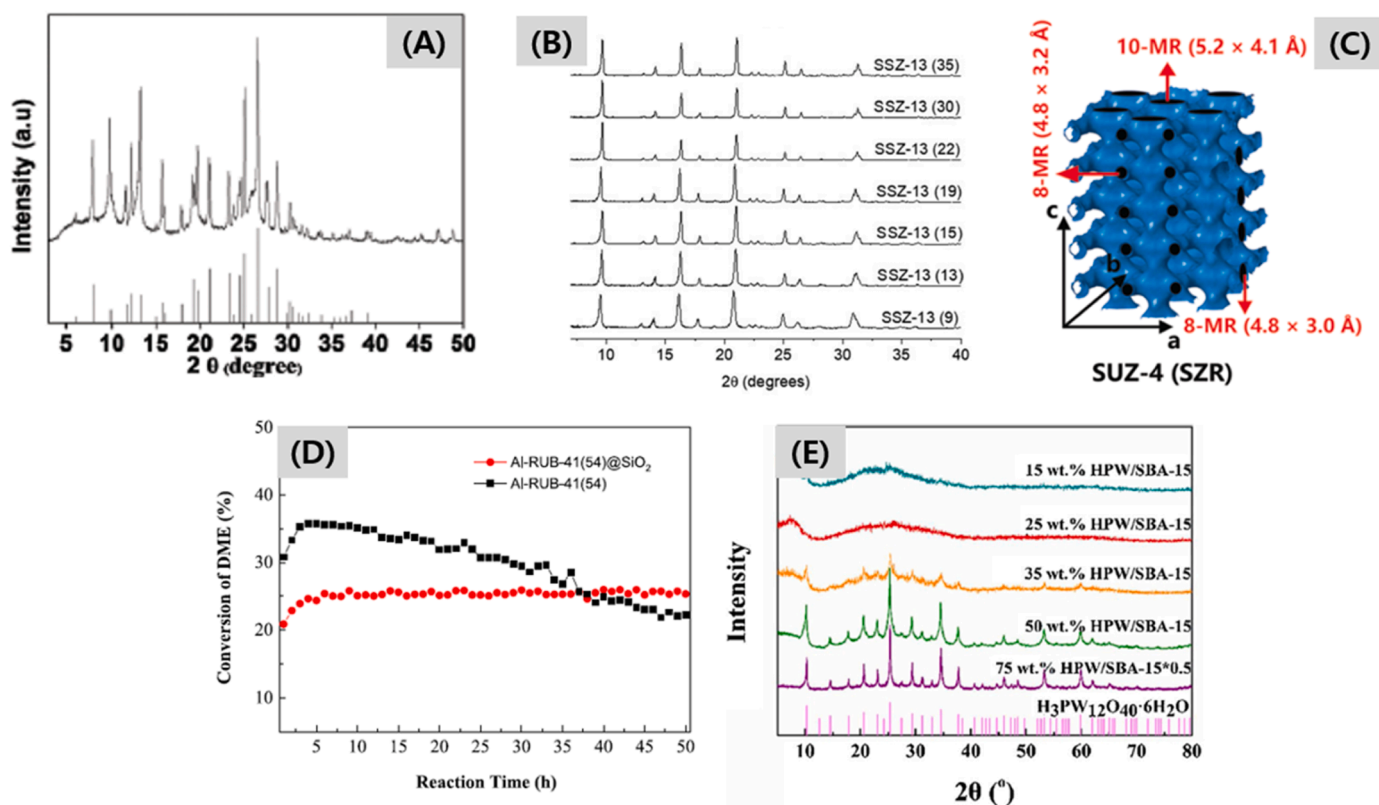
Fig. 6. Characteristics of various zeolites for gas-phase DME carbonylation; (A) XRD patterns of EU-12 (ref. 71), (B) XRD patterns of SSZ-13 with different Si/Al ratio (ref. 72), (C) Model structures of SUZ-4 (ref. 73), (D) DME carbonylation activity on Al-RUB-41(54)@SiO$_2$ (ref. 74) and (E) XRD patterns of HPW/SBA-15 catalysts (**ref.** 75).

intersecting 8-MR (5.0 ×2.7 Å) and distorted 10-MR (6.5 ×4.0 Å) channels was applied for DME carbonylation reaction, and the most suitable Si/Al ratio of 54 was observed on the Al-RUB-41(54) and successive SiO$_2$-coated Al-RUB-41(54)@SiO$_2$ further enhanced catalytic stability by blocking outer surface acidic sties with smaller coke depositions (Fig. 6D) [74].

Some heteropoly acids (HPAs) have been also utilized for a gas-phase DME carbonylation, and the HPAs dispersed on SBA-15 prepared by wet impregnation with phosphotungstic acid, silicotungstic acid and phospomolybdic acid were also investigated with HPAs/SBA-15 like HPW/SBA-15, HSiW/SBA-15 and HPMo/SBA-15. As confirmed by XRD patterns in Fig. 6E, the higher weight of HPW on the SBA-15 clearly showed the characteristic HPW peaks and the highest MA yield was observed on the 15 wt% HPW/SBA-15. A lower loading of HPW led to a higher utilization efficiency of HPW with better dispersion, however the strengths of Brønsted acid sites were weakened by forming more undesired byproducts [75], which revealed new applications of heteropoly acids for DME carbonylation as well.

2.3. Hydrogenation of oxygenates to ethanol

In this section, ethanol production processes via hydrogenation by MA, dimethyl oxalate (DMO) and acetic acid (AA) feed are discussed. MA can be produced by DME carbonylation and DMO- and AA-hydrogenation routes are also attractive since the DMO and AA are widely used chemicals and important platform chemicals.

MA as the simplest ester groups is one of the important intermediates formed from various C1 chemistry based reactions because of the C-O and C-C bonds, where the MA can be converted into ethanol via successive hydrogenation reaction on non-noble metal-based catalysts through multi-step cascade reactions [20,22,29]. For the MA hydrogenation reaction, the core-shell structured Cu@CeO$_2$ synthesized by

sol-gel method revealed the much stable activity compared to an impregnated Cu/CeO$_2$-IM catalyst as schematically displayed in Fig. 7A-1 for Cu/CeO$_2$-IM, Fig. 7A-2 for Cu@CeO$_2$ and Fig. 7A-3 for Cu^0/Cu$^+$ distribution over the Cu@CeO$_2$. As briefly summarized in Table 3, the core-shell structured Cu@CeO$_2$ catalyst effectively inhibited the migration and aggregation of Cu nanoparticles resulted in an enhanced catalytic stability. In addition, the core-shell morphology increased the contact area of Cu and CeO$_2$ by enlarging the surface Cu$^+$ concentrations due to the stronger interactions between Cu and CeO$_{2-x}$ interfaces [76]. Similar with the core-shell structured Cu@CeO$_2$, CuO nanoparticles coated with SiO$_2$ layers also generated CuO-SiO$_2$ interfaces with the fully reduced metallic Cu phases. However, Cu^{2+} phases on CuO-SiO$_2$ interfaces were partially reduced to form Cu$^+$ phases with Cu$^+$/(Cu^0 +Cu$^+$) content of ~28%, where the sizes of Cu nanoparticles and core-shell structures were preserved stably even after the reaction for 100 h and the value of Cu$^+$/(Cu^0 +Cu$^+$) was increased up to 38.9% due to an increased interactions of the Cu nanoparticles at the Cu-SiO$_2$ interfaces and the reaction mechanisms are illustrated in Fig. 7B [77]. Both the core-shell structures of Cu@CeO$_2$ and Cu@SiO$_2$ were well preserved by maintaining their pristine Cu particle sizes by properly adjusting the electronic states of Cu phases, which further enhanced catalytic activity and stability with ~100% conversion of MA and 100% selectivity to ethanol on the 30Cu@CeO$_2$ (30 wt% of Cu) compared to the Cu/SiO$_2$ with 96.2% conversion of MA and 61.7% selectivity to ethanol [76,77]. In addition, Zn oxides were also added to Cu phases on the SiO$_2$ support (CuZn-SiO$_2$) via a hydrolysis precipitation (HP) method with different Cu/Zn molar ratio. The Cu$_9$Zn$_1$-SiO$_2$ showed superior catalytic activity because of its higher dispersion of active sites and improved Cu$^+$ species derived from Cu-ZnO interactions resulted in an improved ethanol yield [78]. In case of MA hydrogenation, although very few Cu-based catalysts haven been reported till now, the roles of Cu$^+$ phase was found to be important and Zn oxides can enhance the
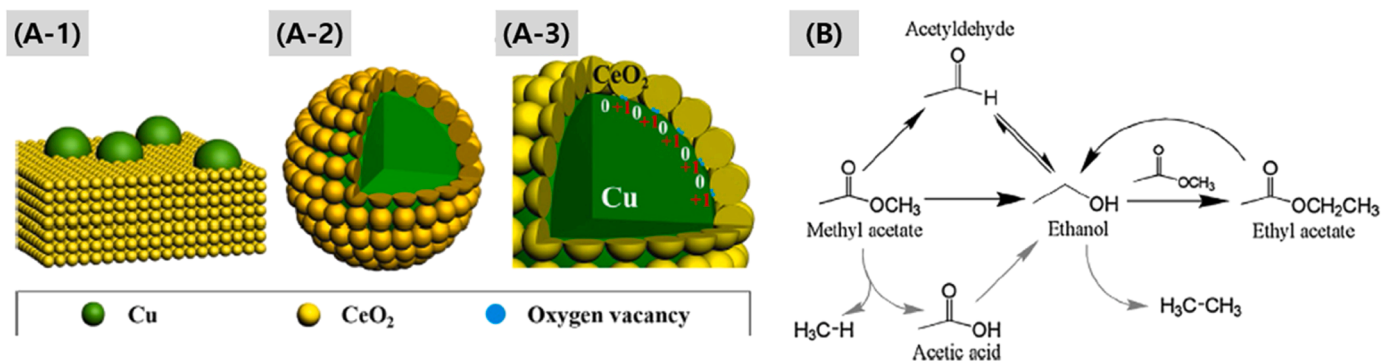
Fig. 7. Schematic diagrams of (A-1) Cu/CeO$_2$-IM catalyst, (A-2) Cu@CeO$_2$ catalyst, (A-3) Cu^0/Cu$^+$ distribution over Cu@CeO$_2$ (**ref.** 76) and (B) Reaction mechanisms of MA hydrogenation to ethanol (**ref.** 77).

catalytic activity by adjusting Cu$^+$ phases, where further researches are under investigation to control morphology and mixed oxides compositions as well.

In case of DMO-mediated route for a selective synthesis of ethanol, DMO formed by esterification of oxalic acid with methanol or by oxidative carbonylation of methanol can be hydrogenated to ethanol at a mild reaction condition compared to the MA-mediated route as summarized in Table 3. Two typical heterogeneous catalysts for DMO hydrogenation can be categorized such as metal carbides (Mo$_2$C) and metal oxides [79–81]. A silica-supported Mo$_2$C was prepared and the best catalytic activity was observed on the 25Mo$_2$C/SiO$_2$ (25 wt% Mo$_2$C on SiO$_2$), where is revealed a superior MA conversion of > 99.9% and ethanol selectivity of 76.4%. The reaction mechanisms are described in Fig. 8 A [79]. To avoid Mo$_2$C leaching problems on the SiO$_2$ support, Cu-doped Mo$_2$C was synthesized by a solid-state pyrolysis reaction with Mo, C and Cu precursor, which was denoted as xCu-Mo$_2$C with different atomic ratio (x) of Cu/Mo. The optimized 0.03Cu-Mo$_2$C

nanoparticles exhibited a higher catalytic activity and selectivity to ethanol and the doped Cu nanoparticles on the Mo$_2$C stabilized the active sites by generating the strongly interacted Cu nanoparticles on the Mo$_2$C surfaces [80]. In addition, FeNi$_3$ solid solutions were prepared by hydrothermal synthesis and incipient wetness impregnation method as displayed in Fig. 8B by using Ni-foam sheet to form Ni(OH)$_2$/Ni-foam substrate by impregnating Fe precursor, which was treated at an optimal calcination temperature of 550 °C and reduction temperature of 350 °C (FeNi$_3$-FeO$_x$/Ni-foam-(550/350)). The FeNi$_3$-FeO$_x$ was prepared by calcining at 550 °C to form NiFe$_2$O$_4$-NiO composites and by successively reducing at 350 °C to form FeNi$_3$-FeO$_x$. The formation of FeNi$_3$ nano-alloy with FeOx nanoparticles was responsible for activating ester groups in DMO molecules to form hydroxyl groups by acting as acidic sites [81]. In addition, the confined iron catalysts such as Fe@C converted MA to ethanol with its higher selectivity of 84.3% accompanied by a higher DMO conversion above 95%. The Fe@C prepared by one-pot hydrothermal synthesis method also possessed the active Fe$_5$C$_2$ phases
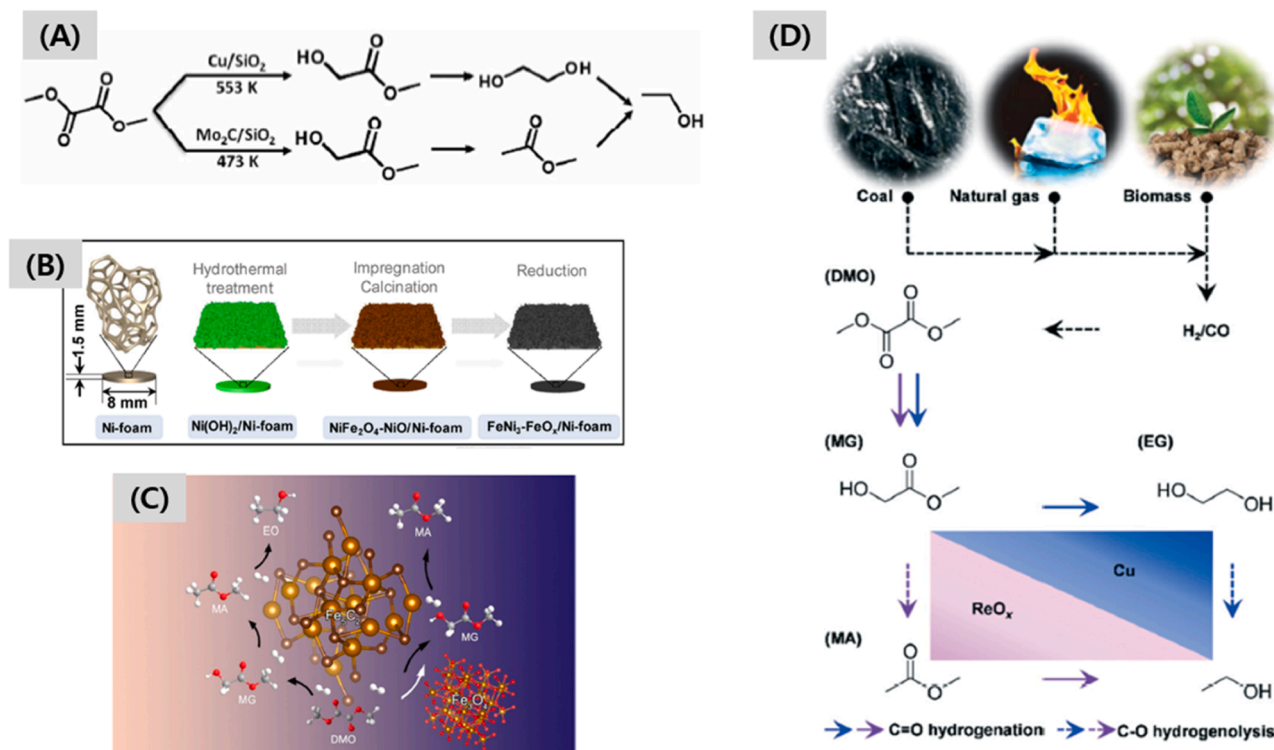

Fig. 8. (A) Reaction mechanisms of DMO hydrogenation to ethanol over Mo$_2$C/SiO$_2$ catalyst (ref. 79), (B) Catalyst preparation procedures of FeNi$_3$-FeO$_x$/Ni-foam-(550/350) (ref. 81), (C) Role of different iron phases on model Fe@C (ref. 82) and (D) Illustration of different intermediates over Re-Cu/SiO$_2$ catalyst during DMO hydrogenation (ref. 83).

as disclosed in Fig. 8 C, which were main active sites for DMO hydrogenation as proved by DFT calculations with excellent mass transfer rate due to its microsphere morphology. In addition to the active Fe_5C_2 phases, Fe_3O_4 phases were also found to be active to convert methyl glocolate (MG) to MA [82]. Furthermore, the bifunctional Re-Cu/SiO$_2$ prepared by evaporation-impregnation method formed smaller Cu nanoparticles decorated with the isolated and clustered Re nanoparticles, and it was suggested that C–O bond hydrogenolysis was more preferential on the oxophilic Re sites and hydrogenation of C═O bonds was active on the Cu sites as summarized in Fig. 8D. Especially, the Re_5-Cu_{20}/SiO$_2$ showed 100% DMO conversion and 90% EtOH selectivity for 800 h duration, where the stability was derived from the stronger electronic effects owing to Re decoration by suppressing the agglomerations of Cu nanoparticles [83]. In addition, the Cu active sites confined in MgAl layered double hydroxides (LDH) via co-precipitation method (CuMgAl-LDH) with different Mg/Al ratios showed a superior catalytic activity and stability by optimizing the microstructures of hydrotalcite, surface acidity and Cu dispersion [84].

Catalytic reduction process of carboxylic acids, particularly for acetic acid (AA), which is commercially produced by a liquid-phase homogeneous catalytic carbonylation reaction of methanol, is also attractive to further synthesize aldehydes or alcohols [85,86]. Silica-based 9Cu1In/SBA-15 containing Cu-In alloy and partial metallic Cu sites, prepared by a deposition-precipitation method, showed a higher AA conversion and ethanol selectivity. On the Cu-In mixed metal oxides, the metallic Cu nanoparticles are prone to be agglomerated into larger nanoparticles resulted in an enriched In_2O_3 nanoparticles on the catalyst surfaces during reduction step. In addition, hydrogen can be dissociated both on the isolated Cu sites and alloyed Cu-In sites, where the H$_2$ adsorption and dissociation are key factors to selectively produce ethanol from AA hydrogenation. Compared to monometallic Cu nanoparticles, Cu-In alloy can suppress the formation of ethyl acetate (EA) byproduct on account of its steric hindrance effects in the Cu-In sites by enhancing ethanol selectivity [85]. In addition, the PtSn alloy on the SiO$_2$ prepared by a modified two-step sol-gel (MTSG) method was reported to be active for AA hydrogenation, and an optimized PtSn1.6/SiO$_2$-MTSG (Sn/Pt molar ratio of 1.6) showed a higher AA conversion (98.3%) and ethanol selectivity (91.8%). On the PtSn/SiO$_2$, the Pt nanoparticles were well dispersed and large amount of Lewis acid sites was formed due to the contiguous contributions of Pt and Sn species, where the amounts of Lewis acid sites were increased with a decrease of Pt dispersion and increase of Sn/Pt ratio. The intrinsic activity (TOF$_{pt}$) was increased with an increase of Lewis acidic site per Pt atoms on account of the synergy effects of the exposed Pt nanoparticles and Lewis acid sites originated from the Sn oxides on the PtSn/SiO$_2$-MTSG [86]. Furthermore, the effects of Sn modification were also proved with RhSn/Al$_2$O$_3$ catalytic system with diverse weight ratios of Rh and Sn synthesized by impregnation method. Among the prepared catalysts, 3Rh5Sn/Al$_2$O$_3$ possessing the metallic Rh and Sn^{2+} species showed best ethanol selectivity and AA conversion. Those effects of Sn/Rh ratio were attributed to the Sn^{2+} species by providing the active sites for acetic acid adsorption and C-OH bond dissociation. In addition, the adsorbed acetyl groups suppressed the cleavages of C-C bonds due to the geometric effects and electronic modifications with the proper addition of Sn species, which eventually induced the appropriate spill-over of H$_2$ which was the key step for acetic acid conversion to ethanol [87]. The MOF-based materials have been also largely utilized as supports for AA conversion to ethanol, for example, Pt/MOF prepared by a plasma deposition method such as Pt/MIL-125-NH$_2$ showed a superior ethanol yield of 31%, where the MIL-125-NH$_2$ suppressed ethyl acetate formation due to the weak adsorption behaviors of ethanol than that of acetic acid [88]. In summary, DMO hydrogenation and AA hydrogenation to ethanol have been emerged as promising ethanol production routes. For the DMO hydrogenation, Mo$_2$C-based, Fe-based or Cu-based catalysts have been introduced by clearly suggesting catalytic reaction mechanisms, and the prevention of active sites aggregations

and formation of MA intermediate were crucial factor. For the AA hydrogenation, diverse active metal (oxides) such as Cu-In, Pt-Sn, Rh-Sn and Pt nanoparticles were proposed by revealing various effects and proper selections of active metals are highly important to enhance the desirable roles of heterogeneous catalysts.

2.4. Indirect ethanol production via tandem catalytic reaction routes

Recently, many tandemly coupled catalytic reactions through an indirect ethanol synthesis method from syngas have been largely investigated with a higher potential for good selectivity to ethanol, since one-step direct ethanol synthesis from syngas are characterized with a very lower ethanol yield even with lots of metal-based catalysts reported so far [89–94]. The syngas including CO$_2$ can be converted into ethanol and C$_{2+}$ oxygenates via DME-MA route by successive hydrogenation-dehydration-carbonylation reaction on the hybridized catalysts and the results are summarized in Table 4. The combinations of ZnAl$_2$O$_4$|H-MOR|ZnAl$_2$O$_4$ catalyst layers showed ethanol selectivity of 52% at CO conversion of ~6%, where total weight of ZnAl$_2$O$_4$ with 0.33 g and H-MOR with 0.67 g were separated by a thin quartz wool layer. The effects of catalyst-layer loading are displayed in Fig. 9 A. For example, the ZnAl$_2$O$_4$|H-MOR|ZnAl$_2$O$_4$ catalyst configuration was found to be more favored for ethanol production and the ZnAl$_2$O$_4$|H-MOR|ZnAl$_2$O$_4$|H-MOR catalyst-layer configuration was found to be better to produce ethylene, where the closer proximity between the ZnAl$_2$O$_4$ and H-MOR layer enhanced ethylene selectivity [89]. The Zn-modified MOR and pyridine-treated MOR also improved catalytic performances during one-step syngas conversion to ethanol on the layer-configuration. For example, the HMOR-20 with Si/Al ratio of 20 was also modified by ion exchange method with Zn species (Zn-HMOR-20), which was further modified with pyridine to prepare Py-Zn-HMOR-20. The CuZnAl catalyst was prepared by co-precipitation method and the hybrid CuZnAl-HZSM-5 was prepared by coprecipitation-impregnation method and the combinations of the prepared catalysts (CuZnAl-HZSM-5 + Py-Zn-HMOR-20 + CuZnAl) were tested, and the pyridine-modified Zn-HMOR-20 improved catalytic stability, CO conversion and ethanol selectivity during a long-run test for 200 h without significant deactivation due to the positive pyridine and Zn modification [90].

In addition, DME, CO and H$_2$-containing syngas can be also utilized to produce ethanol via DME carbonylation and successive MA hydrogenation by using the hybridized zeolites with Cu-based catalyst. For example, nano-sized ZSM-35 (NZ35) zeolite and auto-reduced CuZnAl were tested for DME conversion to ethanol with a dual-catalyst bed configuration consisted of 0.5 g NZ35 and 0.5 g CZA, which showed a stable DME conversion of 47.0% and ethanol selectivity of 45.6% [91]. Similarly, Cu-doped HZSM-35 prepared by an ion exchange method (Cu$_{0.55}$/HZSM-35 with 0.55 wt%Cu) and Cu$_1$-Zn$_1$-Al$_{0.1}$ (molar ratio of Cu:ZnAl = 1:1:0.1) prepared by homogeneous precipitation were subjected to one-step DME conversion to ethanol. Those catalyst combinations showed a higher DME conversion and ethanol productivity. The Cu$_{0.55}$/HZSM35 seemed to strengthen CO adsorption and led to surface enrichment of CO to accelerate CO insertion into DME which eventually increased DME conversion. In addition, better physicochemical properties of the Cu$_1$-Zn$_1$-Al$_{0.1}$ such as large specific surface area and highly dispersive Cu species can enhance the hydrogenation activity of MA to ethanol with an enlarged ethanol productivity [92]. A tailor-made microcapsule catalyst with multifunctional shell morphology was prepared by co-precipitation and hydrothermal synthesis method, where the Cu/ZnO-S-1 catalyst was mixed with MOR precursor solution including a small amount of CTAB, which was carried out by hydrothermal synthesis to prepare the microcapsule CZ@Cu-MOR catalyst (Fig. 9B). The CZ@Cu-MOR with Cu/ZnO core and modified-zeolite shell were used for one-step ethanol synthesis from DME. The larger surface area and suppressed core-to-shell interfaces with CTAB addition effectively improved mass transport and catalytic activity [93]. The
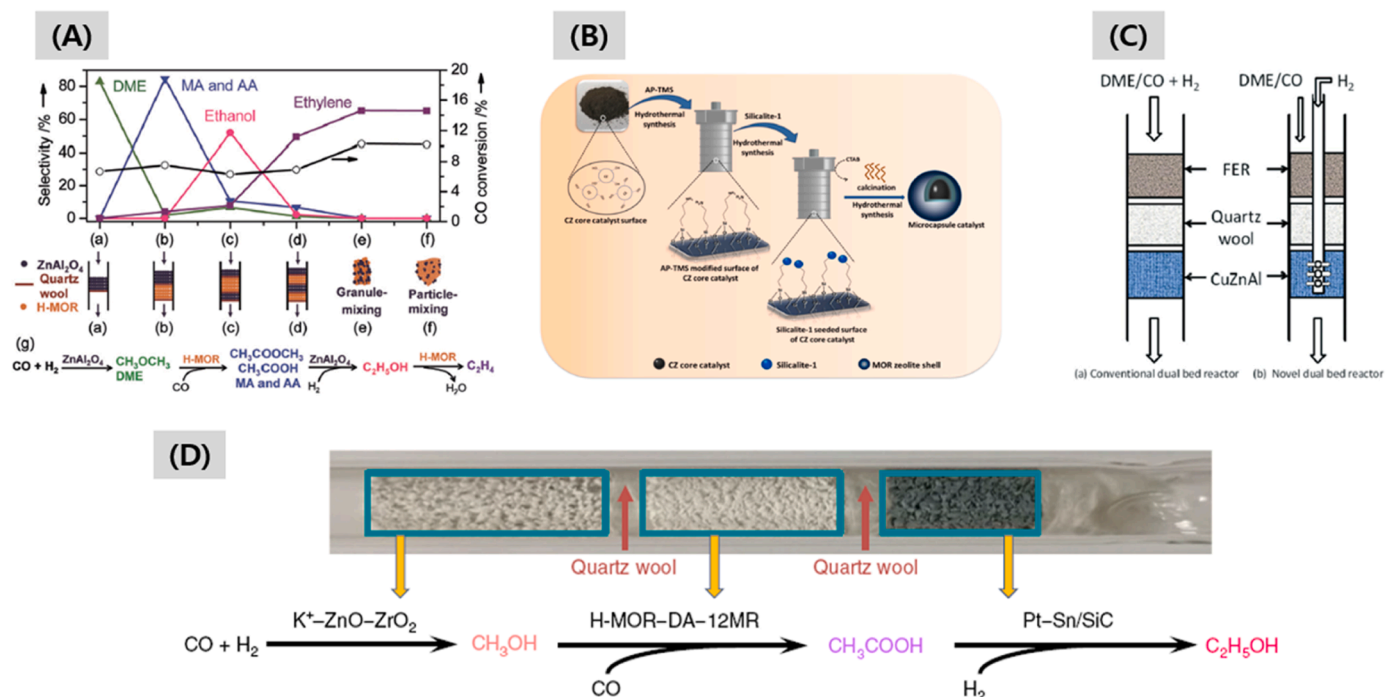
Fig. 9. (A) Effects of catalyst loading configurations and catalytic activity (ref. 89) for one-step CO conversion to ethanol, (B) Synthesis procedures of CZ@Cu-MOR catalyst (ref. 93), (C) Designs of novel rector for one-step DME conversion to ethanol (ref. 94) and (D) Compositions of triple-bed catalytic system for one-step syngas conversion to ethanol via acetic acid (AA) intermediate (ref. 95).

novel dual-bed reactor was also employed for an efficient ethanol production from the mixed gases of DME, CO and H_2, where H_2 was directly introduced into second CuZnAl catalyst through additional inside stainless steel tube as described in Fig. 9 C. The commercial FER zeolite and CuZnAl (Cu/Zn/Al(mol) = 1:1:0.1) prepared by precipitation were tested with a mixed gas of Ar/DME/CO (mole ratio of 3/4/93) and additional pure H_2 was introduced through an inlet of reactor into second stage of the dual-bed CuZnAl. At 200 °C and 1.5 MPa, ethanol selectivity of 45% at 42% DME conversion was observed by using novel dual-bed configuration by combining FER-CuZnAl catalysts [94].

Another single-pass ethanol production route from syngas was also proposed by using triple tandem catalysis including potassium-modified ZnO-ZrO$_2$ (K$^+$-ZnO-ZrO$_2$)-deposited MOR zeolite and Pt-Sn/SiC via methanol carbonylation and acetic acid hydrogenation. The K$^+$-ZnO-ZrO$_2$ was synthesized by sol-gel method, which catalyzed syngas conversion to methanol. In addition, the H-MOR-DA-12MR was prepared via pyridine treatment of the commercial MOR, Na$^+$ ion exchange, steam treatment, NH$_4^+$ ion exchange and calcination, which were active for methanol carbonylation to acetic acid. The last Pt-Sn/SiC was prepared by chemical reduction method to mediate acetic acid hydrogenation. Using the optimal K$^+$-ZnO-ZrO$_2$, H-MOR-DA-12MR and Pt-Sn/SiC as shown in Fig. 9D, the triple tandem reaction revealed a higher ethanol selectivity and CO conversion. Based on their performances, methanol synthesis was suggested as rate-determining step and a higher CO/CH$_3$OH ratio was found to be important to enhance C-C coupling reaction. In addition, H_2 molecules improved catalytic stability of MOR zeolite during methanol carbonylation, whereas CO caused poisoning effects. In conclusion, careful designs of tandem catalysts are required to improve catalytic activity, selectivity and stability due to the complexity of triple-bed catalytic system [95]. For those one-step ethanol production, various combinations of hybridized catalysts were proposed and bulk properties of those catalysts such as proximity of catalyst layers or reactor designs are also important issues.

With many efforts to produce clean ethanol from various feedstock, lots of processes and catalysts have been proposed including CO/CO$_2$ conversions to methanol/DME, carbonylation of DME and MA/AA/

DMO hydrogenation to ethanol as separate parts of whole ethanol production processes and one-step tandem reaction by CO/CO$_2$ conversion to ethanol via DME/MA route or AA route have been also largely investigated. For the CO/CO$_2$ conversion, Cu oxides, ZrO$_2$ and In$_2$O$_3$-based catalysts and solid acid catalysts such as alumina or zeolites were widely studied, and successive DME carbonylation reaction was implemented by using various MOR zeolites. The various modifications were already applied to modify MOR, for instance, Si/Al control, morphology control, addition of extra species involving metal sites or organic materials and so on. Recently, various zeolite frameworks have been also applied for DME carbonylation such as FER, ETL, CHA, SZR and RRO due to a fast deactivation of MOR. Therefore, hydrogenations of MA, DMO or AA were studied as last part of ethanol production from CO/CO$_2$ hydrogenation, where higher conversion and superior selectivity to ethanol were observed. Furthermore, one-step tandem reactions have been paid attention with well-known catalysts involving the Cu or Zn-based (Cu-ZnO-Al$_2$O$_3$) catalysts and zeolites, and the tandem catalytic reactions are beneficial in terms of process efficiency of whole energy resources.

3. Direct CO$_x$ conversion to higher hydrocarbons and higher alcohols

To produce clean liquid fuels by alternative ways to replace petroleum-based processes, CO and CO$_2$ can be hydrogenated to higher hydrocarbons through the well-known Fischer-Tropsch synthesis (FTS) reaction as briefly summarized in Table 5, which includes main side reversible reactions such as water-gas-shift (WGS) and reverse WGS (RWGS) reaction. The products formed by hydrogenation of CO/CO$_2$ can be further hydrotreated to produce gasoline (C$_5$-C$_{11}$), jet fuel (C$_8$-C$_{16}$) and diesel (C$_{10}$-C$_{20}$) which are important petrochemicals and fuels to replace conventional fossil fuels, where various Fe or Co-based catalysts have been developed by using diverse supports. The adsorbed CO is hydrogenated to form CH$_x$ intermediates on the catalyst surfaces during FTS reaction, which undergoes the C-C coupling to form C$_n$H$_m$ intermediates via carbon chain growth mechanisms. However, since the

Table 5

Summarized catalytic activities and reaction conditions for direct CO/CO$_2$ conversions to higher hydrocarbons on various heterogeneous catalysts.

Catalyst	Preparation method	Conversion	Product distribution	Reaction conditions	Reference
MOF-derived iron carbides (FeC)	MOF synthesis	88.9% (CO)	8.9% (CH$_4$), 15.4% (C$_2$-C$_4$), 9.2% (C$_5$ - C$_{10}$), 66.5% (C$_{11+}$)	300 °C, 2.0 MPa, 8000 L/(kg$_{cat}$•h), H$_2$/CO/N$_2$ (mol%) = 63.0/31.5/5.5	[98]
KFe/KIT-6	Impregnation, potassium-modification	70.8% (CO)	16.0% (CH$_4$), 15.1% (C$_2$-C$_4$), 44.6% (Olefin), 68.9% (C$_5$ +)	350 °C, 2.0 Mpa, 4000 L/(kg$_{cat}$•h), H$_2$/CO/N$_2$ (mol%) = 63.1/31.5/5.4	[99]
FeBi/SiO$_2$, FePb/SiO$_2$, FeSn/SiO$_2$, FeSb/SiO$_2$	Impregnation	60%, 44%, 53% and 47% (CO)	25%, 34%, 17% and 17% (light olefin)	350 °C, 1.0 MPa, H$_2$/CO = 1, 3.6 L/(g·h)	[100]
α-Fe$_2$O$_3$, Al$_2$O$_3$/α-Fe$_2$O$_3$, SiO$_2$/α-Fe$_2$O$_3$	Physical mixing	61.6% (CO)	33.9% (CO$_2$), 16.0% (CH$_4$), 31.2% (C$_2$-C$_4$ olefin), 16.1% (C$_2$-C$_4$ Paraffin), 36.7% (C$_{5+}$)	280 °C, 1.0 MPa, H$_2$/CO = 1, 10000 mL/(g-Fe$_2$O$_3$·h)	[101]
Fe$_2$O$_3$, χ-Fe$_5$C$_2$, θ-Fe$_3$C, Fe^0	-	66.5% (CO)	8.4% (CH$_4$), 19.1% (C$_2$-C$_4$ Paraffin), 20.5% (C$_2$-C$_4$ olefin), 51.5% (C$_{5+}$), 0.5% (Oxygenates)	350 °C, 2.0 MPa, 30000 mL/(g·h), CO/H$_2$/Ar (mol%) = 45/45/10	[102]
Fe$_2$N/Al$_2$O$_3$	Sol-gel method	-	19.2% (CO$_2$), 11.2% (CH$_4$), 22.3% (C$_2$-C$_4$ olefin), 9.1% (C$_2$-C$_4$ Paraffin), 38.2% (C$_{5+}$)	280 °C, 2.0 MPa, H$_2$/CO = 1, 30 mL/min, 7200 mL/(g·h)	[103]
Fe (0.2AC)	Incipient wetness impregnation	40.1% (CO)	21.2% (CO$_2$), 13.3% (CH$_4$), 20.6% (C$_2$-C$_4$), 61.3% (C$_5$-C$_{11}$), 4.8% (C$_{12+}$)	260 °C, 3.0 MPa, H$_2$/CO = 2, 20 mL/min	[104]
FeMn(4:1)	Co-precipitation	5.49% (CO)	15.02% (CH$_4$), 9.55% (C$_2^-$), 18.95% (C$_3^-$), 10.13% (C$_4^-$), 38.63% (C$_2$-C$_4^-$), 10.48% (C$_{5+}$), 20.72% (CO$_2$), 2.42% (Oxygenates)	260 °C, 2.0 MPa, H$_2$/CO= 1, 25 mL/min, TOS = 20 h	[105]
Fe$_3$O$_4$/CMC	solvent thermal method	50.8% (CO)	14.7% (Methane)	280 °C, 1.5 MPa, H$_2$/CO = 21000 h^{-1}, TOS = 24 h	[106]
Fe@C	MOF mediated synthesis	11.4% (CO)	8.5% (CH$_4$), 9.2% (CO$_2$), 22.0% (C$_2$-C$_4$), 60.3% (C$_{5+}$)	230 °C, 2.0 MPa, H$_2$/CO = 1, 55 dm$^3_{H_2}$/$_{CO}$/(g$_{Fe}$·h)	[107]
ε-Fe$_2$C@graphene	-	48.0% (CO), 1258 μmol$_{CO}$/(g$_{Fe}$·s)	-	340 °C, 1.0 MPa, H$_2$/CO = 1, 160 L/(g$_{cat}$·h)	[108]
1 K-MgFe/HSG	Impregnation	1825 μmol$_{CO}$/(g$_{Fe}$·s)	40.4% (CO$_2$), 23.7% (CH$_4$), 57.8% (C$_2$-C$_4$ olefin), 5.4% (C$_2$-C$_4$ paraffin), 13.1% (C$_{5+}$)	340 °C, 2.0 MPa, H$_2$/CO = 1, 144 L/(h·g)	[109]
Fe/OHC$_3$N$_4$	Ultrasonic-assisted impregnation method	-	11.4% (CO$_2$), 22.8% (CH$_4$)	280 °C, 1.5 MPa, 1000 h^{-1}, H$_2$/CO = 2 for 24 h	[110]
IO-CAT	Wet-milling process and wet impregnation method	75.4% (CO)	42.6% (CO$_2$), 9.05% (CH$_4$), 20.0% (C$_2$-C$_4$), 30.1% (C$_5$-C$_{11}$), 18.0% (C$_{12}$-C$_{18}$), 22.9%	275 °C, 1.5 MPa, 2.8 NL/(g$_{cat}$·h), H$_2$/CO = 1.0	[111]
Cat-4 h	Hydrothermal process	77.0% (CO) TOF = 0.039 s^{-1}	66.2% (C$_{10}$-C$_{20}$), 8.0% (CH$_4$), 7.8% (C$_2$-C$_4$), 84.2% (C$_5$ +), 15.6% (C$_5$-C$_{11}$), 7.8% (C$_{21}$ +)	220 °C, 2 MPa, W/F = 5.1 (g$_{cat}$·h)/mol, CO/H$_2$ = 1/2	[112]
ZSM-5/Co-Al$_2$O$_3$/M (M = monolith)	Impregnation	78.7% (CO)	10.9% (CH$_4$), 1.5% (CO$_2$), 12.1% (C$_2$-C$_4$), 75.5% (C$_{5+}$), 93.3% (C$_5$-C$_{12}$), 6.5% (C$_{13+}$), 28.9% (Paraffins), 49.8% (Isomers), 21.3% (Olefins)	230 °C, 1.2 MPa, H$_2$/CO = 2/1	[113]
Co/Y-β	Wet impregnation	93.4% (CO)	CO$_2$ = 7.0% CH$_4$ = 23.5% C$_2$-C$_4$ = 11.6% C$_5$-C$_{12}$ = 43.7% C$_{13+}$ = 5.2%	260 °C, 2 MPa, H$_2$/CO = 2, 1064 h^{-1}	[114]
CoPt/TiO$_2$–P1	Incipient wetness co-impregnation	66.3 → 48.2% (CO)	9.7% (CH$_4$), 0.8% (C$_2$), 2.7% (C$_3$), 2.7% (C$_4$), 84.1% (C$_{5+}$)	210 °C, 1.0 MPa, H$_2$/CO = 2, 4 SL/(h·g)	[115]
Co/8 C-TiO$_2$	Hydrothermal synthesis	51.3 → 44.8% (CO)	8.9% (CH$_4$), 5.9% (C$_2$-C$_4$), 85.2% (C$_{5+}$)	210 °C, 1.0 MPa, H$_2$/CO = 2, 2 SL/(g·h)	[116]
Co/C-700–8	Incipient wetness co-impregnation	30.0 ± 1.5% (CO)	45.6 ± 1.5% (CH$_4$), 16.9 ± 0.6% (C$_2$-C$_4$), 37.6 ± 1.0% (C$_{5+}$)	235 °C, 1 MPa, H$_2$/CO = 2, 3625 mL/(g•h)	[117]
CoMn-Li	Co-precipitation Impregnation method	36.7% (CO)	32.8% (CO$_2$), CO2 free: 26.9% (CH$_4$), 1.4% (C$_2^-$), 7.5% (C$_3^-$), 4.5% (C$_4^-$), 13.4% (C$_{2-4}^-$), 40.1% (C$_{5+}$)	250 °C, 0.1 MPa, H$_2$/CO = 2, 3000 mL/(g•h)	[118]
Co/NCS-500	Wetness impregnation	< 10% (CO)	4.4% (CH$_4$), 21.2% (C$_2$-C$_4$), 74.4% (C$_5^+$)	220 °C, 2.0 MPa, H$_2$/CO = 2	[119]
x%Ru/TiO$_2$-450 H	Impregnation method	-	-	200–240 °C, 2.0 MPa, H$_2$/CO/Ar = 64/32/4	[120]
10Fe3Cu1K/Al$_2$O$_3$	Co-impregnation	41.7% (CO$_2$)	26.5% (CO), 27.8% (CH$_4$), 1.6% (C$_2$-C$_4^-$), 30.3% (C$_2$-C$_4^0$), 13.8% (C$_{5+}$)	400 °C, 3.0 MPa, H$_2$/CO$_2$ = 3, 3600 mL/(g$_{cat}$·h)	[121]
Fe(2.5)	Incipient wetness impregnation	12.2% (CO$_2$)	68.9% (CO), 22.3% (CH$_4$), 8.2% (C$_2$-C$_4$), 0.3% (C$_{5+}$)	320 °C, 3 MPa, n(H$_2$)/n(CO$_2$) = 3 (CO$_2$/H$_2$/N$_2$ = 21:63:16), 300 mL/min	[122]
N-600–0	Incipient wetness impregnation	46.0% (CO$_2$)	17.5% (CO), 26.6% (CH$_4$), 22.2% (C$_{5+}$), 19.2% (C$_2$–C$_4^-$), 14.5% (C$_2$–C$_4^0$)	400 °C, 3.0 MPa, 3600 mL/(g·h), H$_2$/CO$_2$ = 3	[123]
2.5 K-CoCu/TiO$_2$	Deposition-precipitation	13.0% (CO$_2$)	34.1% (CH$_4$), 30.8% (C$_2$-C$_4$), 35.1% (C$_{5+}$)	250 °C, 5.0 MPa, 3000 mL/(g·h), H$_2$/CO$_2$/N$_2$ = 73/24/3	[124]
CoMn	Co-precipitation	-	-	265 °C, 0.5 MPa, 2000 mL/(g·h), H$_2$/CO = 0.5, H$_2$/CO$_2$/N$_2$ = 72.7/24.3/3	[125]
Na-Fe$_3$O$_4$/HZSM-5	Incipient wetness co-impregnation	22.0% (CO$_2$)	4.0% (CH$_4$), 16.6% (C$_2$-C$_4$), 79.4% (C$_{5+}$), 1.1% (C$_5$.C$_{11}$), 78.3% (C$_{12+}$)	320 °C, 3.0 MPa, 4000 mL/(g$_{cat}$·h), H$_2$/CO$_2$ = 1	[126]

Table 5 (*continued*)

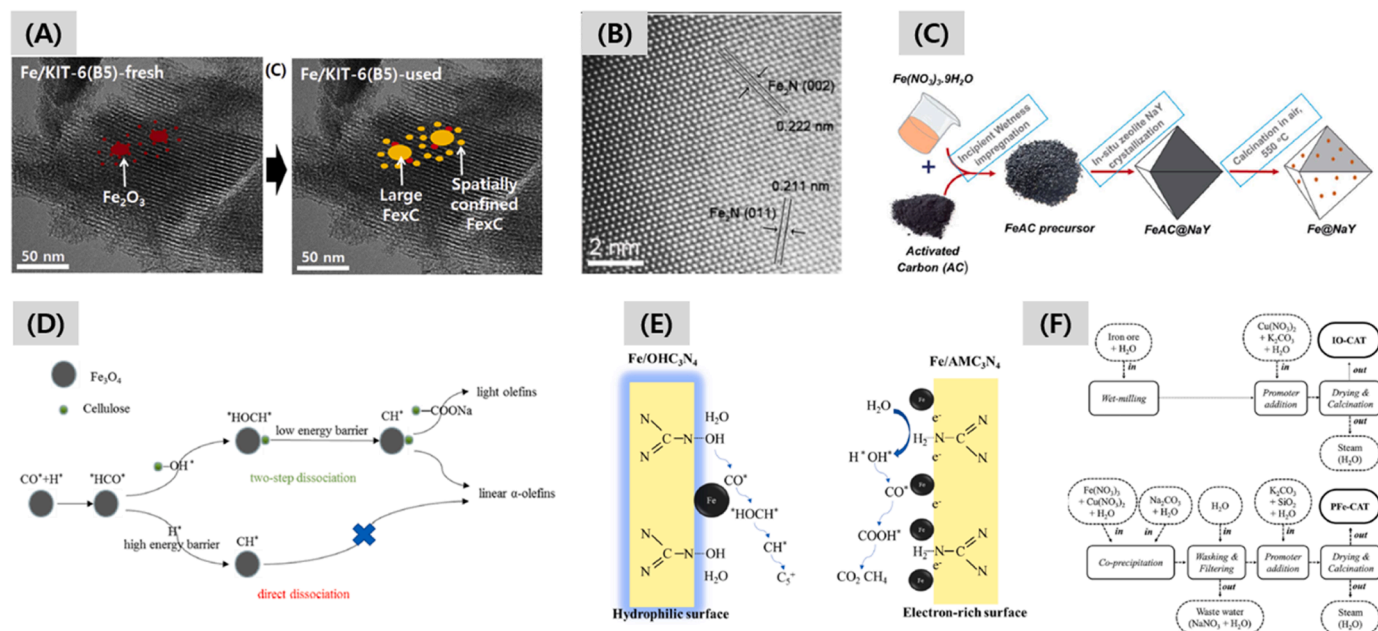| Catalyst	Preparation method	Conversion	Product distribution	Reaction conditions	Reference
NaFe + ZSM-5 + SAPO-11	One-pot process	31.2% (CO_2)	13.2% (CO), 9.2% (CH_4), 18.3% (C_{2-4}), 0.7% (C_{2-4}), 71.7% (C_{5-11}), 0.8% (C_{12+})	320 °C, 3.0 MPa, $W_{NaFe}/F = 6$ (g·h)/mol, $H_2/CO_2 = 3/1$	[127]
Fe-Zn-Zr(0.1:1:1)-T-24 h@HZSM-5	Co-precipitation + hydrothermal treatment	18.1% (CO_2)	24.0% (CO), 76.0% (hydrocarbon), 93.1% (C_{5+} isoalkane in gasoline), 3.9% (aromatics in gasoline)	340 °C, 5.0 MPa, 3000 mL/(g·h), $H_2/CO/N_2 = 72/24/4$	[128]
In_2O_3/HZSM-5(2/1)	Co-precipitation + Hydrothermal synthesis	13.1% (CO_2)	44.8% (CO), 55.2% (hydrocarbons, HC), 1.0% (CH_4 in HC), 20.4% (C_2–C_4 in HC), 78.6% (C_{5+} in HC)	340 °C, 3.0 MPa, 9000 mL/(g_{cat}·h), $H_2/CO/N_2 = 73/24/3$	[129]
In_2O_3-ZrO_2/HZSM-5 + desilicated-HZSM-5	Impregnation	7.2% (CO_2)	11.2% (CO), 68.0% (C_{5+}), 42.4% (C_{8-12} among hydrocarbons)	553 K, 4.0 MPa, $H_2/CO_2 = 3$	[130]
F–Mn–K	Organic combustion	38.2% (CO_2)	5.6% (CO), 10.4% (CH_4), 24.2% (C_{2-4} =), 3.5% ($C_{2-4}0$), 61.9% (C_{5+}), 47.8% (C_{8-16})	300 °C, 1 MPa, 2400 mL/(g_{cat}·h), $H_2/CO_2 = 3$	[131]
CoFe-0.81Na	Co-precipitation	10.2% (CO_2)	5.2% (CO), 17.8% (CH_4), 9.4% (C_2–C_4), 8.7% (C_5–C_7), 64.2% (C_8–C_{16})	240 °C, 3 MPa, 5500 mL/(g_{cat}·h), $H_2/CO_2/N_2 = 73/24/3$	[132]
15Fe–10 K/a-Al_2O_3 + P/ZSM-5	Co-impregnation Hydrothermal synthesis	36.4% (CO_2)	10.2% (CO), 9.7% (CH_4), 0.5% (C_2–C_4^-), 35.1% (C_2–C_4^0), 9.0% (non-aromatics C_5^+), 35.5% (aromatics)	400 °C, 3 MPa, 3000 mL/(g_{cat}·h), $H_2/CO_2 = 1$	[134]
NaFe + HZ(25)-Si-1 × 12%	One-pot synthesis Silylation	28.5% (CO_2)	15.0% (CO), 36.6% (aromatics including CO), 43.0% (aromatics excluding CO), 75.0% (light aromatics in total aromatics)	320 °C, 3 MPa, 4000 mL/(h·g_{cat}), $H_2/CO_2/N_2 = 12:6:1$	[135]
6.25Cu-Fe_2O_3 + HZSM-5-pt	Sol-precipitation Phase-transfer method	55.38 (CO_2)	4.41% (CO), 12.52% (CH_4), 9.39% (C_2–C_4), 15.42% (C_{5+} aliphatic), 61.94% (aromatics)	320 °C, 3.0 MPa, 1000 mL/(g·h), $H_2/CO_2/N_2 = 72/24/4$	[136]
Na-Fe@C + H-ZSM-5 0.2 M	Hydrothermal synthesis + Impregnation Hydrothermal synthesis	33.3% (CO_2)	13.3% (CO), 50.2% (aromatics in total HC) 203.8 g_{CH2} kg_{cat}^{-1} h^{-1} (STY of aromatics)	320 °C, 3 MPa, 9000 mL/(g_{cat}·h), $H_2/CO_2/Ar = 71.8:24.3:3.9$	[137]
ZnFeO$_x$-4.25Na/S-HZSM-5	One-pot synthesis +Alkaline treatment	41.2% (CO_2)	6.9% (CO), 20% (CO+CH_4), 75.6% (aromatics)	320 °C, 3.0 MPa, 1000 mL g_{cat}^{-1} h^{-1}, $H_2/CO/N_2 = 73/24/3$	[138]
6% Zn-UIO-66$_2$/Z5 (550 °C)	Hydrothermal synthesis Hydrothermal synthesis	21.2% (CO_2)	32.8% (CO), 6.2% (C_{1-2}), 1.7% (C_3), 3.0% (C_4), 0.3% (C_{5+}), 0.5% (B), 30.0% (T), 54.4% (X), 3.9% (C_{9+}), 88.8% (aromatics), 84.9% (BTX)	320 °C, 3 MPa, 4800 mL/(g·h), $H_2/CO_2 = 3/1$	[139]
ZZ/Z5–0.73	Co-precipitation + Hydrothermal synthesis	17.5% (CO_2)	23.8% (CO), 1.2% (CH_4), 14.9% (C_2–$_4^0$), 14.9% (C_2–$_4^=$), 7.7% (C_{5+}* except for aromatics), 60.3% (aromatics), 1.0% (DME+methanol)	315 °C, 3.0 MPa, 17 mL/min, $H_2/CO_2/N_2 = 72/24/4$	[140]
InZnZrOx/N25	Co-precipitation Hydrothermal synthesis	13.8% (CO_2)	19.8% (CO), 80.2% (hydrocarbons), 7.3% (gaseous hydrocarbons), 92.7% (liquid hydrocarbons), 90.6% (aromatics in liquid hydrocarbons), 2.1 (iso-paraffin in liquid hydrocarbons)	320 °C, 3 MPa, 4000 mL/(g_{ca}·h), $H_2/CO_2 = 3$	[141]
ZnZrOx + Zn/ZSM-5	Sol-gel method Hydrothermal synthesis	21% (CO_2)	92.8% (toluene + xyelene)	400 °C, 3.0 MPa, 12,000 mL/(g·h), $H_2/CO_2 = 3$	[142]
ZrO_2-Cr (8:1)/HZSM-5 @SiO_2	Sol-gel method + CO_2 supercritical drying Hydrothermal synthesis	13.9% (CO_2)	45.1% (CO), 76.8% (aromatics), 51.2% (BTX in aromatics)	390 °C, 3 MPa, 1200 mL/(h·g_{cat}), $CO_2/Ar/H_2 = 24.02/4.03/71.95$	[143]

Fig. 10. Characteristics of FTS catalysts; (A) TEM images of fresh and used Fe/KIT-6(B5) (ref. 99), (B) Fe$_2$N phases on Fe$_2$N/Al$_2$O$_3$ catalyst (ref. 103), (C) Fe@NaY preparation procedures (ref. 104), (D) Role of cellulose for CO activation and chain growth (ref. 106), (E) Functional effect of hydrophilic and electron-rich surfaces (ref. 110) and (F) IO-CAT catalyst preparation procedures (ref. 111).

hydrocarbons distributions are restricted by Anderson-Schulz-Flory (ASF) distribution, it is important to select the proper catalysts to overcome the limitations [34–36,96,97]. Various metal-based catalysts have been applied to higher hydrocarbons/alcohols synthesis, however, Fe- and Co-based catalysts have been investigated largely owing to its cheaper price and comparable activity [13,34]. Therefore, the Fe- and Co-based catalysts as traditional FTS catalysts are summarized in Sections 3.1.1 and 3.1.2, where those catalysts can produce various hydrocarbons including light olefin and paraffin. In Section 3.2, direct CO$_2$ conversions through FTS reaction are covered to maximize C$_{5+}$ productivity with the help of zeolites by the combinations of RWGS + FTS reaction (CO$_2$ hydrogenation). And the novel heterogeneous catalysts for the higher alcohols synthesis are also summarized in Section 3.3.

3.1. Direct syngas conversion to higher hydrocarbons

3.1.1. Fe-based Fischer-Tropsch synthesis (FTS) catalysts

In case of Fe-based catalysts, the optimized MOF-derived iron carbides (FeC) showed a high CO conversion even without a catalyst reduction step. The higher catalytic performances on the FeC (pyrolyzed at 700 °C for 4 h) were mainly originated from the abundant active iron carbide phases such as χ-Fe$_5$C$_2$ measured by Mössbauer analysis. Those active iron carbide phases can be easily formed on the outer surfaces of the smaller and thermally stable FeO$_x$ nanoparticles such as Fe$_2$O$_3$ and Fe$_3$O$_4$ encapsulated with thinner carbon layers by effectively suppressing the aggregations of metal nanoparticles [98]. As one of the widely applied metal oxides, the highly ordered mesoporous KIT-6 with pore diameters of 3.6 and 5.4 was used for FTS reaction by CO hydrogenation after 20 wt%Fe impregnation and successive potassium-modification (denoted as KFe/KIT-6(B5)), which showed an excellent catalytic activity and stability. The desirable effects of bimodal mesoporous structures formed by the various wall thickness were to form the spatially confined smaller iron carbides with its less aggregations. In addition, co-presence of smaller and larger iron nanoparticles revealed the better catalytic activity which were confirmed by TEM images on the fresh and used catalysts (Fig. 10A). Furthermore, the potassium-modified KFe/KIT-6 also increased CO conversion (70.8 C-mol%) and C$_5$ + selectivity (68.9 C-mol%) by suppressing WGS reaction activity [99]. In addition,

metals having lower melting points such as Bi, Pb, Sb and Sn can promote the catalytic activity on the impregnated Fe/SiO$_2$ catalyst for FTS reaction. The Sb and Sn promoters enhanced FTS reaction rate without affecting light olefin selectivity, where higher FTY (iron time yield) was observed on the FeSb/SiO$_2$ and FeSn/SiO$_2$. On the other hands, Bi and Pb promoters can also enhance FTS reaction rate by increasing light olefin selectivity on the FeBi/SiO$_2$ and FePb/SiO$_2$. Therefore, those metal promoters can change structural and electronic properties by stabilizing iron carbide phases and by preventing the aggregations of active Fe species. The new types of promoters can be migrated during a high temperature catalyst activation step and they showed several oxidation states which could facilitate CO dissociation as well [100].

Furthermore, core-shell structured iron phases were also scrutinized to verify the oxidation states of bulk irons, which were linearly correlated with iron time yield (FTY). The catalytic activity and selectivity were generally related with bulk chemical environments of the active Fe species rather than surface properties. Therefore, FTY was linearly correlated with oxidation state (OS) of Fe species and CH$_4$ yield was related with coordination number (CN) of Fe-C bonds, which suggests that small amount of carbon-rich ε-Fe$_2$C phases was found to be more effective to produce a higher catalytic activity comparing to χ-Fe$_5$C$_2$ and θ-Fe$_3$C phases [101]. Although the nanosized Fe$_2$O$_3$, χ-Fe$_5$C$_2$, θ-Fe$_3$C, and metallic Fe^0 phases can be formed with hierarchical core-shell structured catalyst, iron coordination environments mainly affected FTS performances and FTY can be linearly correlated with the average bulk iron oxidation states rather than the surface properties [102]. In addition, the active Fe$_2$C phases can be formed on alumina support derived from Fe$_2$N precursor during FTS reaction and the phases showed an improved catalytic activity, where the Fe$_2$N phases were prepared by calcination under NH$_3$ atmosphere (Fe$_2$N/Al$_2$O$_3$). The Fe$_2$N phases enhanced the formation of electron-rich and highly active Fe phases where N atoms lowered activation barriers to form Fe$_2$C phases and the Fe$_2$N phases existed on the crystalline Al$_2$O$_3$ surface as proved by TEM images in Fig. 10B [103].

Zeolites can be also utilized to prepare the active Fe phases (XAC) by simply introducing X g activated carbons and usage of NaY zeolite as shown in Fig. 10C. The optimum Fe (0.2AC) catalyst showed the highest CO conversion (40.1%) and desirable product distribution, which was

attributed to the increased surface area and enhanced porosity, and the volume of adsorbed CO was increased drastically due to the suppressed strongly adsorbed H_2 molecules. In addition, the active $Fe_2C_5(510)$ phase formed on the Fe(0.2AC) enhanced the C-C chain growths which enhanced gasoline-range hydrocarbons [104]. Furthermore, Mn promoter boosted up catalytic activity on the FeMn bimetallic oxides formed by low temperature coprecipitation method. During the catalyst calcination step, Mn species can be incorporated into the Fe_2O_3 frameworks, and the ionic radius mismatches of Mn and Fe caused the formation of lattice expansions, which resulted in the decreased crystallinity and particle size. The Mn species also stabilized FeO phases by forming the mixtures of FeMn oxides ($Fe_{1-x}Mn_xO$), which retarded the reduction period of FeO to metallic $Fe°$ by decreasing the reduction/carburization degree. The superior stability of the $Fe_{1-x}Mn_xO$ phases allowed the resistance towards carburization by forming different phase compositions of iron carbides and Mn-promoted surface basicity, which were well related with better CO dissociation behavior and resistance to sequential hydrogenation of olefins. Furthermore, the contributions of basicity and phase compositions of iron carbides with Mn promoter were responsible for a higher catalytic activity with lower olefin selectivity due to higher dispersion of nanoparticles and proper amount of active iron carbides [105].

For other cheaper and renewable catalyst preparations, hydroxyethyl cellulose (HEC) and carboxymethyl cellulose (CMC) were used to prepare Fe_3O_4/HEC and Fe_3O_4/CMC catalyst by solvent thermal method. HEC and CMC-modified Fe_3O_4 showed an enhanced hydrophilicity due to the grafted -OH and -COONa functional groups on the catalyst surfaces, which showed a higher activity to linear α-olefins and light olefins during CO hydrogenation. Especially, water-induced selective formation of CH* intermediate formed from surface hydroxyl groups of cellulose were suggested to enhance surface coverages of polymerization intermediates due to a lower energy barrier as displayed in Fig. 10D. The hydrophilic surface modifications also enhanced the transfer rate of primary products and suppressed secondary reaction where the -COONa species on the CMC increased catalytic activity and selectivity to light olefins by intensifying electron transfer ability [106]. Various Fe-containing carbon-based catalysts have been also studied for FTS reaction, and iron carbides phases formed by using MOF or graphene materials have been also known as promising candidates. The Fe@C catalysts can be prepared by MOF-mediated synthesis method followed by typical pyrolysis steps under N_2 flow. On the Fe@C catalysts, various iron phases such as ε'-$Fe_{2.2}C$ and χ-Fe_5C_2 were formed with the size of iron nanoparticles of 3.6 – 6.0 nm. The carburized Fe@C catalysts contained the hexagonal ε'-$Fe_{2.2}C$ and Hägg-type χ-Fe_5C_2

carbides phases during low temperature FTS reaction (LTFT), where the ε'-$Fe_{2.2}C$ and χ-Fe_5C_2 phases showed similar CO conversions with different product distribution in the particle sizes of 3.6 – 6.0 nm. The enhanced hydrogenation ability of the ε'-$Fe_{2.2}C$ phase showed higher methane selectivity and lower C_{5+} selectivity due to their different surface chemical environments [107]. Furthermore, the ε-Fe_2C phases were proposed as the most active phases for FTS reaction, however, the phases are unstable under typical FTS reaction conditions (> 250 °C) and it was solved by stabilizing the pure ε-Fe_2C nanocrystals confined into graphene layers (ε-Fe_2C@graphene) which showed a higher FTY of 1258 $\mu mol_{CO}/(g_{Fe}·s)$ with 48.0% CO conversion. Because of the graphene layers, the metastable and active ε-Fe_2C phases were stabilized which were confined in the graphene structures by preventing the less active carbide phases formation such as χ-Fe_5C_2 from the amorphous carbon layers [108]. As typical alkali promoters for Fe-based FTS catalysts, potassium was used on magnesium ferrite catalyst, which was prepared from honeycomb-like structured graphene (HSG) preparation followed by an impregnation of Mg, Fe and K species (denoted as *y*K-MgFe/HSG with *y* for nominal K amount). The composition-optimized 1 K-MgFe/HSG catalyst showed an excellent specific activity to hydrocarbons, where the porous HSG structures were effective to constrain the sintering of iron carbide nanoparticles and K promoter improved the carburization degree of Fe metal to enhance the adsorption and dissociation of CO in combination with Mg promoter [109]. In addition, surface modified g-C_3N_4 has been also widely studied as the carbon-based supporting materials, where iron metal oxides were doped on the g-C_3N_4 surfaces by ultrasonic-assisted impregnation method. An additional H_2O_2 treatment influenced the hydrophilicity of the g-C_3N_4 which accelerated the rate of water-assisted pathway by enhancing chain growth probability. For example, H_2O_2-treated Fe/OHC$_3N_4$ catalyst showed the lowest CO_2 selectivity of 11.4% and CH_4 selectivity of 22.8%, where the functional group modifications can also adjust the surface hydrophobicity or hydrophilicity by altering the selectivity or stability as illustrated in Fig. 10E [110]. Iron-ore-based catalysts (IO-CAT) were also synthesized by combining wet-milling and wet impregnation method to accommodate Cu and K species and wet-milling process broke down polyhedral crystallites of raw iron ore resulted in an enhanced textural property as shown in Fig. 10F. Due to the larger pore volume on the IO-CAT, the Cu and K promoters were well distributed and it showed a higher C_5 - C_{11} selectivity (~30 wt%), which was also attributed to small impurity of Al (Al_2O_3) and Si (SiO_2) and the proper acidic Al_2O_3-SiO_2 sites acted as extra active sites for hydrocracking of heavy hydrocarbons [111].
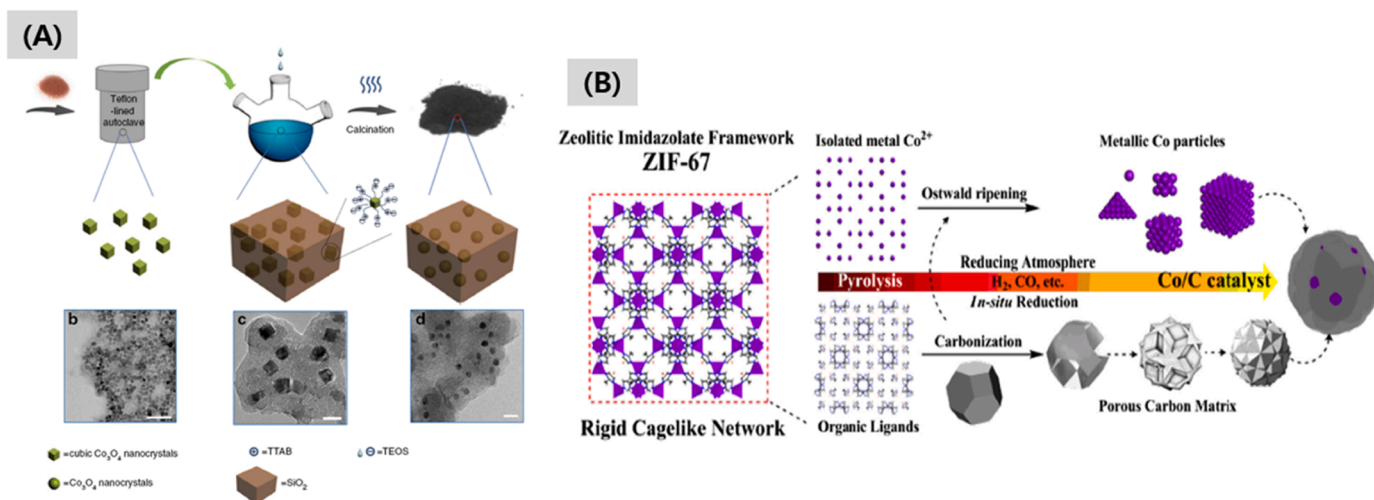

Fig. 11. Schematic diagrams of the synthesis steps of Co_3O_4 catalysts; (A) Hydrothermal process to synthesize Co_3O_4 nanocrystals embedded in mesoporous SiO_2 (ref. 112) and (B) Typical pyrolysis procedures of ZIF-67 (ref. 117).

3.1.2. Co-based Fischer-Tropsch synthesis (FTS) catalysts

The Co metal-based catalysts have been also widely studied for FTS reaction with various supporting materials, for example, typical SiO_2 support was used to prepare Co_3O_4 nanocrystals by hydrothermal process with tetradecyl trimethyl ammonium bromide (TTAB) as capping agent and Co_3O_4 crystallite sizes were controlled by hydrothermal duration with x (denoted as Cat-xh) as shown in Fig. 11A. Among the size-controlled Co nanocrystals embedded in the mesoporous SiO_2 support, the Cat-4 h catalyst having the smallest Co crystallites of 7.2 nm in size showed higher diesel-range hydrocarbons selectivity, where the smaller Co crystallites can strongly adsorb and capture a larger amount of C* species resulted in possessing enough CH_x coverages inside the confined mesoporous SiO_2 spaces to enhance chain growth probability by carbide mechanism [112]. In addition, Co-doped zeolite was utilized for FTS reaction and the gasoline-range hydrocarbons were selectively produced on the ZSM-5/Co-Al_2O_3/M (M = monolith), where the catalyst was synthesized on the cordierite monolith substrate composed of $2MgO:2Al_2O_3:5SiO_2$ after alumina washi-coating step and active material depositions and ZSM-5 coating step. The ZSM-5 on the monolith improved the gasoline-range hydrocarbons selectivity and its quality with proper olefin and isomer composition. As increasing reaction temperature, the liquid products selectivity was shifted to the smaller and light hydrocarbons and CO_2 selectivity was increased rapidly due to an enhanced WGS reaction activity. With an increase of reaction pressure, the higher selectivity to heavy hydrocarbons was observed by introducing diffusion limitations to the ZSM-5 surfaces and the isomer and olefin production were favorable at lower pressure [113]. H-β zeolite doped with rare-earth metals such as Y^{3+}, Ce^{3+} and La^{3+} was also used for FTS reaction after their introduction by ion exchange method, where the x-β (x = Y, Ce, La) was further carried out by wet-impregnation of Co nanoparticles. The rare earth metals-modified Co/x-β catalysts largely enhanced CO-metal bond strengths by weakening C-O bond strengths which resulted in an increase of gasoline-range hydrocarbons selectivity (C_5-C_{12} hydrocarbons). Particularly, the Y^{3+} species promoted the dispersion of Co species, meanwhile the Ce^{3+} intensified the reducibility which facilitated CO conversion as well. On the other hands, the strong acidity of the Co/La-β catalyst induced lower gasoline-range hydrocarbons selectivity, and the Co/Y-β was found to be best catalyst with higher catalytic activity due to its proper acidity and optimum product distribution [114]. In addition to silica, alumina or zeolite support, the active Co nanoparticles were introduced on TiO_2 support with novel Pt metal through incipient wetness co-impregnation method followed by glow discharge plasma (GDP) treatment to prepare CoPt/TiO_2–PN catalysts, where N indicates the plasma treating duration (h). After the GDP treatment to decompose cobalt precursors in a short time at low temperature, Co dispersion was improved by maintaining the reducibility of Co nanoparticles on all plasma-treated catalysts with more active sites and higher specific activity. Those excellent properties were responsible for the much higher FTS reaction rate, where the superiority of the plasma treatment of cobalt-based metal oxide catalysts seems to be beneficial to obtain higher catalytic activity [115]. In addition, the Co nanoparticles were doped on carbon-modified TiO_2 through a hydrothermal synthesis to enhance the uniformity of carbon layers by using glucose as carbon source. The thickness of carbon layers was affected by the amount of glucose, and carbon layers-containing TiO_2 (C-TiO_2) with different carbon layers (nC-TiO_2 where n is for its average thickness) was used to impregnate Co nanoparticles on the C-TiO_2 support. The carbon-coated TiO_2 structures showed the homogeneous particle distributions and high reducibility of Co nanoparticles, which were effectively tuned by controlling coating thickness and annealing temperature. In addition, positive synergy effects between hydrothermal carbon layers (HTC) and TiO_2 cores were clearly observed by the breakdown of HTC structures during reduction and reaction step, where the HTC structures induced a higher dispersion of CoO species immobilized on the C-TiO_2 [116]. The size effects of metallic Co (Co^0) have been largely studied by using carbon-based catalysts, for example,

Co-containing zeolitic imidazolate framework (ZIF-67) synthesis and its pyrolysis under Ar condition at diverse temperature (T) and duration (t) were applied to prepare Co/C-T-t catalysts as illustrated in Fig. 11B. The particle sizes of Co^0 particles on the Co/C were well adjusted in the range of 8.4 ± 1.9–74.8 ± 11.6 nm and only metallic Co species existed at higher pyrolysis temperature above 700 – 900 °C. The selectivity to products was found to be independent of the small sizes of Co nanoparticles in the range of 8.4–47.8 nm, however, methane selectivity was decreased and C_2-C_4 and C_{5+} selectivity was increased with an increase of larger particle sizes from 47.8 to 74.8 nm. The catalytic activity of the Co^0 size of 47.8 nm was related with both size effects and mass-transfer and diffusion effects, which suggested that the Co^0 size controls are important for FTS reaction on Co-based catalysts [117].

In addition, the effects of promoters on carbon-based supports were largely scrutinized, and CoMn catalysts prepared by co-precipitation with various alkali metals treatment were further used to prepare CoMn-M catalysts (M = Li, Na, K and Rb). The presence of those alkali metal promoters was found to be beneficial for the formation and stabilization of Co_2C phases, where the active phase changes from Co_2C nanospheres to Co_2C nanoprisms on the CoMn-Rb, CoMn-K and CoMn-Na were observed with an increase of ionic potential (IP). Those phenomena also caused the changes of reaction mechanisms from Co_2C nanosphere-based FTS reaction to Co_2C nanoprism-based Fischer-Tropsch to olefins (FTO) mechanism. The increased IP was observed on CoMn-Li catalyst and it showed the phase changes of Co_2C nanoprism structures to the mixtures of fcc-structured Co^0 and Co_2C nanospheres, which also caused the mechanism shift from FTO reaction on the Co_2C nanoprism to FTS reaction on the traditional Co nanoparticles. For more details, alkali metal promoters with strong polarization effects on the CoMn enhanced the polarization of Co-C bonds, which enhanced the formation of stronger Co-C bonds and CO adsorption by improving CO dissociation and by selectively forming Co_2C phases. In addition, the alkali promoters showed the stabilization effects on the Co_2C facets of (010) and (020), where the alkali metal promoter having a low IP showed two different promotion effects such as electronic effects to enhance CO dissociation and Co_2C formation and facet-stabilization effects to stabilize Co_2C nanoprisms under FTO reaction condition [118].

Nitrogen dopant can also change FTS reaction activity, and N-doped carbon supports were prepared by polydopamine (PDA)-based nanosphere synthesis followed by carbonization at T °C (NCS-T). Ultrasonic-assisted incipient wetness impregnation method was implemented to prepare Co/NCS-T catalysts followed by calcination under N_2 flow. According to carbonization temperatures, N dopant concentration on the NCS-T was controlled, and the N-doped carbon supports showed distinct merits in terms of anchoring and dispersing of Co species by showing better catalytic activity and C_{5+} selectivity. The effectiveness of N dopants was followed in the sequence of pyrrolic N > pyridinic N > graphitic N. The pyrrolic N species caused the more pronounced Co-support interactions owing to an improved electronic donation nature from pyrrolic N sites to Co species, where the intensified interactions on the Co/NCS increased the number of electron-enriched Co species. The pyrrolic N dopants promoted CO dissociation by weakening C-O bonds and by increasing the number of activated C* species by improving Co dispersion, which also confirmed the higher concentration of chain initiator (CH_2) to enhance carbon-chain growth probability. The effects of N dopants were well optimized on the Co/NCS-500, which had the higher pyrrolic N concentration and better catalytic activity [119]. Although the Fe and Co metals have been dominantly used for FTS catalysts, Ru-based catalysts can be also utilized for FTS reaction. For example, Ru/TiO_2 was reported as FTS catalysts prepared by an impregnation method with Ru loading amount of 0.5–4 wt% after reduction at 450 °C (Ru/TiO_2-450 H). With an increase of Ru loading, the Ru sizes were increased and FTS activity was enhanced, however, C_{5+} selectivity was decreased. The increased reduction degree for the larger Ru nanoparticles induced the selective methanation, and smaller
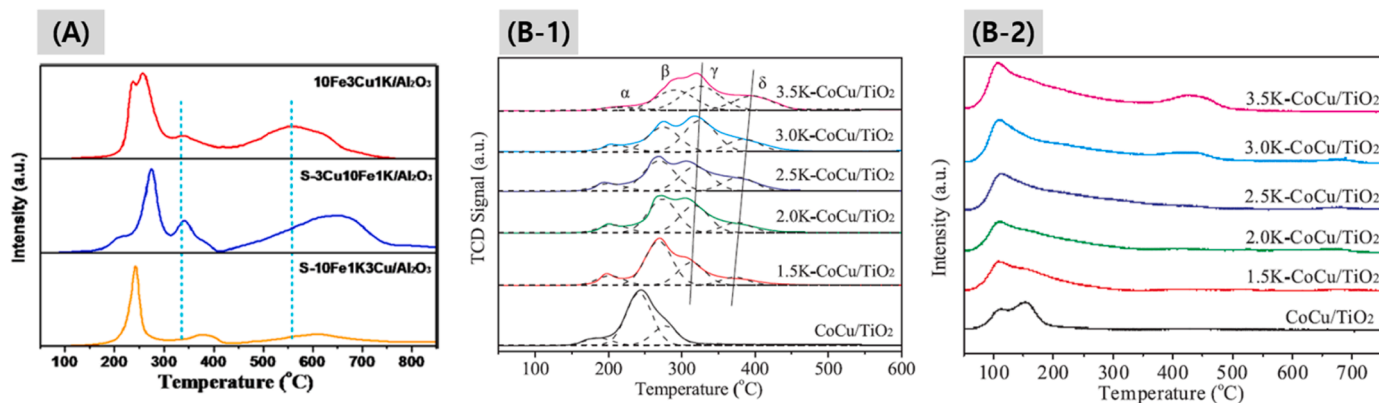
Fig. 12. (A) H_2-TPR patterns of FeCuK/Al_2O_3 catalyst (ref. 121), (B-1) H_2-TPR patterns and (B-2) CO_2-TPD patterns on CoCu/TiO_2 catalyst (ref. 124) for CO_2 hydrogenation to higher hydrocarbons.

Ru nanoparticles decorated with TiO_x coating layers showed the favorable carbon chain growth by suppressing methanation, which revealed the roles of size-dependent metal/support interactions for different product distributions [120].

In addition to FTS reaction by CO hydrogenation to produce clean fuel-range hydrocarbons, the active Fe metal oxides with various promoters such as Mn, Mo, Zn, Cu, Zr, Cr and K can be generally impregnated on the Al_2O_3 support by co-impregnation or sequential impregnation method, which can be further applied for CO_2 hydrogenation as a typical FTS catalyst. For example, 10Fe3Cu1K/Al_2O_3 prepared by co-impregnation with a nominal Fe/Cu/K mass fraction of 10/3/1 showed superior catalytic activity, where the strong interactions between Cu and Fe metal enhanced Fe oxides reduction. Therefore, the Cu species obviously improved CO_2 conversion and C_{5+} selectivity by decreasing C_2-C_4 olefin selectivity and by increasing CO_2 adsorption capacity as confirmed by H_2-TPR analysis in Fig. 12A. The enhanced

adsorption capacity of the primary olefins formed on the active sites seems to enhance secondary reaction activity to form C_{5+} products by successive hydrogenation of olefins to paraffins. In addition, the catalytic surface properties were largely affected by co-impregnation and sequential impregnation methods during the catalyst preparation step which can also change the Fe and Cu distributions [121]. Therefore, the crystallite sizes and the phases of Fe nanoparticles seem to be also interesting issues for CO_2 hydrogenation to hydrocarbons.

On an ordered mesoporous ZrO_2 metal oxide support, 10 wt% Fe metal was loaded to prepare Fe(x) by an incipient wetness impregnation method, where x represented its specific surface area. In the range of Fe sizes of 2.5 – 12.9 nm on Fe(2.5) – Fe(12.9) catalysts, overall selectivity according to Fe particle sizes was found to be opposite to the catalytic activity of FTS reaction, and the trends of hydrocarbon distributions were similar with the changes of Fe particle sizes, where the selectivity of C_{2+} hydrocarbons was increased continuously with an increase of Fe
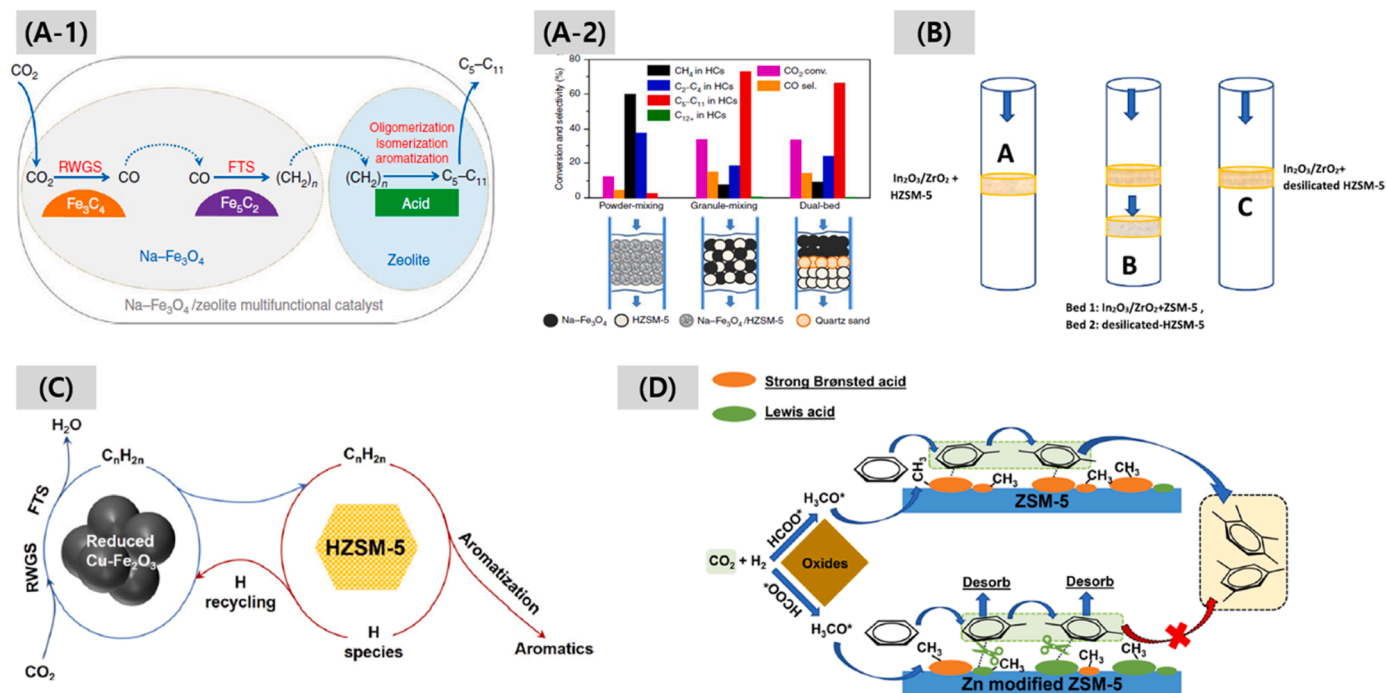

Fig. 13. (A-1) Reaction mechanisms and (A-2) Proximity effects for catalytic activity and product distribution over Na-Fe_3O_4 and HZSM-5 catalysts (ref. 126), (B) Configurations of In_2O_3/ZrO_2, ZSM-5 and desilicated-HZSM-5; configuration A was for one bed with physically mixed In_2O_3-ZrO_2/HZSM-5, configuration B was for two beds mixed with In_2O_3-ZrO_2/HZSM-5 and desilicated-HZSM-5 and configuration C was for physically mixed one bed In_2O_3-ZrO_2/desilicated-HZSM-5 (ref. 130), (C) "H-recycling" mechanism over combination of Cu-Fe_2O_3 and HZSM-5 (ref. 136) and (D) Different reaction mechanisms of CO_2 hydrogenation to aromatics on ZSM-5 and Zn-modified ZSM-5 (ref. 142).

particle sizes. The RWGS reaction and methanation are assumed as main primary reactions, which are more active on the Fe nanoparticles in the range of 6.1 – 12.9 nm. On the other hands, HCCO* species was formed more easily on larger Fe particles, which enhanced its further hydrogenation to CH_4 as a primary product. Therefore, the geometric effects or ensemble effects endowed the larger Fe particles to perform with a higher chain-growth probability in the range of 2.5 – 9.8 nm through an easy secondary FTS reaction. In addition, the enhanced CO adsorptions on large Fe particles on more terrace-like sites can also induce more facile C-C coupling reaction [122], which enhanced the heavier hydrocarbons selectivity. The MOF-derived Fe-based catalysts were investigated for CO_2 hydrogenation to hydrocarbons and the n N-K-T-t catalysts represent the pyrolysis temperature (T), its duration (t) and potassium (K), prepared by an incipient wetness impregnation method. Owing to the K promoter (N-K-600–0), C_2-C_4 olefin selectivity was improved, however, CO selectivity was also increased due to an increase of RWGS activity. The phases of Fe particles largely changed catalytic activity for CO_2 hydrogenation to hydrocarbons and proper content of Fe_3O_4 and χ-Fe_5C_2 phases were important for the enhanced catalytic activity, however the metallic Fe and θ-Fe_3C phases were easily aggregated to carry out a fast catalyst deactivation [123].

With the active metals such as Cu and Co with K promoter on TiO_2 support, CO_2 conversion was enhanced to produce long-chain hydrocarbon fuels, which was successively prepared by deposition-precipitation method with an optimum 2.5 wt%K through an incipient wetness impregnation method (2.5 K-CoCu/TiO_2). The highest C_{5+} selectivity of 35.1% was observed on the 2.5 K-CoCu/TiO_2 at a quite low CO_2 conversion of 13.0% and low selectivity to other hydrocarbons. The introduction of K promoter decreased the reducibility of K-CoCu/TiO_2 with smaller H_2 adsorption as well as increased the adsorption of CO_2 without any changes of textural and crystalline properties, which were responsible for the enhanced selectivity to heavier hydrocarbons as confirmed by H_2-TPR and CO_2-TPD analysis as shown in Figs. 12B-1 and 12B-2 [124]. In addition, Na-promoted cobalt carbide (Co_2C) nanoprisms were formed on the CoMn mixed metal oxides, and the prepared CoMn catalyst was subjected to H_2/CO feed followed by a feed gas switch by using CO_2 or CO/CO_2 mixed gas successively. For CO hydrogenation, a large fraction of olefins (70.7%) and small fraction of methane (3.1%) were observed, however, methane product was found to be dominant with CO_2-containing syngas feed. The linearly and bridged-type of the adsorbed CO molecules were observed from DRIFT analysis at the adsorption temperature of 250 °C under CO-containing gas feed, and CO_2 environment seems to inhibit CO adsorption over Co_2C surfaces, which affected the Co_2C morphology changes from nanoprisms with (101) and (020) facets to nanosphere with (111) facet by the decomposition of Co_2C phases into metallic Co. Therefore, the competitive adsorption between CO and CO_2 on the active Co_2C phases under different feed conditions was responsible for the different methane selectivity, where CO_2 environment caused the changes of active sites phases resulted in changing catalytic behaviors [125].

3.2. Direct CO_2 conversion to higher hydrocarbons on hybridized catalysts

3.2.1. CO_2 conversion to C_{5+} hydrocarbons

Typical FTS reaction has been developed to convert CO/H_2 syngas into hydrocarbons, and it can be further modified for tandem catalysis by combining it with RWGS reaction to directly utilize CO_2. Although lots of catalysts have been developed for direct CO_2 conversions via FTS reaction to produce wide range hydrocarbons, it is important to control the hydrocarbons distributions toward desirable products with the suppressed formation of CO, CH_4 and undesirable products. Therefore, many researchers have reported different catalytic systems by quantifying C_{5+} selectivity through the surface modifications of Fe- or Co-based catalysts, and the outstanding FTS catalysts for higher hydrocarbon productions are introduced briefly. In addition, CO_2 can be also

directly converted into higher hydrocarbons through CO_2 hydrogenation to methanol followed by methanol to hydrocarbons (MTH) reaction.

For the RWGS-FTS reaction route, the typical direct CO_2 conversions to gasoline-range hydrocarbons on the hybrid catalytic systems are displayed in Fig. 13A-1. The hybrid Na-Fe_3O_4/HZSM-5, where Na-Fe_3O_4 nanoparticles were prepared by one-pot synthesis, revealed a higher productivity of gasoline-range hydrocarbons with its superior stability. Based on the mechanisms for the CO_2 hydrogenation, CO_2 molecules were first reduced to CO with simultaneous formation of additional H_2 by RWGS reaction on the Fe_3O_4 sites, which was followed by CO hydrogenation to form α-olefins intermediates by FTS reaction on the separate Fe_5C_2 phases. The gasoline-range hydrocarbons were successively produced by solid acid-catalyzed reactions on the Na-Fe_3O_4/HZSM-5 hybrid catalyst through oligomerization, isomerization and aromatization and so on. In addition, the catalyst proximity effects such as powder-mixing, granule-mixing and dual-bed configuration as displayed in Fig. 13A-2 were found to be crucial factors to change catalytic activity, where the powder-mixing catalyst was found to be easily deactivated due to the poisoning of acidic sites of the HZSM-5 with Na-induced alkali metals migrations. However, the granule-mixing or dual-bed configuration of the Na-Fe_3O_4 and HZSM-5 showed a superior CO_2 conversion and desirable product distributions. Therefore, the enhanced RWGS reaction on the Fe_3O_4 seems to improve the successive olefin synthesis rate on Fe_5C_2 sites and oligomerization, aromatization and isomerization over the solid acid HZSM-5 sites with different Si/Al ratio [126]. In addition, the tandem catalysts composed of the Na/Fe_3O_4/HZSM-5 with additional commercial ZSM-5 and commercial SAPO-11 layer was further tested with a triple-bed system. At an optimum condition, CO_2 conversion of 31.2% was obtained with gasoline selectivity of 71.7% with higher isoparaffins selectivity of 38.2%. Two different zeolite layers enhanced the productions of long chain hydrocarbons by increasing oligomerization activity and altering the isomerization activity on the ZSM-5, and the hydrocarbons distributions can be controlled by changing those zeolite-bed configurations, which successively altered the catalytic activity due to the different isomerization, oligomerization and aromatization reaction [127]. The Fe-based FTS catalysts were also modified by preparing the hybridized core-shell-structured Fe-Zn-Zr@HZSM-5, where the core Fe-Zn-Zr metal oxides were synthesized by co-precipitation followed by a hydrothermal treatment and it was coated with commercial HZSM-5 layers via cladding method. The best Fe-Zn-Zr mixed metal oxides were disclosed as Fe-Zn-Zr(0.1:1:1)-T-24 h@HZSM-5 with its molar ratio of Fe/Zn/Zr = 0.1:1:1 at hydrothermal treatment with TPABr for 24 h at 180 °C. CO_2 conversion of 18.1% with lower CO selectivity of 24.0% and hydrocarbon selectivity of 76.0% (C_{5+} isoalkane selectivity of 93% among the gasoline-range hydrocarbons) were observed due to the contributions of abundant oxygen vacant sites. The improved surface properties also enhanced both the adsorption ratio of H_2/CO_2 and adsorption strength of HCOO* as well as CH_3O^* desorption rate. According to the proposed mechanisms, the FTS reaction was activated and methanol production rate was also activated simultaneously on the mixed metal oxides where the FTS reaction could be suppressed owing to the altered adsorption strengths of CO molecules. Furthermore, methanol formation was correlated with the Brønsted acidic sites on the HZSM-5 which increased C_{5+} isoalkanes selectivity, and the core-shell structures were conducive to proceed successive reactions on the acidic sites to enhance the production of desirable C_{5+} hydrocarbons [128].

In addition to the Fe-based catalysts for FTS reaction, In_2O_3-based hybrid catalysts were also active for a direct CO_2 conversion into C_{5+} hydrocarbons. In_2O_3 was found to be stable at higher temperature (> 300 °C) to form methanol intermediate for a successive MTH reaction by CO_2 hydrogenation. In_2O_3 hybridized with HZSM-5 was separately prepared by a typical co-precipitation and hydrothermal method with its mass ratio of 1:2 for In_2O_3/HZSM-5 and granular stacking configuration, which showed C_{5+} selectivity of 78.6% with suppressed CH_4 formation. Although CO byproduct was excessively formed with 44.8% selectivity

due to higher RWGS reaction activity, In_2O_3-based hybrid catalyst effectively enhanced MTH activity for selective C_{5+} hydrocarbons production. The presence of oxygen vacant sites on In_2O_3(110) was responsible for an enhanced catalytic activity, and it was also suggested that CO molecules can increase the number of oxygen vacant sites resulted in an enhanced CO_2 hydrogenation activity [129]. In addition, In_2O_3-ZrO_2 mixed bimetal oxides were prepared by impregnation of In_2O_3 on the ZrO_2. The In_2O_3-ZrO_2 metal oxides were mixed with HZSM-5 or desilicated-HZSM-5 treated with NaOH solution and various methods such as the configurations of A, B and C as displayed in Fig. 13B were applied through granule mixing method with its mass ratio of 1:1. The effects of catalyst configurations were also optimized where the "configuration B" composed of dual-bed layer of the In_2O_3-ZrO_2/HZSM-5 and desilicated-HZSM-5 showed CO_2 conversion of 7.2% with an enhanced C_{5+} selectivity of 68% (C_{8-12} selectivity 42.4%) and CO selectivity of 11.2%. The improvement of desirable products selectivity was attributed to the dual-bed configuration where the desilicated-HZSM-5 possessed higher acidic site density as well as larger pore volume after desilication, where the desilicated HZSM-5 seems to boost the oligomerization reaction of the smaller olefins produced in the first layer of In_2O_3-ZrO_2/HZSM-5 [130].

In addition to the production of C_{5+} hydrocarbons, Fe-Mn-K catalyst prepared by organic combustion method with different citric acid, oxalic acid or tartaric acid as chelating agent showed a higher jet fuel (C_8-C_{16}) selectivity of 47.8% at CO_2 conversion of 38.2% with a lower CH_4 and CO selectivity of 10.4% and 5.6%. The Fe-Mn-K catalyst possessed the uniformly organized ultrafine nanoparticles with its size of 15 nm and Fe_3O_4 and χ-Fe_5C_2 phases are mainly formed on the surfaces where Fe_3O_4 phases were found to be active for RWGS reaction to convert CO_2 into CO followed by the FTS reaction on the χ-Fe_5C_2 sites to form hydrocarbons. In addition, among various alkaline metals such as K, Na, Li or Cs, potassium promoter was found to be most effective for jet fuel production and Mn promoter was further used since Mn was known for its higher ability to enhance surface basicity or caburization [131]. Furthermore, Na-promoted CoFe alloy was also known to be efficient for jet fuel production, where CoFe-layered double hydroxides (LDH) structures were prepared by co-precipitation method and Na_2CO_3 and NaOH were mixed with metal precursors to control pH value and Na concentration was controlled by washing and filtering step. The optimal CoFe-0.81Na (0.81 wt%Na) catalyst showed CO_2 conversion of 10.2% and C_8-C_{16} selectivity of 64.2%. The role of optimal amount of Na promoter was found to enhance C-C coupling reaction to produce C_{8+} hydrocarbons as well as to suppress CO_2 methanation activity, where the Na promoter also adjusted the formation of the active metallic CoFe phases and CoO/Co phases were found to be more active for CO_2 methanation than CoFe bimetal phases as well [132].

3.2.2. CO_2 conversion to aromatics

Furthermore, aromatics such as benzene, toluene and xylene (BTX) can be also produced by direct CO_2 conversion to higher hydrocarbons, where BTX or aromatic chemicals have been widely utilized in chemical industries for diverse purposes. During RWGS reaction, CO can be produced from CO_2 which further undergoes FTS reaction to synthesize BTX by successive aromatization. The combinations of RWGS and FTS reaction for the production of heavier hydrocarbons, Fe containing metal oxides have been applied for the direct CO_2 conversion to BTX with various zeolites [133]. The Fe-based catalysts were promoted by K promoter, which has been well known to be effective to improve FTS activity, and iron metals promoted with potassium were loaded on commercial alkaline alumina (a-Al_2O_3) support by co-impregnation method (15Fe–10 K/A_2O_3). And ZSM-5 zeolite was synthesized from silicalite-1 (S-1) seed via hydrothermal synthesis and phosphorus treatment was conducted by simple ultrasonic shaking to prepare P/ZSM-5. For tandem reaction of CO_2 hydrogenation to aromatics, 15Fe–10 K/A_2O_3 and P/ZSM-5 were loaded with granule mixing configuration, which exhibited better yield of aromatics and CO_2

conversion. Alkaline Al_2O_3 seems to be better to enhance Fe-K dispersion, which effectively enhanced CO_2 adsorption and suppressed H_2 adsorption by showing superior CO_2 conversion with lower olefin intermediates. In addition, the acidic property of HZSM-5 enhanced aromatics formation, where the amount of medium-strength acidic sites were known to be effective for aromatics formation. Furthermore, the formations of medium-strength acidic sites were improved via phosphorous modification at an optimum P loading of 0.8 wt%. The granule mixture of 15Fe–10 K/A_2O_3 and P/ZSM-5 showed the best catalytic activity of 35.3% CO_2 conversion and 33% selectivity toward aromatics [134]. The acidic property of the ZSM-5 was adjusted to maximize the productivity of light aromatics on the Fe-based catalysts. The Na-Fe_3O_4 (NaFe) nanocatalysts were prepared via one-pot synthesis with 0.7 wt% Na, and the commercial H-form ZSM-5 with various Si/Al ratios (HZ(x), where x is for Si/Al ratio) was carried out by silylation treatment via a chemical liquid deposition (CLD) method. Finally, the ZSM-5 after silylation (denoted as HZ(x)-S-n × y%, where n = cycles of silylation, y = SiO_2 wt%) was mixed by granule-mixing method. The effects of Brønsted acid sites (BAS) were investigated to confirm the stronger BAS contributions for higher aromatization ability and cracking activity. Particularly, the external BAS was passivated via silylation method to control the surface acidic properties, which exhibited better selectivity towards light aromatics and xylene. For example, appropriate BAS density in the range of 54 – 154 μmol/g converted surface intermediates into aromatics, however, BAS density higher than 154 μmol/g was favored to coke formation. Therefore, the best granule combinations of NaFe and HX(25)-Si-1 × 12% exhibited the CO_2 conversion of 28.5% with aromatic selectivity of 36.6%, where light aromatics selectivity was found to be 75.0% among aromatic products [135].

Aside from zeolites, the surface properties of Fe catalysts can be modified by additions of metal promoters, where Cu-promoted Fe_2O_3 (nCu-Fe_2O_3, n = molar concentration of Cu) was synthesized by sol-precipitation method and HZSM-5 was synthesized by phase-transfer method with 6.25Cu-Fe_2O_3 showed desirable catalytic activity with CO_2 conversion of 55.4% and aromatics selectivity of 61.9% (BTX selectivity 54.2%). The superior catalytic activity was obtained by granule mixing method of 6.25Cu-Fe_2O_3 and inter-crystalline mesoporous HZSM-5, which was attributed to an easy adsorption of reactants and intermediates due to appropriate interactions between Cu and Fe by forming favorable sites such as oxygen vacant sites and iron carbides for CO_2 adsorption and FTS reaction through "H recycling" mechanisms. The "H recycling" between iron oxides and zeolite as described in Fig. 13C suggested that H species from HZSM-5 was diffused into the interfaces of metal oxides followed by successive reactions with CO_2 adsorbed on oxygen vacant sites by enhancing RWGS as well as FTS activity to replenish the surface C_2H_4 intermediates for the continuous aromatization reaction. Therefore, the properly formed desirable active sites on 6.25Cu-Fe_2O_3 with the help of Cu promoter and mesoporous HZSM-5 caused the better aromatics production rate [136].

Aside from the Fe-based metal oxides, MOF-derived catalysts have been also largely utilized for direct BTX synthesis from CO_2 with hollow-type H-ZSM-5. Hydrothermally synthesized Fe-containing MOF material was pyrolyzed followed by Na impregnation to produce Na-Fe@C catalyst with 0.47 wt%Na. The H-ZSM-5 was synthesized by a hydrothermal synthesis, which was subjected to being immersed into NaOH solution with various NaOH concentration to produce the hollow morphology of H-ZSM-5-X (where, X = NaOH molar concentration). The superior catalytic activity was observed by granule mixing configuration composed of Na-Fe@C and H-ZSM-5–0.2 M after optimization of NaOH solution. By using Na-Fe@C catalyst, alkene intermediates were generated where the Na promoter enhanced the formation of Fe-C bonds derived from CO_2 dissociation owing to the electron donating property of Na promoter. Besides, Lewis basic C=C double bond adsorptions were inhibited on the Na-Fe@C with basic surface properties by Na depositions. The NaOH-treated ZSM-5 was conducive to modulate the acidic density and strength which led to the conversions of alkenes

produced by Na-Fe@C surfaces into aromatics via dehydrogenative aromatization mechanisms and the hollow morphology of the ZSM-5 was helpful for the faster diffusion of alkenes intermediates to acidic sites of the ZSM-5. In case of Na-Fe@C, the generated H species by dehydrogenation and aromatization reaction was adsorbed successfully by accelerating the aromatics formation rate by overcoming the thermodynamic barrier [137]. The effects of Na promoter were verified after preparing spinel-type $ZnFeO_x$ catalyst by adjusting pH value with NaOH solution ($ZnFeO_x$-Na). On the optimal $ZnFeO_x$-4.25Na and nanocrystalline ZSM-5 (S-HZSM-5) with its mass ratio of 1:2 and granule-stacking configuration, CO_2 conversion and aromatics selectivity were enhanced to 41.2% and 75.6%, respectively. CO_2 was converted to CO by RWGS reaction on Fe_3O_4 sites followed by the formation of olefins on the active Fe_5C_2 sites by FTS and successive aromatization reaction on the nanocrystalline S-HZSM-5 zeolite. The Na promoter largely altered Fe phases where a higher Na content led to the selective formation of Fe_5C_2 phases with decreased Fe_3O_4 phases. Proximity of catalysts was also found to be crucial by altering ZSM-5 surface properties due to the migrations of Na ions, which resulted in decreasing acidic site with fast catalytic deactivation. Therefore, close proximity between metal oxides and zeolite was found to be ineffective to aromatics production and the best catalytic activity was obtained by a granule-stacking configuration. In addition, the presence of Zn promoter also enhanced the reducibility of iron oxides which was helpful to form more active Fe phases by forming smaller and stable Fe nanoparticles with the formation of spinel structure $ZnFeO_x$ phases [138].

For CO_2 hydrogenation to BTX formation, Zr-MOF precursors were also investigated after preparing UIO-66 MOF material synthesized by a hydrothermal method and sequential mixing with M metal oxides (M = ZnO, Ga_2O_3 or In_2O_3) with xwt% of single metal oxide in the MOF catalyst (x%M-UIO-66). The UIO-66 containing Zr core metals was found to be favored to selective methanol synthesis by CO_2 hydrogenation, where the methanol was successively aromatized on the acidic sites of zeolites [43]. Especially, the palygorskite was synthesized by acidification, which was used to prepare palygorskite-based HZSM-5 by adding palygorskite precursor into the synthetic gel of zeolite followed by a hydrothermal synthesis to form Z5 catalyst. The highest BTX selectivity was observed by using the physical mixture of 6% Zn-UIO66$_2$/Z5 (calcined at 550 °C) with its weight ratio of 2, where the mixed hybrid catalyst showed BTX selectivity of 84.9% at CO_2 conversion of 21.2%. The Zn-doped UIO-66 catalyst possessed sufficient active sites for CO_2 hydrogenation, and CO_2 adsorption energy on oxygen vacant sites on the Zn-doped UIO-66 was found to be more desirable to activate CO_2 molecules, which were confirmed by DFT calculation. In addition, the oxygen vacant sites were improved by a proper addition of Zn species, which enhanced the transfer rate of surface intermediates including HCOO* and H_3CO* from Zn-UIO-66 to Z5 surfaces. During CO_2 hydrogenation and methanol aromatization, HCO* hydrogenation to H_2CO* and cyclization of C_6H_{10} and C_2H_4 to form C_7H_{14} were also suggested as crucial rate determining steps (RDS) [139].

For CO_2 hydrogenation to methanol, ZnZrOx mixed metal oxides were reported as effective catalysts [43,45–47], and the ZnZrOx was further investigated for aromatics production by CO_2 hydrogenation with the help of chain-like nanocrystal HZSM-5 zeolite. The ZnZrOx (ZZ) and ZSM-5 were prepared by co-precipitation and hydrothermal synthesis method by using n-octyltrimethoxysilane. Especially, the chain length along with b-axis of ZSM-5 with 0.73 μm (Z5–0.73) was synthesized by micelles generated from organosilane by selectively forming (010) crystal plane. In addition, the larger amount of Brønsted acid sites with mesoporous structures were responsible for an excellent catalytic activity, where the proper b-axis length was helpful to produce para-xylene. In addition, oxygen vacant sites on the ZZ with well-controlled acidic sites on the Z5–0.73 revealed a higher CO_2 conversion of 17.5% with 60.3% aromatics selectivity with suppressed CH_4 formation [140]. Furthermore, In_2O_3 was introduced on the ZnZrOx via coprecipitation (InZnZrOx) or impregnation method (In-ZnZrOx) with a

fixed In metal content of 10 wt% based on the weight of ZnZrOx. Furthermore, nano-ZSM-5 (NZ5) was synthesized by a seed-induced template-free method and the combination of the InZnZrOx solid solution and NZ5 showed aromatic selectivity of 90.6% at CO_2 conversion of 13.8% due to abundant oxygen vacant sites and surface basic sites. The oxygen vacant sites seem to be necessary to active CO_2 and In_2O_3 containing metal oxides were also effective to form oxygen vacant sites by stabilizing HCOO* and H_3CO* intermediates and by suppressing RWGS reaction, where the InZnZrOx having an optimal reducibility was responsible for the suppressed excessive hydrogenation of CO_2 to form CH_4 byproduct. In addition, the shorter pore channels with more abundant acidic sites on the NZ5 can also improve the diffusion of aromatic products resulted in showing enhanced aromatics productivity [141]. On the other hands, Zn-modified ZSM-5 with ZnZrOx metal oxides prepared by sol-gel method was applied to improve toluene and xylene selectivity. The H-ZSM-5 was synthesized by a typical hydrothermal method with different Si/Al ratio, and Zn metal was impregnated to prepare Zn/ZSM-5. A lower Si/Al ratio of the ZSM-5 was favored to increase CO_2 conversion and Zn metal oxide induced better production of toluene and xylene, where Zn species altered the acidic properties by forming Zn-induced Lewis acid sites in the forms of Zn $(OH)^+$ and $[Zn-O-Zn]^{2+}$ phases. The dehydrogenation activity of C_{1-4} alkanes was promoted by the addition of Zn species by adjusting their intermediate desorption and by controlling the ratio of strong/weak acidic sites and BAS/LAS sites as displayed in Fig. 13D. Therefore, an excessive alkylation was successively prevented and the active acidic sites were regenerated to produce more aromatics [142]. H-form ZSM-5 was further modified with core-shell-structured zeolite by a chemical liquid deposition (CLD) method to passivate the external BAS with SiO_2 shells, which was denoted as HZSM-5 @SiO_2. Meanwhile, ZrO_2-Cr aerosol was prepared by a sol-gel method which was physically mixed with HZSM-5 @SiO_2 with a weight ratio of 1:2. The effects of silylation were found to effectively block the external BAS, which inhibited the further alkylation of light aromatics by increasing BTX selectivity. Aerosol catalyst was also beneficial due to its larger surface area and copious oxygen vacant sites, and the combination of ZrO_2-Cr with an appropriate Zr/Cr ratio of 8:1 and properly coated HZSM-5 @SiO_2 caused a superior aromatics selectivity of 76.8% [143].

In summary, various heterogenous catalysts with active metals can effectively convert CO or CO_2 to liquid hydrocarbons with their different product distributions. The FTS reaction for CO conversion to hydrocarbons, Fe or Co-based catalysts have been largely studied, where the preservation of original active Fe phases was crucial to suppress their aggregations and to enhance catalytic stability. Potassium promoter on the Fe-based catalysts with other metals such as Sn, Mn or Mg have been also found to be effective for FTS reaction. In addition, ε-Fe_2C, Fe_2C_5 or Fe_2N phases were suggested as the active sites for CO_x hydrogenation to hydrocarbons, which can be properly controlled by catalyst preparation steps. The surface of those catalysts can be modified with various functional groups to adjust surface hydrophilicity, which largely altered catalytic activity and stability. On the Co-based catalysts for FTS reaction, the sizes and phases of metallic Co^0 were found to be important to control product distributions, and the rare earth metals were utilized as promoters to enhanced catalytic activity, and the Co_2C nanoprism structures and N-doped supports including pyrrolic N species also revealed the effective catalytic performances for CO_x hydrogenation to hydrocarbons. Direct CO_2 conversion can be realized by combination of metal oxides, especially Fe-based or In/Zr-based catalysts, and ZSM-5 zeolite. Metal oxides catalyst played critical roles to enhance RWGS or hydrogenation activity followed by carbon chain growth on acidic sites of zeolite. Typically, two routes seem to be possible to convert CO_2 to C_{5+} hydrocarbons including (1) RWGS + FTS and (2) CO_2 hydrogenation to methanol and MTH reaction. Similarly, in case of CO_2 to BTX, two routes are possible as (1) RWGS + FTS and aromatization and (2) CO_2 hydrogenation to methanol and aromatization which is highly analogous to the direct CO_2 to hydrocarbons. The phases of those metal oxides

Table 6

Summarized catalytic activities and reaction conditions for direct CO/CO_2 conversions to ethanol or higher alcohols on various heterogeneous catalysts.

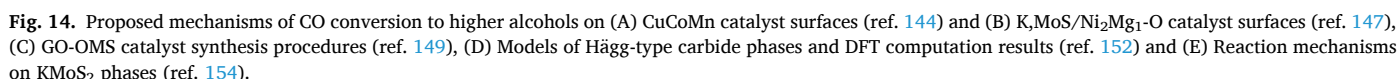| Catalyst	Preparation method	Conversion	Product distributions	Reaction conditions	Reference
$CuCoMn_{1.5}$	Co-precipitation	29.7% (CO)	46.2% (ROH), 29.6% (methanol), 45.4% (ethanol), 16.4% (propanol), 7.2% (butanol), 1.4% ($C_{5+}OH$)	270 °C, 2.5 MPa, 7500 h^{-1}, $H_2/CO = 2$	[144]
Co-Cu	Precipitation method	6.0% (CO) at TOS = 80 h	41.2% (oxygenates), 28.7% (hydrocarbons)	280 °C, 6.0 MPa, 12000 $mL/(g_{cat} \cdot h)$, $H_2/CO = 1$	[145]
Mo/MMO-2	Co-precipitation	8.73% (CO)	52.6% (C_{2+} alcohols), 0.71 $g/(g_{Mo} \cdot h)$ (C_{2+}), 64.9% (alcohola), 9.3% (hydrocarbons)	350 °C, 5.0 MPa, 3000 mL/ ($g_{cat} \cdot h$)	[146]
K,Mo/Ni_2Mg_1-O	Incipient wetness impregnation	9.9% (CO)	56.1% (alcohols)	350 °C, 5.0 MPa, 3000 mL/ ($g_{cat} \cdot h$), $CO/H_2/N_2 = 45/45/10$	[147]
$K_{0.5}$-($Ni_1Mo_{0.25}$) Si-PS	Incipient wetness impregnation	6.6% (CO)	43.8% (ROH), 65.4% (C_{2+}-OH)	240 °C, 3.0 MPa, 3000 mL/ ($g \cdot h$), $n(H_2)/n(CO) = 1$	[148]
Co/3GO-OMS	Impregnation method	19.9% (CO)	43.4% (methanol), 22.4% (ethanol), 25.9% (C_3-C_5 OH), 8.3% (others)	225 °C, 3.0 MPa, $H_2/CO/N_2 = 6/3/1$, 10800 $mL/(g_{cat} \cdot h)$	[149]
3R3M/UiO-66	Co-impregnated	16.8% (CO)	2.4% (CO_2), 29.6% (CH_4), 1.5% (methanol), 25.2% (ethanol), 23.2% (C_2^+ hydrocarbons), 43.2% (C_2^+ oxygenates), STY(C_2^+ oxygenates) = 200.1 g/(kg·h)	300 °C, 3.0 MPa, $H_2/CO = 2$	[150]
10Co5Ce/CNT	Impregnation method	30.6% (CO)	38.6% (ROH), 39.6% (methanol), 29.7% (ethanol), 20.2% (propanol), 8.6% (butanol), 1.9% (C_5OH), STY (total alcohols) = 343.7 $mg/(g_{cat} \cdot h)$	270 °C, 2.5 MPa, 10000 $mL/(g_{cat} \cdot h)$, $H_2/CO = 2$	[151]
3DOM Cu_2Fe_1	Colloidal crystal template (CCT) method	58.4% (CO)	5.2% (methanol), 26.1% (C_{2+} oxygenates), 57.2% (hydrocarbons), 11.5% (CO_2)	260 °C, 4.8 MPa, $H_2/CO = 1$, 2000 h^{-1}	[152]
$LaCo_{0.9}Mn_{0.1}O_3$	Citrate acid complex method	18.7% (CO)	23.0% (ROH), 32.9% (CH_3OH), 67.1% (C_{2-5}-OH)	270 °C, 3.0 MPa, $H_2/CO/N_2 = 6/3/1$, 4000 mL/(g·h)	[153]
M5	Precipitation	7.8% (CO)	22.9% (hydrocarbons), 31.1% (CO_2), 46.0% (oxygenates), 6.7% (methanol), 13.7% (ethanol), 20.6% (C3 +OH), 5.0% (others)	300 °C, 8.7 MPa, 4500 mL/ (g·h), $H_2/CO = 1$	[154]
Na-Co/SiO_2	Incipient wetness impregnation	18.8% (CO_2)	12.50% (methanol), 62.8% (ethanol), 13.50% (propanol), 9.27% (butanol), 1.92% (C_5OH)	250 °C, 5.0 MPa, 4000 h^{-1}, $H_2/CO = 3$	[155]
2%Na-Co/SiO_2-C	Impregnation	53.2% (CO_2)	12.9% (among alcohols, 52.8% (ethanol), 91.3% (C_2+OH), STY = 1.1 mmol/(g·h)	310 °C, 5.0 MPa, $H_2/CO_2 = 3$, 6000 $mL/(g_{cat} \cdot h)$	[156]
Catalyst	Preparation method	Conversion	Product distributions	Reaction conditions	Reference
$CoAlO_x$-600	Co-precipitation	-	92.1% (ethanol)	200 °C, 4.0 MPa, $H_2/CO_2 = 3$	[157]
$Co_{0.52}Ni_{0.48}AlO_x$	Coprecipitation	-	85.7% (ethanol), yield (ethanol) = 15.8 $mmol/g_{cat}$	200 °C, 4.0 MPa, $H_2/CO_2 = 3$	[158]
Cu@Na-Beta	Hydrothermal	-	yield (ethanol) = ~14%	300 °C, 2.1 MPa, 12,000 mL/ (g·h), $H_2/CO_2 = 3$	[159]
CZA(1)/K-CMZF (1)	Precipitation + power mixing	42.3% (CO_2)	13.8% (CO), 67.6% (hydrocarbons), 1.3% (methanol), 17.4% (C_2+OH) 90.2% (C_2+OH/ROH), STY (C_2+OH) = 106.5 mg/(g·h)	320 °C, 5.0 MPa, 6 L/($g_{cat} \cdot h$), $H_2/CO_2 = 3$	[160]
0.1 wt%Pd/ Fe_3O_4	-	3.9% (CO_2)	77.5% (CO), 17.8% (ethanol), 4.7% (propanol), STY = 846 $mmol_{EtOH}/(g_{Pd} \cdot h)$	400 °C, 0.1 MPa, F/W = 60 L/ ($g_{cat} \cdot h$), $H_2/CO_2 = 4$	[161]
FeNaS-0.6	Precipitation	32.0% (CO_2)	20.7% (CO), 12.8% (C_2+OH), 1.2% (CH_3OH), 98.8% (C_2+OH), STY (C_2+OH) = 78.5 $mg/(g_{cat} \cdot h)$, STY(alcohols) = 80.5 $mg/(g_{cat} \cdot h)$	320 °C, 3.0 MPa, 8000 mL/ ($g_{cat} \cdot h$), $H_2/CO_2/N_2 = 72/24/4$	[162]

can be also well designed by containing alkaline or transition metal promoters. Oxygen vacant sites were also known to play critical roles, particularly CO_2 hydrogenation step during methanol formation, where the formation of oxygen vacant sites was largely affected by the catalyst modification methods. For the above both routes, ZSM-5 was largely used for carbon chain growth and acidic sites were for an enhancement of the desirable products formation. For example, an introduction of metal species as well as surface silylation method can be implemented to cover the surface acidic sites by minimizing side reactions and the ZSM-5 morphology can alter diffusion path, where the proximity can significantly change tandem reaction activity such as granule mixing, physical mixing or dual-bed system.

3.3. Direct syngas conversions to higher alcohols

Direct synthesis of higher alcohols from CO/CO_2 hydrogenation on various catalysts are summarized in Table 6. The primary merit of indirect synthesis of higher alcohols including ethanol is its higher selectivity to targeted product. In addition, product distributions of direct higher alcohol synthesis by CO_x hydrogenation are quite broader with dominant C_{3+} alcohols. Since the higher alcohols are also valuable chemicals, the heterogeneous catalysts for higher alcohols synthesis from syngas are covered in the section with summarized results in Table 6.

Transition metal oxides including Cu, Co, Mn and Al metal prepared

by co-precipitation method were investigated for CO hydrogenation to oxygenates and higher alcohols, where the CuCoMn metal oxides having layered double hydroxide (LDH) structures with spherical-platelike morphology revealed a higher catalytic activity owing to its combined hierarchical structures of CuMn-rich spheres with Co dominant nanosheets. The partially oxidized Cu^+ species formed by stronger interaction of Cu and Mn oxides with additional synergetic effects between Cu^+ and metallic Co sites effectively enhanced CO insertion rate with the help of bridge-bonded CO adsorption on the metallic Co sites as well as linearly-bonded CO adsorption on the Cu^+ sites, resulted in a higher ethanol selectivity and productivity of higher alcohols. As displayed in Fig. 14A, the proposed reaction mechanisms were the simultaneous activations of CO and H_2 to form surface CH_x species followed by non-dissociative CO insertion and its stepwise hydrogenation to ethanol. The non-dissociative CO (CO*) insertion step into the CH_x intermediate is critical step with the help of MnO promoter, and the optimized $CuCoMn_{1.5}$ revealed an improved CO conversion and alcohol selectivity [144]. Other LDH-based catalysts were utilized to accommodate Co-Cu bimetallic sites prepared by precipitation method using Cu, Co, Zn and Al precursors at affixed Co:Cu ratio of 2. The fast phase separation and sintering of Cu^0 nanoparticles were ascertained within 2 h for activity test. On the other hands, conversion of metallic Co^0 into Co_2C happened as carbidization and sintering during first 40 h reaction, which was responsible for the decreased selectivity of hydrocarbons. After 40 h on stream, a stable activity was observed by the intergrowths of Cu^0

Fig. 14. Proposed mechanisms of CO conversion to higher alcohols on (A) CuCoMn catalyst surfaces (ref. 144) and (B) K,MoS/Ni$_2$Mg$_1$-O catalyst surfaces (ref. 147), (C) GO-OMS catalyst synthesis procedures (ref. 149), (D) Models of Hägg-type carbide phases and DFT computation results (ref. 152) and (E) Reaction mechanisms on KMoS$_2$ phases (ref. 154).

nanoparticles with Co$_2$C nanoparticles. It was reported that the mechanisms for higher alcohol synthesis begin with CO dissociation on Co$_2$C surfaces followed by combining with atomic hydrogen, which forms C$_x$H$_y$ intermediates. Therefore, the active CO adsorption sites on both metallic Cu^0 and Co$_2$C facets can facilitate the CO insertion into C$_x$H$_y$ intermediates, which enhanced higher alcohols selectivity. The oxygenates formation by CO$_x$ hydrogenation was attributed to multi-functional properties of Co$_2$C/Cu^0 interfaces [145], and the roles of promoter were explained differently on the LDH catalysts by forming different intermediates.

In addition, Mo containing catalysts have been also paid attention and the active Mo species was loaded on various metal oxides. For example, the KMoS phases were formed on NiMgAl trimetallic oxides (MMOs), where the MMO was synthesized by co-precipitation method and treated with KOH followed by grinding with K$_2$CO$_3$ and successive calcination (K,Mo/MMO). The formation of C$_{2+}$ alcohols was enhanced by suppressing surface acidity and by increasing basic sites, where the optimal K,Mo/MMO showed the highest sulfidation degree, appropriate acidity and basicity as well as higher ratio of octahedral Mo species [146]. The KMoS phases were effectively confined in the mesoporous NiMg bimetal oxides, and CO hydrogenation to higher alcohols was enhanced due to the adjusted Mo-Ni interactions by increasing specific surface area and MoS$_2$ dispersion with its appropriate size and abundant double-layer MoS$_2$ stacking. By using NiMg bimetal oxides (Ni$_2$Mg$_1$), MoO$_3$/Ni$_2$Mg$_1$ catalyst was prepared by an incipient wetness impregnation method and grinding with K$_2$CO$_3$ and successive calcination was

eventually conducted to prepare K,Mo/Ni$_2$Mg$_1$-O. The ordered mesoporous Ni$_2$Mg$_1$ structures can modulate Mo-support interactions and MoS$_2$ sizes, which intensified the synergism between Ni$_2$Mg$_1$ and Mo to form larger active NiMoS sites. The abundant NiMoS active phases and double-layers MoS$_2$ were characterized on the K,Mo/Ni$_2$Mg$_1$-O, which was responsible for an enhanced catalytic performances and the roles of each phases were summarized in Fig. 14B [147]. In addition, the K-promoted Ni-Mo catalyst was prepared by ammonia evaporation method by using silica support followed by an incipient wetness method with K$_2$CO$_3$ at different K content (denoted as Kx-(Ni$_1$Mo$_{0.25}$)Si-PS). The observed superior catalytic activity was derived from higher dispersion of nanoparticles and intensified metal-support interactions with minority of metallic Ni^0 and the majority of Mo^{3+} sites [148].

Aside from the metal oxide-based catalysts, carbon-based supports such as metal-organic framework (MOF), graphene oxide and carbon nanotube (CNT) have been also largely reported for direct CO hydrogenation to higher alcohols. In addition, composites of graphene oxide (GO) and ordered mesoporous silica (OMS) supported with cobalt metal oxides (xGO-OMS, where x for weight percent of GO) were introduced for direct CO hydrogenation as shown in Fig. 14C, where the Co metal was impregnated over xGO-OMS to prepare Co/xGO-OMS. The maximum CO conversion was obtained on Co/3GO-OMS with the synergy effects of GO, where the GO improved metal dispersion by promoting CO adsorption and disassociation on Co nanoparticles. In more details, the electron donor effects of GO were attributed to carbide formations with an increased Co$_2$/Co ratio, which further enhanced

higher alcohols selectivity. The excessive GO addition caused the stacks of GO which covered active sites by weakening the electron donor effects of GO resulted in lower C_{2+} alcohols yield, and an optimum GO content was proposed [149]. The MOF structures of UiO-66 with co-impregnated Rh and Mn metals (3R3M/UiO-66 with 3 wt% of Rh and Mn) revealed a higher catalytic activity for CO hydrogenation to higher alcohols. The ordered microporous MOF structures were found to be beneficial to disperse active metals and to form stronger interactions between Rh^+ and MnO_2 at an optimal Mn/Rh ratio of $\sim$ 1. The best catalytic activity and selectivity at a proper Mn/Rh ratio was attributed to the enhanced CO adsorption on the active Rh^+ sites by forming much weaker Rh-CO bond strengths, which selectively produced C_2^+ oxygenates (especially ethanol) through an easy formation of CH_x intermediates with successive fast CO insertion rate [150]. On the CNT support, the binary or ternary metal oxides such as CoCe/CNT and CuCoCe/CNT prepared by impregnation method also showed synergy effects on the $Co\text{-}CeO_{2-x}$ interfaces and Cu-Co bimetallic sites for CO hydrogenation to higher alcohols. Those active sites on the CNT improved C-C bond formations by easy CO dissociation, which were mainly originated from superior confinement effects of $Co\text{-}CeO_{2-x}$ interfaces with an enhanced reduction of CoO. In addition, the surface hydroxyl groups on the partially reduced CeO_{2-x} were also responsible for the termination of chain growth reaction by forming alkoxy intermediates to selectively form higher alcohols as well [151]. In addition, the binary metal oxides were synthesized with three-dimensionally ordered macroporous (3DOM) Cu–Fe catalysts through glyoxylate routes. The synergy effects of geometric and electronic interactions of $Cu^0 - \chi\text{-}Fe_5C_2$ with main Hägg-type carbides ($\chi\text{-}Fe_5C_2$) were attributed to the closer d-band center of $Cu^0 - \chi\text{-}Fe_5C_2(510)$ to Fermi level, and more electron-rich interfaces of the $Cu^0 - \chi\text{-}Fe_5C_2(510)$ were originated

from the delocalized electron transfer from Cu^0 atoms as described in Fig. 14D. Therefore, the $Cu^0 - \chi\text{-}Fe_5C_2(510)$ interfaces enhanced CO activation and CO insertion into surface alkyl group to form C_2-oxygenataes, which increased ethanol selectivity and reaction pathway was proposed as $CHCO + (H) \rightarrow CH_2CO + (H) \rightarrow CH_3CO + (H) \rightarrow CH_3CHO + (H) \rightarrow CH_3CH_2O + (H) \rightarrow C_2H_5OH$ on the $Cu^0 - \chi\text{-}Fe_5C_2(510)$ surfaces [152].

Perovskite-like $LaCo_{1-x}Mn_xO_3$ was also proposed for CO hydrogenation, and $LaCo_{0.9}Mn_{0.1}O_3$ catalyst showed a superior alcohols selectivity (C_{2+}–OH selectivity of 67.1%) at comparable CO conversion. Those excellent activity was explained by the formation of Co_2C phases during the reaction, where Mn facilitated to form Co_2C species known as highly active sites for non-dissociated adsorption of CO to selectively form oxygenates. The higher alcohols yield was attributed to dual active sites composed of Co^0-Co_2C, where the increased contents of Co_2C phases were attributed to the partial substitution of Co by Mn atoms [153]. On the other hands, molybdenum sulfide-based catalyst was prepared by precipitation method and modified with potassium by a simple physical mixing of amorphous molybdenum sulfide precursor with K_2CO_3. The prepared M5 catalysts with K/Mo ratio of 0.52 showed an excellent CO conversion, and multilayer structures with well-contacted MoS_2 and $KMoS_2$ phases improved the carbon chain growth probability and C_{3+} alcohols production by CO insertion enhancement under proper reaction conditions, which are illustrated in Fig. 14E [154]. For CO hydrogenation to higher alcohols, various transition metals and noble metals can easily activate CO molecules with non-dissociative adsorption pathway to selectively form higher alcohols, where the active Cu, Rh or Co metal sites can be further modified with other metal oxides promoters including Mn or K species well as KMoS phases having various oxidation states.
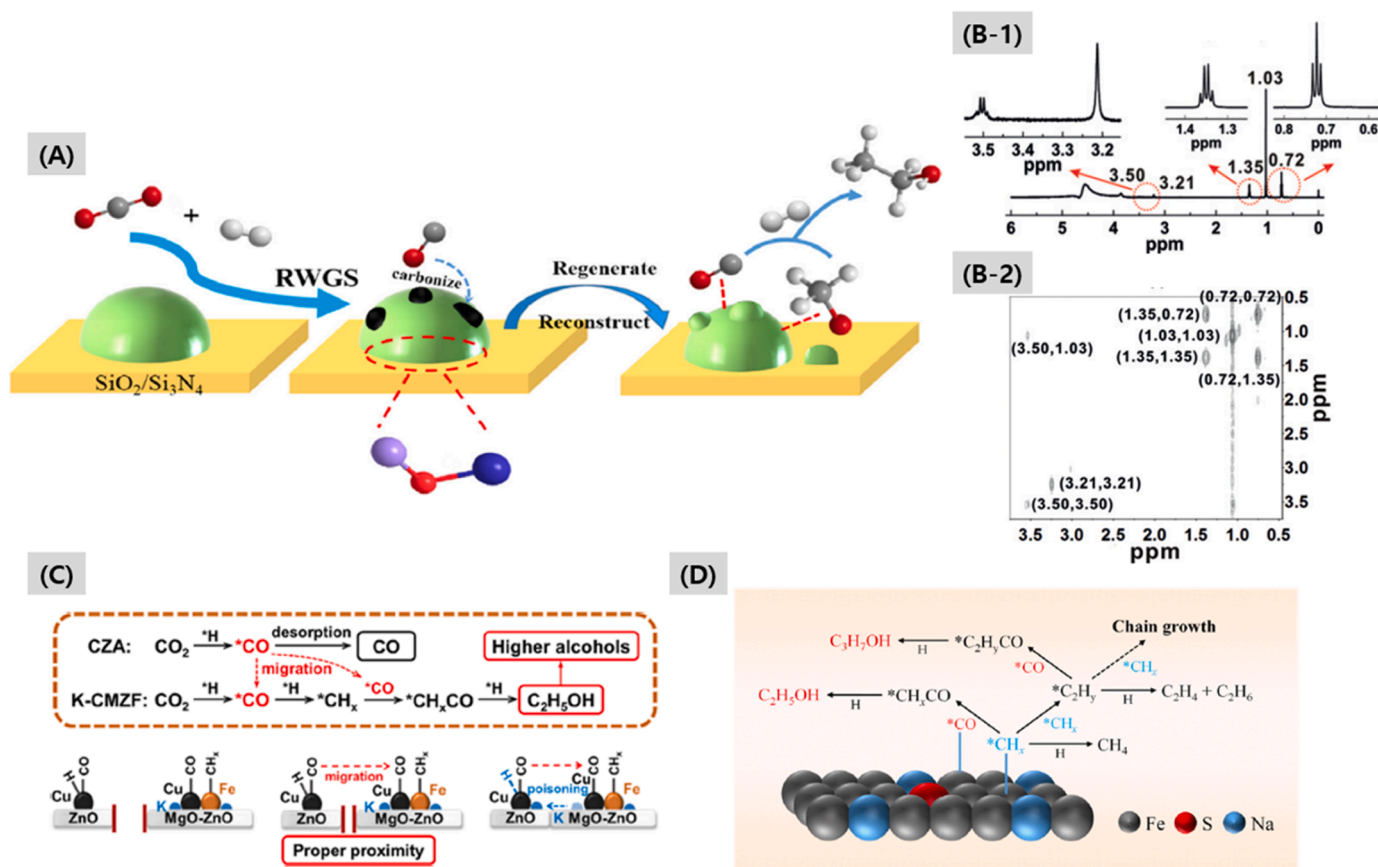

Fig. 15. (A) Schematic diagrams of CO_2 hydrogenation to ethanol on SiO_2/Si_3N_4 surfaces (ref. 155), (B-1) ^{1}H NMR and (B-2) ^{1}H COSY NMR spectra of $CoAlO_x$-600 (ref. 156), (C) Proximity effects of K-CMZF catalyst and reaction mechanisms (ref. 160) and (D) Mechanisms for CO_2 hydrogenation to ethanol on FeNaS catalyst (**ref.** 162).

Direct CO_2 hydrogenation to oxygenates has been also implemented by various catalysts and several Co-based catalysts have been reported. The Co_2C phases were formed on SiO_2 support prepared by an incipient wetness impregnation method, and Na-promoted Co nanoparticles on SiO_2 and Si_3N_4 support showed a superior catalytic durability by selectively forming thermally stable Si-O-Co interactions through strong metal-support interaction (SMSI). As displayed in Fig. 15 A, the Na-Co/SiO_2 and Na-Co/Si_3N_4 preferentially formed the reconstructed Co_2C phases on the metallic Co surfaces, which was responsible for an improved catalytic activity and enhanced reverse water-gas shift (RWGS) reaction activity. Furthermore, the appropriate SMSI effects on the Na-Co/Si_3N_4 and Na-Co/SiO_2 improved the stability of Co_2C phases, which were mainly responsible for higher CO_2 conversion as well as ethanol selectivity and smaller CH_4 formation compared to other supporting materials [155]. The interactions of Na and Co_2C were adjusted by Na content on SiO_2 support, where the Co-impregnated SiO_2 at a fixed 20 wt%Co was prepared by adding it to alkali metal solution (Li, Na or K species) with its different content and 2 wt%Na on the Na-Co/SiO_2 formed the stronger interactions of Na-Co to induce Na-Co_2C active sites for CO_2 hydrogenation. The intensified interactions caused an enhanced Co_2C dispersion and reduction of particle sizes, which increased RWGS rate and space time yield of ethanol. In addition, CO_2 adsorption and non-dissociative adsorption of CO were enhanced on the Na-Co_2C sites due to their enhanced interactions and adjusted surface CO/CHx ratio, where the inappropriate interactions of CO molecules induced easy desorption of CO resulted in increasing CO selectivity [156].

For measuring the different Co phases for CO_2 hydrogenation activity, Co-impregnated Al_2O_3 was prepared by co-precipitation (CoAlOx-T) at different reduction temperature (T, °C). The most appropriate reduction temperature of 600 °C (CoAlO$_x$-600) revealed the best catalytic activity with a higher ethanol selectivity. The superior catalytic activity and stability on the CoAlO$_x$-600 were mainly attributed to optimal surface cobalt phases such as Co-CoO mixtures, which enhanced the formation of active $*CH_x$ intermediates. Based on the results of ^1H NMR and ^1H homonuclear chemical shift correlation (COSY) spectra as shown in Figs. 15B-1 and 15B-2, the $*CH_3$ group and $*CH_2$ intermediates bonded to the oxygens assigned to the chemical shifts of 1.03 and 3.21 ppm were observed on the CoAlO$_x$-600 surfaces. The selective coupling of $*CH_3$ species with $*C_1$-oxygen species was responsible to form C_2-oxygenates rather than its hydrogenation to form CH_4 [157]. In addition, the addition of Ni metal on the CoAlOx by coprecipitation method also improved the catalytic activity, especially on the $Co_{0.52}Ni_{0.48}AlOx$ with ethanol yield of 15.8 mmol/g$_{cat}$ and its selectivity of 85.7%. The Ni metal promoter seems to boost up the formation of stable $*CHx$ intermediates, which can be easily inserted into $*HCOO$ formate intermediates to form C_2-oxygenates instead of selective methanation as well [158]. Therefore, the Co metal can generate its various phases on different supporting materials, which induces different surface properties for direct CO_2 hydrogenation to higher alcohols.

Furthermore, various zeolites can be utilized for CO_2 hydrogenation to produce ethanol, and Cu@Na-Beta was prepared by alkaline treatment of commercial Na-Beta zeolite for the introduction of mesopore structures, which was further treated by Cu impregnation and calcination to prepare CuO/alk-Beta catalyst. The CuO/alk-Beta was added into the typical Na-Beta synthesis gel which was kept under a typical hydrothermal synthesis condition. After the rinsing and calcining the hydrothermally treated catalyst, the final catalyst was obtained and reduced before the reaction (Cu@Na-Beta), which showed a higher single pass ethanol yield with ~14%. The intimate interactions between Cu nanoparticles (2–5 nm in size) and Na-Beta were responsible for the higher CO_2 hydrogenation to ethanol, where CO_2 was hydrogenated to form $CH_3 *$ at the surfaces of Cu nanoparticles and adsorbed $CO_2 *$ was reacted with $CH_3 *$ to form CH_3COO* as the most stable surface intermediate resulted in forming ethanol. The 3D Na-Beta zeolite frameworks also enhanced the effects of confinement and modulation of Cu nanoparticles by restricting byproducts formation [159]. To overcome the

difficult C-C bond formation by suppressing the surface coverages of C_1 species, tandem catalysis was suggested with commercial Cu-Zn-Al_2O_3 (CZA) and K-CMZF (K-CuMgZnFe) mixed metal oxides after powder mixing method. The CZA was responsible for RWGS and K-CMZF was to increase CO insertion rate, which resulted in an increase of CO_2 conversion to higher alcohols. In addition, the proper proximity of two metal oxides catalysts were investigated to ensure two reactions rates and to accelerate the transfer of $*CO$ intermediate formed from CZA to K-CMZF catalyst as illustrated in Fig. 15 C [160].

Novel single atom catalysts (SAC) such as Pd atom-incorporated Fe_3O_4 magnetite (0.1 wt% Pd/Fe_3O_4) have been also attractive for CO_2 hydrogenation to oxygenates, which are stable even at high reaction temperatures. The higher CO_2 conversion and higher ethanol selectivity were observed on the SAC due to its appropriate SMSI effects between single Pd atom sites with Fe_3O_4 by preferentially forming surface architectures for an easy C-C coupling reaction [161]. Another Fe-based catalyst, FeNaS-0.6 prepared by precipitation method with Fe, Na and S precursors was reported. The synergistic effects of Na and S caused superior alcohols selectivity, where Na species boosted CO dissociation and S species (sulfate) helped to provide more Fe sites for non-dissociative CO adsorption. Therefore, Na and S modification on the Fe-based catalyst was found to be efficient by reducing energy barriers for intermediates formation. In more details, the electron-withdrawing effects of sulfate enabled to adjust the surrounding Fe sites for preferential CO dissociation to the proper sites for non-dissociative CO adsorption, which seem to be crucial step for the selective production of higher alcohols as displayed in Fig. 15D [162]. For the production of higher alcohols by CO_2 hydrogenation, catalytic activity and stability were closely related with strong metal-support interactions, which adjusted the distributions of active metal sites and its phases, and the selection of alkali metal promotors was found to be important to optimize electron-rich environments of the active metal sites to enhance the stability of surface intermediates (for example, formyl or formate species) to oxygenates formed from the dissociatively adsorbed CO_2 molecules on the various hybridized catalysts such as Co, Cu or Fe-based catalysts with various zeolites [155–162].

In summary, the Fe and Co-based catalysts have been largely applied for CO/CO_2 conversion to higher alcohols including ethanol product as well, where the Fe and Co phases were found to be important factors to change product distributions through different reaction mechanisms. Especially, the additions of alkali metals and adjustments of metal-support interactions also affected the catalytic activity and selectivity to desirable products. For example, CO can be converted into hydrocarbons via FTS reaction on the Fe- and Co-based catalysts with various promoters such as alkaline or transition metals, where their phases and sizes are crucial to change WGS-RWGS activity. In addition, the modified-FTS catalysts can also enhance CO_2 conversion into hydrocarbons or aromatics, which can be followed by two routes such as (1) RWGS + FTS route and (2) CO_2 hydrogenation + MTH route. In general, the Fe-based catalysts including FeCo alloy and In_2O_3-based catalysts can be hybridized with ZSM-5 for CO_2 hydrogenation + MTH route. Higher alcohols can be also synthesized by using Co- and Mo-based catalysts, and various active sites such as carbide phases were suggested to maximize the selectivity toward desirable alcohols by adjusting surface properties.

4. Concluding remarks and perspectives

In the present review paper, the recent trends for CO/CO_2 conversions to ethanol, higher hydrocarbons and higher alcohols are summarized to give insight about catalyst preparation strategy with their reactor conditions. Various strategies to develop supports, to modulate active sites and to reveal the effects of promoters have been summarized, and some tandem catalysis has been largely reported to control product distributions or direct conversion of CO_2 to value-added chemicals, where the tandem catalysis is implemented by using two or three

different catalysts with their different proximity of each catalyst beds. Therefore, it is still important to design novel catalysts for each single reaction and proper reaction conditions and catalyst configurations should be optimized to enhance the desired products selectivity. For example, the surface properties of active metal oxides can be adjusted in terms of their crystallite sizes, oxidation states or sintering resistances and oxygen vacant sites. The acidic sites (Brønsted or Lewis acid sites) of zeolites can be modulated during the preparation step with various alkaline and transition metals promoters, where the surface acidic strengths and site distributions alter the catalytic activity, product distribution and extent of coke deposition significantly. The active site confirmations are generally conducted by XRD, TEM or XPS/AES analysis, and the oxidation states and oxygen vacant sites of metal oxides can be quantified by AES and XPS analysis to distinguish different Cu species such as Cu^{2+}, Cu^{+} and Cu^{0} on Cu-based catalysts. In addition, EXAFS, 2D NMR and Mössbauer spectroscopy are also important to disclose catalyst compositions and structures of active sites. The acidic sites are measured by NH_3-TPD and FT-IR analysis with probe molecules, and FT-IR analysis with pyridine probe molecules can quantify the acidic sites in the 10-MR or 12-MR channels on the zeolites and bulk basic molecules can be also utilized for the titration of external acidic sites, which are important for aromatization or higher hydrocarbon formation and DME carbonylation. In addition, the cokes on the used catalysts can be analyzed by TGA to quantify the amount of deposited coke precursors. Some in-situ analysis techniques with DRIFT or mass spectroscopy are used to prove reaction mechanisms with the help of DFT calculation. The tandemly coupled CO_x conversions to value-added chemicals seem to be excellent to maximize the selectivity towards target products. In case of those tandem catalytic reactions, proximity effects of the hybridized catalysts should be considered properly to adjust their surface properties during hybridization of two or three different active sites for developing various efficient CO_x conversions through proper selections of catalyst configurations and reaction conditions.

In addition, oxygenates formations by CO or CO_2 hydrogenation can be carried out via the indirect ethanol production process over various active metals, which can be embedded in various metal oxides or zeolites for the syngas conversion to methanol and DME followed by DME carbonylation steps over various zeolites and successive hydrogenation of methyl acetate to ethanol. For a gas-phase DME carbonylation, various zeolites containing 8-MR channels have been widely applied after various zeolite modification methods such as precise metal ion exchanges, alkali treatments or morphology designs and so on. Through various hydrogenation reactions of MA, DMO and AA on the Cu-based catalysts with various promoters, conversions and selectivity to desired products are largely changed due to their different metal-support interactions and phases of active sites. CO_2 hydrogenation, first step for indirect ethanol synthesis, has been vigorously investigated by using conventional typical Cu-based catalysts. Although there are several commercialized Cu-based catalysts for methanol synthesis by CO_2 hydrogenation, the Cu phases are generally vulnerable at high reaction temperatures. Aside from the Cu-based catalysts, the Zn, Zr and In metal oxides have been reported as promising catalysts for CO_2 activation where the formation of oxygen vacant sites can be regarded as active sites. The newly developed metal oxides are generally stable at higher reaction temperatures than the Cu-based catalysts with the suppressed RWGS activity, where the oxygen vacant sites on the Zn, Zr and In oxide can also enhance the electron transfer ability. Recently, the effects of In or Zn-Zr metal oxides were unraveled with the contributions of metal oxides promoters to enhance sintering-resistance properties with a higher methanol selectivity owing to the suppressed WGS-RWGS reaction activity.

For the STD reaction on the hybrid catalysts, Cu-based catalysts are generally hybridized with solid acid catalysts such as alumina or zeolites with two active sites where the Cu-based catalysts are upgraded by adding promoters to adjust the surface Cu natures and to suppress WGS-RWGS reaction activity with an enhanced surface hydrophobicity of

solid acid catalysts with their different morphology. The bifunctional hybrid catalysts can be also optimized by controlling the weight ratio of both metal-based and solid acid catalysts and its catalyst loading configurations such as physical mixing or co-precipitation. The roles of Cu^{+} phases under reductive condition were highlighted in terms of an enhanced CO_2 conversion and surface acidity of solid acid oxides were also found to be important for methanol dehydration, which were largely improved on the In, Zr or Zn (mixed) metal oxides (larger oxygen vacant sites) for CO_2 hydrogenation combined with zeolites for STD reaction. To suppress undesired side reactions during STD reaction, the catalysts with more hydrophobic surfaces were found to be more efficient by decreasing RWGS reaction activity.

DME carbonylation seems to be a bottleneck of indirect ethanol production process through CO_2 hydrogenation, where the reaction is more favorable on Brønsted acid sites in the 8-MR channels of zeolites and other defective sites are active for coke depositions, and MOR zeolites have been intensively developed after modification with various methods. One efficient proposed method to enhance the stability is to adopt basic pyridine treatment to block external acidic sites selectively. Another zeolite frameworks containing 8-MR channels are also applied and in case of the FER zeolite, the crystallinity and Al distributions are important for a long-term catalytic stability, and new zeolite frameworks containing desirable BAS in the 8-MR channels are still required to enhance the stability. In addition, the catalyst deactivation caused by coke depositions was effectively decreased by using pyridine-modified MOR zeolite with abundant acidic sites in the 8-MR channels during DME carbonylation reaction. Ethanol can be also synthesized via hydrogenation of different C_2 chemicals (MA/DMO/AA). In case of MA, Cu-based catalysts are dominantly used where the Cu^{+} phases are known as active sites. For DMO and AA hydrogenation, various catalysts such as Mo_2C, Fe and Re-based catalysts are known for effective DMO activation and Cu, Pt and Rh-based catalyst are also known for AA hydrogenation. The MA/DMO/AA hydrogenation reactions showed an extremely high conversion and ethanol selectivity, which are also important for tandem catalytic reactions.

In addition, direct ethanol synthesis methods from syngas conversions have been reported through the combinations of two or three catalytic reactions such as representative three routes of (1) syngas → DME → MA → ethanol, (2) DME/syngas → MA → ethanol and (3) syngas → methanol/AA → ethanol. For those stepwise tandem reactions, the catalyst loading configurations are crucial with proper selections of catalysts, where the proximity between the catalyst-layers and reaction conditions largely altered product distributions due to different diffusion rates of intermediates on various active sites. The well-organized tandem reactions are beneficial to overcome thermodynamic limitations by increasing the selectivity toward desirable products, however, not only properties of catalysts but also reactor configurations should be properly considered and optimized. For these tandemly coupled catalytic reaction, the effects of catalyst proximity with different contact modes should be clearly disclosed which can significantly change catalytic activity and stability by coke depositions.

In addition, CO and CO_2 could be directly converted into higher hydrocarbons and higher alcohols by using Fe or Co-based active metals with promoters on various supports such as zeolite, metal oxides or carbon-based materials through FTS and modified-FTS reaction. For both direct CO_x conversion, selectivity controls are main issues because lots of byproducts and undesirable chemicals can be formed simultaneously. By regulating strong metal-support interactions, phases of active metals and physicochemical properties of supporting materials were largely adjusted through effective synthetic methods and promoter which altered the product distributions including fuel-grade hydrocarbons and oxygenates including ethanol. Generally, hydrocarbons distributions can be controlled by modification of those catalysts. The active sites are modulated by adding alkali or transition metal promoters such as K, Na, Cu, Mn and so on as well as applications of metal carbide phases. In addition, the morphologies of supports are important to adjust

overall properties of active metal sites, for example, MOF or graphene-derived supports can be utilized to form useful carbon-based FTS catalysts. The FTS reaction can be further developed by regulating active metals for direct CO_2 hydrogenation.

In case of the modified-FTS reaction route, tandemly coupled reactions involving RWGS followed by FTS and CO_2 hydrogenation followed by MTH reaction have been investigated to develop most efficient catalytic systems to meet carbon net zero emission as well. The catalysts can be also modified with various promoters to adjust C_{5+} selectivity by controlling RWGS activity. The combination of Fe-based catalysts with HZSM-5 zeolite is also active for CO_2 conversion to CO by RWGS reaction followed by the FTS and successive oligomerization-isomerization reaction on the ZSM-5 to form various heavier isomers as well. Therefore, it is important to develop novel and active Fe-based catalysts and stable ZSM-5 with tandem reaction schemes. The C_{5+} hydrocarbons production can be also implemented by the combinations of CO_2 hydrogenation to methanol followed by MTH reaction by using In-Zr mixed metal oxides, where the oxygen vacant sites, properties of zeolite and their proximity are crucial to alter product distributions simultaneously. Those reaction routes can be also applied for CO_2 conversion to BTX with similar approaches through tandem reactions, and the catalyst-bed configurations are known to be important for stepwise direct ethanol synthesis. Furthermore, various zeolite modification techniques are applied for optimizing product distributions and enhancing stability through adjusting external acidic sites and other zeolite frameworks having different acidic site distribution and topologies seems to be important for sequential oligomerization-isomerization-aromatization reaction. In addition, Co, Mo, Cu and Fe are also known as active metals for CO_x conversions to higher alcohols, which can be modified with various promoters. On the various alkali metal promoters-modified supports including metal oxides, graphene and MOFs revealed different SMSI effects and surface oxygen vacant sites are also critical for changing the distributions of oxygenates. The direct CO_2 utilization for higher alcohols production can be also achieved by the strategies for tandem reactions by using proper catalyst-layers configurations. In case of modified-FTS reaction route, the phases of active sites should be confirmed for CO_2 hydrogenation, and acidic properties of zeolite should be also ascertained. The most effective configurations of two catalyst layers are also required to be confirmed to enlarge catalytic activity and stability for the tandemly coupled CO_2 conversions to various value-added chemical products with smaller byproducts.

Declaration of Competing Interest

The authors declare that they have no known competing financial interests or personal relationships that could have appeared to influence the work reported in this paper.

Data Availability

Data will be made available on request.

Acknowledgements

Appendix A. Supporting information

Supplementary data associated with this article can be found in the online version at doi:10.1016/j.apcatb.2023.123477.

References

[1] R. Meys, A. Kätelhön, M. Bachmann, B. Winter, C. Zibunas, S. Suh, A. Bardow, Achieving net-zero greenhouse gas emission plastics by a circular carbon economy, Science 374 (2021) 71–76.

[2] L. Xie, J. Liang, C. Priest, T. Wang, D. Ding, G. Wu, Q. Li, Engineering the atomic arrangement of bimetallic catalysts for electrochemical CO_2 reduction, Chem. Commun. 57 (2021) 1839–1854.

[3] X. Wu, J. Lang, Z. Sun, F. Jin, Y.H. Hu, Photocatalytic conversion of carbon monoxide: from pollutant removal to fuel production, Appl. Catal. B 295 (2021), 120312.

[4] B. Mao, J.-S. Wei, M. Shi, Recent advancements in visible-light-driven carboxylation with carbon dioxide, Chem. Commun. 58 (2022) 9312–9327.

[5] A.R. Woldu, Z. Huang, P. Zhao, L. Hu, D. Astruc, Electrochemical CO_2 reduction (CO_2RR) to multi-carbon products over copper-based catalysts, Coord. Chem. Rev. 454 (2022), 214340.

[6] R.I. Masel, Z. Liu, H. Yang, J.J. Kaczur, D. Carrillo, S. Ren, D. Salvatore, C. P. Berlinguette, An industrial perspective on catalysts for low-temperature CO_2 electrolysis, Nat. Nanotechnol. 16 (2021) 118–128.

[7] M.K. Debe, Electrocatalyst approaches and challenges for automotive fuel cells, Nature 486 (2012) 43–51.

[8] S. Anwar, F. Khan, Y. Zhang, A. Djire, Recent development in electrocatalysts for hydrogen production through water electrolysis, Int. J. Hydrog. Energy 46 (2021) 32284–32317.

[9] X. She, Y. Wang, H. Xu, S. Chi Edman Tsang, S. Ping Lau, Challenges and opportunities in electrocatalytic CO_2 reduction to chemicals and fuels, Angew. Chem. Int. Ed. 61 (2022), e202211396.

[10] K. Villa, J.R. Galán-Mascarós, N. López, E. Palomares, Photocatalytic water splitting: advantages and challenges, Sustain. Energy Fuels 5 (2021) 4560–4569.

[11] X. Tao, Y. Zhao, S. Wang, C. Li, R. Li, Recent advances and perspectives for solar-driven water splitting using particulate photocatalysts, Chem. Soc. Rev. 51 (2022) 3561–3608.

[12] W.-H. Chen, C.-Y. Chen, Water gas shift reaction for hydrogen production and carbon dioxide capture: a review, Appl. Energy 258 (2020), 114078.

[13] M. Rahmati, M.-S. Safdari, T.H. Fletcher, M.D. Argyle, C.H. Bartholomew, Chemical and thermal sintering of supported metals with emphasis on cobalt catalysts during Fischer–Tropsch synthesis, Chem. Rev. 120 (2020) 4455–4533.

[14] D.B. Pal, R. Chand, S.N. Upadhyay, P.K. Mishra, Performance of water gas shift reaction catalysts: a review, Renew. Sustain. Energy Rev. 93 (2018) 549–565.

[15] S.M. Safieddin Ardebili, H. Solmaz, D. İpci, A. Calam, M. Mostafaei, A review on higher alcohol of fusel oil as a renewable fuel for internal combustion engines: applications, challenges, and global potential, Fuel 279 (2020) 118516.

[16] Z. Ma, M.D. Porosoff, Development of tandem catalysts for CO_2 hydrogenation to olefins, ACS Catal. 9 (2019) 2639–2656.

[17] A.M. Bahmanpour, M. Signorile, O. Kröcher, Recent progress in syngas production via catalytic CO_2 hydrogenation reaction, Appl. Catal. B 295 (2021), 120319.

[18] J. Wei, R. Yao, R. Han, Q. Ge, J. Sun, Towards the development of the emerging process of CO_2 heterogenous hydrogenation into high-value unsaturated heavy hydrocarbons, Chem. Soc. Rev. 50 (2021) 10764–10805.

[19] T.A. Atsbha, T. Yoon, P. Seongho, C.J. Lee, A review on the catalytic conversion of CO_2 using H_2 for synthesis of CO, methanol, and hydrocarbons, J. CO_2 Util. 44 (2021), 101413.

[20] A.D. Chowdhury, A.L. Paioni, K. Houben, G.T. Whiting, M. Baldus, B. M. Weckhuysen, Bridging the gap between the direct and hydrocarbon pool mechanisms of the methanol-to-hydrocarbons process, Angew. Chem. Int. Ed. 57 (2018) 8095–8099.

[21] R.P. Ye, J. Ding, W. Gong, M.D. Argyle, Q. Zhong, Y. Wang, C.K. Russell, Z. Xu, A. G. Russell, Q. Li, M. Fan, Y.G. Yao, CO_2 hydrogenation to high-value products via heterogeneous catalysis, Nat. Commun. 10 (2019) 5698.

[22] G. Liu, G. Yang, X. Peng, J. Wu, N. Tsubaki, Recent advances in the routes and catalysts for ethanol synthesis from syngas, Chem. Soc. Rev. 51 (2022) 5606–5659.

[23] R.K. Parsapur, S. Chatterjee, K.-W. Huang, The insignificant role of dry reforming of methane in CO_2 emission relief, ACS Energy Lett. 5 (2020) 2881–2885.

[24] K.A. Ali, A.Z. Abdullah, A.R. Mohamed, Recent development in catalytic technologies for methanol synthesis from renewable sources: a critical review, Renew. Sustain. Energy Rev. 44 (2015) 508–518.

[25] S.T. Bai, G. De Smet, Y. Liao, R. Sun, C. Zhou, M. Beller, B.U.W. Maes, B.F. Sels, Homogeneous and heterogeneous catalysts for hydrogenation of CO_2 to methanol under mild conditions, Chem. Soc. Rev. 50 (2021) 4259–4298.

[26] U. Mondal, G.D. Yadav, Perspective of dimethyl ether as fuel: Part I. Catalysis, J. CO_2 Util. 32 (2019) 299–320.

[27] U. Mondal, G.D. Yadav, Perspective of dimethyl ether as fuel: Part II- analysis of reactor systems and industrial processes, J. CO_2 Util. 32 (2019) 321–338.

[28] K. Saravanan, H. Ham, N. Tsubaki, J.W. Bae, Recent progress for direct synthesis of dimethyl ether from syngas on the heterogeneous bifunctional hybrid catalysts, Appl. Catal. B 217 (2017) 494–522.

[29] E. Zhan, Z. Xiong, W. Shen, Dimethyl ether carbonylation over zeolites, J. Energy Chem. 36 (2019) 51–63.

[30] S.S. Ali, S.S. Ali, N. Tabassum, A review on CO_2 hydrogenation to ethanol: Reaction mechanism and experimental studies, J. Environ. Chem. Eng. 10 (2022), 106962.

[31] F. Zeng, C. Mebrahtu, X. Xi, L. Liao, J. Ren, J. Xie, H.J. Heeres, R. Palkovits, Catalysts design for higher alcohols synthesis by CO$_2$ hydrogenation: Trends and future perspectives, Appl. Catal. B 291 (2021), 120073.

[32] W.U. Khan, L. Baharudin, J. Choi, A.C.K. Yip, Recent progress in CO hydrogenation over bimetallic catalysts for higher alcohol synthesis, ChemCatChem 13 (2021) 111–120.

[33] D. Xu, Y. Wang, M. Ding, X. Hong, G. Liu, S.C.E. Tsang, Advances in higher alcohol synthesis from CO$_2$ hydrogenation, Chem 7 (2021) 849–881.

[34] A.C. Ghogia, A. Nzihou, P. Serp, K. Soulantica, D. Pham Minh, Cobalt catalysts on carbon-based materials for Fischer-Tropsch synthesis: a review, Appl. Catal. A 609 (2021), 117906.

[35] C. Du, P. Lu, N. Tsubaki, Efficient and new production methods of chemicals and liquid fuels by carbon monoxide hydrogenation, ACS Omega 5 (2020) 49–56.

[36] P. Gao, L. Zhang, S. Li, Z. Zhou, Y. Sun, Novel heterogeneous catalysts for CO$_2$ hydrogenation to liquid fuels, ACS Cent. Sci. 6 (2020) 1657–1670.

[37] S. Kar, A. Goeppert, G.K.S. Prakash, Catalytic homogeneous hydrogenation of CO to methanol via formamide, J. Am. Chem. Soc. 141 (2019) 12518–12521.

[38] P. Lu, J. Sun, D. Shen, R. Yang, C. Xing, C. Lu, N. Tsubaki, S. Shan, Direct syngas conversion to liquefied petroleum gas: Importance of a multifunctional metal-zeolite interface, Appl. Energy 209 (2018) 1–7.

[39] P. Gao, L. Zhong, B. Han, M. He, Y. Sun, Green carbon science: keeping the pace in practice, Angew. Chem. Int. Ed. 61 (2022), e202210095.

[40] Z. Zhou, P. Gao, Direct carbon dioxide hydrogenation to produce bulk chemicals and liquid fuels via heterogeneous catalysis, Chin. J. Catal. 43 (2022) 2045–2056.

[41] J. Zhong, X. Yang, Z. Wu, B. Liang, Y. Huang, T. Zhang, State of the art and perspectives in heterogeneous catalysis of CO$_2$ hydrogenation to methanol, Chem. Soc. Rev. 49 (2020) 1385–1413.

[42] F. Sha, Z. Han, S. Tang, J. Wang, C. Li, Hydrogenation of carbon dioxide to methanol over non−Cu-based heterogeneous catalysts, ChemSusChem 13 (2020) 6160–6181.

[43] J. Wang, G. Li, Z. Li, C. Tang, Z. Feng, H. An, H. Liu, T. Liu, C. Li, A highly selective and stable ZnO-ZrO$_2$ solid solution catalyst for CO$_2$ hydrogenation to methanol, Sci. Adv. 3 (2017), e1701290.

[44] J. Wang, C. Tang, G. Li, Z. Han, Z. Li, H. Liu, F. Cheng, C. Li, High-Performance M$_a$ZrO$_x$ (Ma = Cd, Ga) Solid-Solution Catalysts for CO$_2$ hydrogenation to methanol, ACS Catal. 9 (2019) 10253–10259.

[45] O. Martin, A.J. Martín, C. Mondelli, S. Mitchell, T.F. Segawa, R. Hauert, C. Drouilly, D. Curulla-Ferré, J. Pérez-Ramírez, Indium oxide as a superior catalyst for methanol synthesis by CO$_2$ hydrogenation, Angew. Chem. Int. Ed. 55 (2016) 6261–6265.

[46] S. Dang, B. Qin, Y. Yang, H. Wang, J. Cai, Y. Han, S. Li, P. Gao, Y. Sun, Rationally designed indium oxide catalysts for CO$_2$ hydrogenation to methanol with high activity and selectivity, Sci. Adv. 6 (2020), eaaz2060.

[47] M.S. Frei, C. Mondelli, A. Cesarini, F. Krumeich, R. Hauert, J.A. Stewart, D. Curulla Ferré, J. Pérez-Ramírez, Role of zirconia in indium oxide-catalyzed CO$_2$ hydrogenation to methanol, ACS Catal. 10 (2020) 1133–1145.

[48] H. Ham, S.W. Baek, C.H. Shin, J.W. Bae, Roles of structural promoters for direct CO$_2$ hydrogenation to dimethyl ether over ordered mesoporous bifunctional Cu/M-Al$_2$O$_3$ (M = Ga or Zn), ACS Catal. 9 (2019) 679–690.

[49] S. Asthana, C. Samanta, A. Bhaumik, B. Banerjee, R.K. Voolapalli, B. Saha, Direct synthesis of dimethyl ether from syngas over Cu-based catalysts: Enhanced selectivity in the presence of MgO, J. Catal. 334 (2016) 89–101.

[50] L. Zhang, Z. Bian, K. Sun, W. Huang, Effects of Sn on the catalytic performance for one step syngas to DME in slurry reactor, N. J. Chem. 45 (2021) 3783–3789.

[51] L. Liu, Z. Lin, S. Lin, Y. Chen, L. Zhang, S. Chen, X. Zhang, J. Lin, Z. Zhang, S. Wan, Y. Wang, Conversion of syngas to methanol and DME on highly selective Pd/ZnAl$_2$O$_4$ catalyst, J. Energy Chem. 58 (2021) 564–572.

[52] F. Frusteri, M. Migliori, C. Cannilla, L. Frusteri, E. Catizzone, A. Aloise, G. Giordano, G. Bonura, Direct CO$_2$-to-DME hydrogenation reaction: New evidences of a superior behaviour of FER-based hybrid systems to obtain high DME yield, J. CO$_2$ Util. 18 (2017) 353–361.

[53] G. Bonura, C. Cannilla, L. Frusteri, A. Mezzapica, F. Frusteri, DME production by CO$_2$ hydrogenation: Key factors affecting the behaviour of CuZnZr/ferrierite catalysts, Catal. Today 281 (2017) 337–344.

[54] H.S. Jung, F. Zafar, X. Wang, T.X. Nguyen, C.H. Hong, Y.G. Hur, J.W. Choung, M.-J. Park, J.W. Bae, Morphology effects of Ferrierite on bifunctional Cu-ZnO-Al$_2$O$_3$/Ferrierite for direct syngas conversion to dimethyl ether, ACS Catal. 11 (2021) 14210–14223.

[55] D.B. Rasmussen, J.M. Christensen, B. Temel, F. Studt, P.G. Moses, J. Rossmeisl, A. Riisager, A.D. Jensen, Ketene as a reaction intermediate in the carbonylation of dimethyl ether to methyl acetate over Mordenite, Angew. Chem. Int. Ed. 54 (2015) 7261–7264.

[56] X. Wang, R. Li, C. Yu, Y. Liu, L. Liu, C. Xu, H. Zhou, C. Lu, Influence of acid site distribution on dimethyl ether carbonylation over Mordenite, Ind. Eng. Chem. Res. 58 (2019) 18065–18072.

[57] K. Cai, S. Huang, Y. Li, Z. Cheng, J. Lv, X. Ma, Influence of acid strength on the reactivity of dimethyl ether carbonylation over H-MOR, ACS Sustain. Chem. Eng. 7 (2019) 2027–2034.

[58] J. Yao, X. Feng, J. Fan, Y. He, R. Kosol, Y. Zeng, G. Liu, Q. Ma, G. Yang, N. Tsubaki, Effects of mordenite zeolite catalyst synthesis conditions on dimethyl ether carbonylation, Micro Mesopor. Mater. 306 (2020), 110431.

[59] X. Wang, R. Li, C. Yu, Y. Liu, L. Zhang, C. Xu, H. Zhou, Enhancing the dimethyl ether carbonylation performance over mordenite catalysts by simple alkaline treatment, Fuel 239 (2019) 794–803.

[60] S. Liu, H. Liu, X. Ma, Y. Liu, W. Zhu, Z. Liu, Identifying and controlling the acid site distributions in mordenite zeolite for dimethyl ether carbonylation reaction by means of selective ion-exchange, Catal. Sci. Technol. 10 (2020) 4663–4672.

[61] A.A.C. Reule, N. Semagina, Zinc hinders deactivation of copper-Mordenite: Dimethyl ether carbonylation, ACS Catal. 6 (2016) 4972–4975.

[62] Y. Li, S. Huang, Z. Cheng, K. Cai, L. Li, E. Milan, J. Lv, Y. Wang, Q. Sun, X. Ma, Promoting the activity of Ce-incorporated MOR in dimethyl ether carbonylation through tailoring the distribution of Brønsted acids, Appl. Catal. B 256 (2019), 117777.

[63] X. Wang, R. Li, C. Yu, L. Zhang, C. Xu, H. Zhou, Dimethyl ether carbonylation over nanosheet-assembled hierarchical mordenite, Micro Mesopor. Mater. 274 (2019) 227–235.

[64] P. He, Y. Li, K. Cai, X. Xiong, J. Lv, Y. Wang, S. Huang, X. Ma, Nano-assembled Mordenite zeolite with tunable morphology for carbonylation of dimethyl ether, ACS Appl. Nano Mater. 3 (2020) 6460–6468.

[65] L. Li, Q. Wang, H. Liu, T. Sun, D. Fan, M. Yang, P. Tian, Z. Liu, Preparation of spherical Mordenite zeolite assemblies with excellent catalytic performance for dimethyl ether carbonylation, ACS Appl. Mater. Inter. 10 (2018) 32239–32246.

[66] K. Cao, D. Fan, L. Li, B. Fan, L. Wang, D. Zhu, Q. Wang, P. Tian, Z. Liu, Insights into the Pyridine-Modified MOR Zeolite Catalysts for DME Carbonylation, ACS Catal. 10 (2020) 3372–3380.

[67] Y. Li, Q. Sun, S. Huang, Z. Cheng, K. Cai, J. Lv, X. Ma, Dimethyl ether carbonylation over pyridine-modified MOR: Enhanced stability influenced by acidity, Catal. Today 311 (2018) 81–88.

[68] J. Kim, H. Ham, H.S. Jung, Y. Wang, Y. He, N. Tsubaki, S.J. Cho, G.Y. Han, J.W. Bae, Dimethyl ether carbonylation to methyl acetate over highly crystalline zeolite seed-derived ferrierite, Catal. Sci. Technol. 8 (2018) 3060–3072.

[69] H. Ham, H.S. Jung, H.S. Kim, J. Kim, S.J. Cho, W.B. Lee, M.-J. Park, J.W. Bae, Gas-phase carbonylation of dimethyl ether on the stable seed-derived Ferrierite, ACS Catal. 10 (2020) 5135–5146.

[70] H.S. Jung, N.T. Xuan, J.W. Bae, Carbonylation of dimethyl ether on ferrierite zeolite: Effects of crystallinity to coke distribution and deactivation, Micro Mesopor. Mater. 310 (2021), 110669.

[71] X. Feng, J. Yao, H. Li, Y. Fang, Y. Yoneyama, G. Yang, N. Tsubaki, A brand new zeolite catalyst for carbonylation reaction, Chem. Commun. 55 (2019) 1048–1051.

[72] M. Lusardi, T.T. Chen, M. Kale, J.H. Kang, M. Neurock, M.E. Davis, Carbonylation of dimethyl ether to methyl acetate over SSZ-13, ACS Catal. 10 (2020) 842–851.

[73] Z. Xiong, E. Zhan, M. Li, W. Shen, DME carbonylation over a HSUZ-4 zeolite, Chem. Commun. 56 (2020) 3401–3404.

[74] J. Yao, Q. Wu, J. Fan, S. Komiyama, X. Yong, W. Zhang, T. Zhao, Z. Guo, G. Yang, N. Tsubaki, A carbonylation zeolite with specific nanosheet structure for efficient catalysis, ACS Nano 15 (2021) 13568–13578.

[75] H. Shen, Y. Li, S. Huang, K. Cai, Z. Cheng, J. Lv, X. Ma, The carbonylation of dimethyl ether catalyzed by supported heteropoly acids: The role of Brønsted acid properties, Catal. Today 330 (2019) 117–123.

[76] Y. Wang, Y. Zhao, J. Lv, X. Ma, Facile Synthesis of Cu@CeO$_2$ and its catalytic behavior for the hydrogenation of methyl acetate to ethanol, ChemCatChem 9 (2017) 2085–2090.

[77] X. Huang, M. Ma, S. Miao, Y. Zheng, M. Chen, W. Shen, Hydrogenation of methyl acetate to ethanol over a highly stable Cu/SiO$_2$ catalyst: Reaction mechanism and structural evolution, Appl. Catal. A 531 (2017) 79–88.

[78] Y. Zhao, B. Shan, Y. Wang, J. Zhou, S. Wang, X. Ma, An Effective CuZn-SiO$_2$ bimetallic catalyst prepared by hydrolysis precipitation method for the hydrogenation of methyl acetate to ethanol, Ind. Eng. Chem. Res. 57 (2018) 4526–4534.

[79] Y. Liu, J. Ding, J. Sun, J. Zhang, J. Bi, K. Liu, F. Kong, H. Xiao, Y. Sun, J. Chen, Molybdenum carbide as an efficient catalyst for low-temperature hydrogenation of dimethyl oxalate, Chem. Commun. 52 (2016) 5030–5032.

[80] Y. Liu, J. Ding, J. Bi, Y. Sun, J. Zhang, K. Liu, F. Kong, H. Xiao, J. Chen, Effect of Cu-doping on the structure and performance of molybdenum carbide catalyst for low-temperature hydrogenation of dimethyl oxalate to ethanol, Appl. Catal. A 529 (2017) 143–155.

[81] J. Zhu, G. Zhao, W. Sun, Q. Nie, S. Wang, Q. Xue, Y. Liu, Y. Lu, Superior FeNi$_3$-FeO$_x$/Ni-foam catalyst for gas-phase hydrogenation of dimethyl oxalate to ethanol, Appl. Catal. B 270 (2020), 118873.

[82] Y. Sun, Q. Ma, Q. Ge, J. Sun, Tunable synthesis of ethanol or methyl acetate via dimethyl oxalate hydrogenation on confined iron catalysts, ACS Catal. 11 (2021) 4908–4919.

[83] Z. Du, M. Chen, X. Wang, X. Chen, X. Mou, Y. Tan, W. Yang, C. Huang, H. Zhu, R. Lin, Y. Ding, Bifunctional rhenium–copper nanostructures for intensified and stable ethanol synthesis via hydrogenation of dimethyl oxalate, Catal. Sci. Technol. 10 (2020) 3175–3180.

[84] J. Shi, J. He, K. Ma, S. Tang, C. Liu, H. Yue, B. Liang, Cu active sites confined in MgAl layered double hydroxide for hydrogenation of dimethyl oxalate to ethanol, Catal. Today 365 (2021) 318–326.

[85] X. Dong, J. Lei, Y. Chen, H. Jiang, M. Zhang, Selective hydrogenation of acetic acid to ethanol on Cu-In catalyst supported by SBA-15, Appl. Catal. B 244 (2019) 448–458.

[86] G. Xu, J. Zhang, S. Wang, Y. Zhao, X. Ma, A well fabricated PtSn/SiO$_2$ catalyst with enhanced synergy between Pt and Sn for acetic acid hydrogenation to ethanol, RSC Adv. 6 (2016) 51005–51013.

[87] M. Zhou, H. Zhang, H. Ma, W. Ying, Insight on mechanism of Sn modification in alumina supported RhSn catalysts for acetic acid hydrogenation to fuel-grade ethanol, Fuel 203 (2017) 774–780.

[88] S. Yoshimaru, M. Sadakiyo, N. Maeda, M. Yamauchi, K. Kato, J. Pirillo, Y. Hijikata, Support Effect of metal-organic frameworks on ethanol production through acetic acid hydrogenation, ACS Appl. Mater. Inter. 13 (2021) 19992–20001.

[89] W. Zhou, J. Kang, K. Cheng, S. He, J. Shi, C. Zhou, Q. Zhang, J. Chen, L. Peng, M. Chen, Y. Wang, Direct conversion of syngas into methyl acetate, ethanol, and ethylene by relay catalysis via the intermediate dimethyl ether, Angew. Chem. Int. Ed. 57 (2018) 12012–12016.

[90] Z. Cao, T. Hu, J. Guo, J. Xie, N. Zhang, J. Zheng, L. Che, B.H. Chen, Stable and facile ethanol synthesis from syngas in one reactor by tandem combination CuZnAl-HZSM-5, modified-H-Mordenite with CuZnAl catalyst, Fuel 254 (2019), 115542.

[91] X. Feng, J. Yao, Y. Zeng, Y. Cui, S. Kazumi, R. Prasert, G. Liu, J. Wu, G. Yang, N. Tsubaki, More efficient ethanol synthesis from dimethyl ether and syngas over the combined nano-sized ZSM-35 zeolite with CuZnAl catalyst, Catal. Today 369 (2021) 88–94.

[92] Q. Wei, G. Yang, X. Gao, L. Tan, P. Ai, P. Zhang, P. Lu, Y. Yoneyama, N. Tsubaki, A facile ethanol fuel synthesis from dimethyl ether and syngas over tandem combination of Cu-doped HZSM35 with Cu-Zn-Al catalyst, Chem. Eng. J. 316 (2017) 832–841.

[93] C. Du, E. Hondo, L. Gapu Chizema, R. Hassan Ali, X. Chang, L. Dai, Q. Ma, P. Lu, N. Tsubaki, An efficient microcapsule catalyst for one-step ethanol synthesis from dimethyl ether and syngas, Fuel 283 (2021), 118971.

[94] X. Gao, B. Xu, G. Yang, X. Feng, Y. Yoneyama, U. Taka, N. Tsubaki, Designing a novel dual bed reactor to realize efficient ethanol synthesis from dimethyl ether and syngas, Catal. Sci. Technol. 8 (2018) 2087–2097.

[95] J. Kang, S. He, W. Zhou, Z. Shen, Y. Li, M. Chen, Q. Zhang, Y. Wang, Single-pass transformation of syngas into ethanol with high selectivity by triple tandem catalysis, Nat. Commun. 11 (2020) 827.

[96] S. Kasipandi, M. Ali, Y. Li, J.W. Bae, Phosphorus-modified mesoporous inorganic materials for production of hydrocarbon fuels and value-added chemicals, ChemCatChem 12 (2020) 4224–4241.

[97] Y.M. Park, M. Son, M.-J. Park, J.W. Bae, Effects of Pt precursors on Pt/CeO2 to water-gas shift (WGS) reaction activity with Langmuir-Hinshelwood model-based kinetics, Int. J. Hydrog. Energy 45 (2020) 26953–26966.

[98] J.M. Cho, B.G. Kim, G.Y. Han, J. Sun, H.K. Jeong, J.W. Bae, Effects of metal-organic framework-derived iron carbide phases for CO hydrogenation activity to hydrocarbons, Fuel 281 (2020), 118779.

[99] J.M. Cho, G.Y. Han, H.-K. Jeong, H.S. Roh, J.W. Bae, Effects of ordered mesoporous bimodal structures of Fe/KIT-6 for CO hydrogenation activity to hydrocarbons, Chem. Eng. J. 354 (2018) 197–207.

[100] A.J. Barrios, B. Gu, Y. Luo, D.V. Peron, P.A. Chernavskii, M. Virginie, R. Wojcieszak, J.W. Thybaut, V.V. Ordomsky, A.Y. Khodakov, Identification of efficient promoters and selectivity trends in high temperature Fischer-Tropsch synthesis over supported iron catalysts, Appl. Catal. B 273 (2020), 119028.

[101] F. Lu, X. Chen, Z. Lei, L. Wen, Y. Zhang, Revealing the activity of different iron carbides for Fischer-Tropsch synthesis, Appl. Catal. B 281 (2021), 119521.

[102] J. Wang, S. Huang, S. Howard, B.W. Muir, H. Wang, D.F. Kennedy, X. Ma, Elucidating surface and bulk phase transformation in Fischer–Tropsch synthesis catalysts and their influences on catalytic performance, ACS Catal. 9 (2019) 7976–7983.

[103] X.P. Fu, W.Z. Yu, C. Ma, J. Lin, S.Q. Sun, S.Q. Li, P.N. Ren, F.Y. Jia, M.Y. Li, W. W. Wang, X. Wang, C.J. Jia, K. Wu, R. Si, C.H. Yan, Supported Fe2C catalysts originated from Fe2N phase and active for Fischer-Tropsch synthesis, Appl. Catal. B 284 (2021), 119702.

[104] H. Liu, Y. Fu, M. Li, J. Wang, A. Noreen, E. Maturura, X. Gao, R. Yang, C.C. Amoo, C. Xing, Activated carbon templated synthesis of hierarchical zeolite Y-encapsulated iron catalysts for enhanced gasoline selectivity in CO hydrogenation, J. Mater. Chem. 9 (2021) 8663–8673.

[105] Z. Yang, Z. Zhang, Y. Liu, X. Ding, J. Zhang, J. Xu, Y. Han, Tuning direct CO hydrogenation reaction over Fe-Mn bimetallic catalysts toward light olefins: Effects of Mn promotion, Appl. Catal. B 285 (2021), 119815.

[106] Y.X. Zhang, X.Y. Guo, B. Liu, J.L. Zhang, X.H. Gao, Q.X. Ma, S.B. Fan, T.S. Zhao, Cellulose modified iron catalysts for enhanced light olefins and linear C$_5^+$ α-olefins from CO hydrogenation, Fuel 294 (2021), 120504.

[107] T.A. Wezendonk, X. Sun, A.I. Dugulan, A.J.F. van Hoof, E.J.M. Hensen, F. Kapteijn, J. Gascon, Controlled formation of iron carbides and their performance in Fischer-Tropsch synthesis, J. Catal. 362 (2018) 106–117.

[108] S. Lyu, L. Wang, Z. Li, S. Yin, J. Chen, Y. Zhang, J. Li, Y. Wang, Stabilization of ε-iron carbide as high-temperature catalyst under realistic Fischer–Tropsch synthesis conditions, Nat. Commun. 11 (2020) 6219.

[109] Y. Cheng, J. Tian, J. Lin, S. Wang, S. Xie, Y. Pei, S. Yan, M. Qiao, H. Xu, B. Zong, Potassium-promoted magnesium ferrite on 3D porous graphene as highly efficient catalyst for CO hydrogenation to lower olefins, J. Catal. 374 (2019) 24–35.

[110] Y.X. Zhang, X.Y. Guo, B. Liu, J.L. Zhang, X.H. Gao, Q.X. Ma, S.B. Fan, T.S. Zhao, Surface modification of g-C3N4-supported iron catalysts for CO hydrogenation: Strategy for product distribution, Fuel 305 (2021), 121473.

[111] J.S. Bae, S.Y. Hong, J.C. Park, G.B. Rhim, M.H. Youn, H. Jeong, S.W. Kang, J. I. Yang, H. Jung, D.H. Chun, Eco-friendly prepared iron-ore-based catalysts for Fischer-Tropsch synthesis, Appl. Catal. B 244 (2019) 576–582.

[112] Q. Cheng, Y. Tian, S. Lyu, N. Zhao, K. Ma, T. Ding, Z. Jiang, L. Wang, J. Zhang, L. Zheng, F. Gao, L. Dong, N. Tsubaki, X. Li, Confined small-sized cobalt catalysts stimulate carbon-chain growth reversely by modifying ASF law of Fischer–Tropsch synthesis, Nat. Commun. 9 (2018) 3250.

[113] C. Zhu, G.M. Bollas, Gasoline selective Fischer-Tropsch synthesis in structured bifunctional catalysts, Appl. Catal. B 235 (2018) 92–102.

[114] Y. Zhuo, L. Zhu, J. Liang, S. Wang, Selective Fischer-Tropsch synthesis for gasoline production over Y, Ce, or La-modified Co/H-β, Fuel 262 (2020), 116490.

[115] J. Hong, J. Du, B. Wang, Y. Zhang, C. Liu, H. Xiong, F. Sun, S. Chen, J. Li, Plasma-assisted preparation of highly dispersed cobalt catalysts for enhanced Fischer–Tropsch synthesis performance, ACS Catal. 8 (2018) 6177–6185.

[116] C. Liu, Y. He, L. Wei, Y. Zhang, Y. Zhao, J. Hong, S. Chen, L. Wang, J. Li, Hydrothermal carbon-coated TiO2 as support for Co-based catalyst in Fischer–Tropsch synthesis, ACS Catal. 8 (2018) 1591–1600.

[117] Q.X. Luo, L.P. Guo, S.Y. Yao, J. Bao, Z.T. Liu, Z.W. Liu, Cobalt nanoparticles confined in carbon matrix for probing the size dependence in Fischer-Tropsch synthesis, J. Catal. 369 (2019) 143–156.

[118] Z. Li, N. Yao, J. Cen, X. Li, L. Zhong, Y. Sun, M. He, Effects of alkali metal promoters on the structure–performance relationship of CoMn catalysts for Fischer–Tropsch synthesis, Catal. Sci. Technol. 10 (2020) 1816–1826.

[119] Q. Cheng, N. Zhao, S. Lyu, Y. Tian, F. Gao, L. Dong, Z. Jiang, J. Zhang, N. Tsubaki, X. Li, Tuning interaction between cobalt catalysts and nitrogen dopants in carbon nanospheres to promote Fischer-Tropsch synthesis, Appl. Catal. B 248 (2019) 73–83.

[120] Y. Zhang, X. Su, L. Li, H. Qi, C. Yang, W. Liu, X. Pan, X. Liu, X. Yang, Y. Huang, T. Zhang, Ru/TiO2 catalysts with size-dependent metal/support interaction for tunable reactivity in Fischer-Tropsch synthesis, ACS Catal. 10 (2020) 12967–12975.

[121] J. Liu, A. Zhang, X. Jiang, M. Liu, Y. Sun, C. Song, X. Guo, Selective CO2 hydrogenation to hydrocarbons on Cu-promoted Fe-based catalysts: Dependence on Cu–Fe interaction, ACS Sustain. Chem. Eng. 6 (2018) 10182–10190.

[122] J. Zhu, G. Zhang, W. Li, X. Zhang, F. Ding, C. Song, X. Guo, Deconvolution of the particle size effect on CO2 hydrogenation over iron-based catalysts, ACS Catal. 10 (2020) 7424–7433.

[123] J. Liu, A. Zhang, M. Liu, S. Hu, F. Ding, C. Song, X. Guo, Fe-MOF-derived highly active catalysts for carbon dioxide hydrogenation to valuable hydrocarbons, J. CO2 Util. 21 (2017) 100–107.

[124] Z. Shi, H. Yang, P. Gao, X. Li, L. Zhong, H. Wang, H. Liu, W. Wei, Y. Sun, Direct conversion of CO2 to long-chain hydrocarbon fuels over K-promoted CoCu/TiO2 catalysts, Catal. Today 311 (2018) 65–73.

[125] T. Lin, K. Gong, C. Wang, Y. An, X. Wang, X. Qi, S. Li, Y. Lu, L. Zhong, Y. Sun, Fischer–Tropsch synthesis to olefins: Catalytic performance and structure evolution of Co2C-based catalysts under a CO2 environment, ACS Catal. 9 (2019) 9554–9567.

[126] J. Wei, Q. Ge, R. Yao, Z. Wen, C. Fang, L. Guo, H. Xu, J. Sun, Directly converting CO2 into a gasoline fuel, Nat. Commun. 8 (2017) 15174.

[127] A. Noreen, M. Li, Y. Fu, C.C. Amoo, J. Wang, E. Maturura, C. Du, R. Yang, C. Xing, J. Sun, One-pass hydrogenation of CO2 to multibranched isoparaffins over bifunctional zeolite-based catalysts, ACS Catal. 10 (2020) 14186–14194.

[128] X. Wang, C.Y. Zeng, N. Gong, T. Zhang, Y. Wu, J. Zhang, F. Song, G. Yang, Y. Tan, Effective suppression of CO selectivity for CO2 hydrogenation to high-quality gasoline, ACS Catal. 11 (2021) 1528–1547.

[129] P. Gao, S. Li, X. Bu, S. Dang, Z. Liu, H. Wang, L. Zhong, M. Qiu, C. Yang, J. Cai, W. Wei, Y. Sun, Direct conversion of CO2 into liquid fuels with high selectivity over a bifunctional catalyst, Nat. Chem. 9 (2017) 1019–1024.

[130] P. Sharma, P.H. Ho, W. Di, D. Creaser, L. Olsson, Novel catalyst configuration to boost the yield of longer hydrocarbons from methanol-mediated CO2 hydrogenation, J. CO2 Util. 74 (2023), 102549.

[131] B. Yao, T. Xiao, O.A. Makgae, X. Jie, S. Gonzalez-Cortes, S. Guan, A.I. Kirkland, J. R. Dilworth, H.A. Al-Megren, S.M. Alshihri, P.J. Dobson, G.P. Owen, J. M. Thomas, P.P. Edwards, Transforming carbon dioxide into jet fuel using an organic combustion-synthesized Fe-Mn-K catalyst, Nat. Commun. 11 (2020) 6395.

[132] L. Zhang, Y. Dang, X. Zhou, P. Gao, A. Petrus van Bavel, H. Wang, S. Li, L. Shi, Y. Yang, E.I. Vovk, Y. Gao, Y. Sun, Direct conversion of CO2 to a jet fuel over CoFe alloy catalysts, Innovation 2 (2021), 100170.

[133] I. Nezam, W. Zhou, G.S. Gusmão, M.J. Realff, Y. Wang, A.J. Medford, C.W. Jones, Direct aromatization of CO2 via combined CO2 hydrogenation and zeolite-based acid catalysis, J. CO2 Util. 45 (2021) 101405.

[134] C. Dai, X. Zhao, B. Hu, J. Zhang, Q. Hao, H. Chen, X. Guo, X. Ma, Hydrogenation of CO2 to Aromatics over Fe−K/Alkaline Al2O3 and P/ZSM-5 Tandem Catalysts, Ind. Eng. Chem. Res. 59 (2020) 19194–19202.

[135] J. Wei, R. Yao, Q. Ge, D. Xu, C. Fang, J. Zhang, H. Xu, J. Sun, Precisely regulating Brønsted acid sites to promote the synthesis of light aromatics via CO2 hydrogenation, Appl. Catal. B 283 (2021) 119648.

[136] G. Song, M. Li, P. Yan, M.A. Nawaz, D. Liu, High Conversion to Aromatics via CO2-FT over a CO-Reduced Cu-Fe2O3 Catalyst Integrated with HZSM-5, ACS Catal. 10 (2020) 11268–11279.

[137] Y. Wang, S. Kazumi, W. Gao, X. Gao, H. Li, X. Guo, Y. Yoneyama, G. Yang, N. Tsubaki, Direct conversion of CO2 to aromatics with high yield via a modified Fischer-Tropsch synthesis pathway, Appl. Catal. B 269 (2020) 118792.

[138] X. Cui, P. Gao, S. Li, C. Yang, Z. Liu, H. Wang, L. Zhong, Y. Sun, Selective production of aromatics directly from carbon dioxide hydrogenation, ACS Catal. 9 (2019) 3866–3876.

[139] H. Tian, P. Gao, X. Yang, C. Jiao, F. Zha, Y. Chang, H. Chen, Tandem composite of M (Zn, Ga, In)-UIO-66/(HZSM-5)-palygorskite for hydrogenation of carbon dioxide to aromatics, Chem. Eng. J. 466 (2023), 143267.

[140] T. Wang, C. Yang, P. Gao, S. Zhou, S. Li, H. Wang, Y. Sun, ZnZrOx integrated with chain-like nanocrystal HZSM-5 as efficient catalysts for aromatics synthesis from CO2 hydrogenation, Appl. Catal. B 286 (2021), 119929.

[141] Q. Xin, H. Guo, Y. Wang, L. Xiao, W. Wang, W. Wu, Indium-promoted znZrOx/ nano-ZSM-5 for efficient conversion of CO₂ to aromatics with high selectivity, J. Environ. Chem. Eng. 10 (2022) 108032.

[142] X. Shang, G. Liu, X. Su, Y. Huang, T. Zhang, Preferential synthesis of toluene and xylene from CO₂ hydrogenation in the presence of benzene through an enhanced coupling reaction, ACS Catal. 12 (2022) 13741–13754.

[143] L. Zhang, W. Gao, F. Wang, C. Wang, J. Liang, X. Guo, Y. He, G. Yang, N. Tsubaki, Highly selective synthesis of light aromatics from CO₂ by chromium-doped ZrO₂ aerogels in tandem with HZSM-5@SiO₂ catalyst, Appl. Catal. B 328 (2023), 122535.

[144] K. Sun, M. Tan, Y. Bai, X. Gao, P. Wang, N. Gong, T. Zhang, G. Yang, Y. Tan, Design and synthesis of spherical-platelike ternary copper-cobalt-manganese catalysts for direct conversion of syngas to ethanol and higher alcohols, J. Catal. 378 (2019) 1–16.

[145] C. Göbel, S. Schmidt, C. Froese, Q. Fu, Y.-T. Chen, Q. Pan, M. Muhler, Structural evolution of bimetallic Co-Cu catalysts in CO hydrogenation to higher alcohols at high pressure, J. Catal. 383 (2020) 33–41.

[146] J. Yong, X. Luan, X. Dai, X. Zhang, Y. Yang, H. Zhao, M. Cui, Z. Ren, F. Nie, X. Huang, Alkaline-etched NiMgAl trimetallic oxide-supported KMoS-based catalysts for boosting higher alcohol selectivity in CO hydrogenation, ACS Appl. Mater. Interfaces 11 (2019) 19066–19076.

[147] Z. Ren, X. Zhang, X. Dai, X. Luan, Z. Yang, F. Nie, X. Yin, Y. Gan, Y. Cao, B. Wu, Ordered mesoporous NiMg bimetal oxides confined KMoS catalyst for selective CO hydrogenation into higher alcohols, Fuel 303 (2021), 121321.

[148] F. Zhang, Y. Li, S. Gao, H. Fang, X. Liang, Y. Yuan, Synthesis of higher alcohols by CO hydrogenation on a K-promoted Ni–Mo catalyst derived from Ni–Mo phyllosilicate, Catal. Sci. Technol. 8 (2018) 4219–4228.

[149] S. Fan, Y. Wang, Z. Li, Z. Zeng, D. Yao, S. Huang, X. Ma, Graphene oxide-ordered mesoporous silica composite supported Co-based catalysts for CO hydrogenation to higher alcohols, Appl. Catal. A 583 (2019), 117123.

[150] X. Xue, J. Yu, Y. Han, X. Xiao, Z. Shi, H. Mao, D. Mao, Zr-based metal–organic frameworks drived Rh–Mn catalysts for highly selective CO hydrogenation to C₂ oxygenates, J. Ind. Eng. Chem. 86 (2020) 220–231.

[151] P. Wang, S. Chen, Y. Bai, X. Gao, X. Li, K. Sun, H. Xie, G. Yang, Y. Han, Y. Tan, Effect of the promoter and support on cobalt-based catalysts for higher alcohols synthesis through CO hydrogenation, Fuel 195 (2017) 69–81.

[152] Y. Lu, R. Zhang, B. Cao, B. Ge, F.F. Tao, J. Shan, L. Nguyen, Z. Bao, T. Wu, J. W. Pote, B. Wang, F. Yu, Elucidating the copper–Hägg iron carbide synergistic interactions for selective CO hydrogenation to higher alcohols, ACS Catal. 7 (2017) 5500–5512.

[153] S. Gao, N. Liu, J. Liu, W. Chen, X. Liang, Y. Yuan, Synthesis of higher alcohols by CO hydrogenation over catalysts derived from LaCo₁₋ₓMnₓO₃ perovskites: Effect of the partial substitution of Co by Mn, Fuel 261 (2020), 116415.

[154] F. Zeng, X. Xi, H. Cao, Y. Pei, H.J. Heeres, R. Palkovits, Synthesis of mixed alcohols with enhanced C₃₊ alcohol production by CO hydrogenation over potassium promoted molybdenum sulfide, Appl. Catal. B 246 (2019) 232–241.

[155] S. Zhang, X. Liu, Z. Shao, H. Wang, Y. Sun, Direct CO₂ hydrogenation to ethanol over supported Co₂C catalysts: Studies on support effects and mechanism, J. Catal. 382 (2020) 86–96.

[156] S. Zhang, Z. Wu, X. Liu, Z. Shao, L. Xia, L. Zhong, H. Wang, Y. Sun, Tuning the interaction between Na and Co₂C to promote selective CO₂ hydrogenation to ethanol, Appl. Catal. B 293 (2021), 120207.

[157] L. Wang, L. Wang, J. Zhang, X. Liu, H. Wang, W. Zhang, Q. Yang, J. Ma, X. Dong, S.J. Yoo, J.-G. Kim, X. Meng, F.-S. Xiao, Selective hydrogenation of CO₂ to ethanol over cobalt catalysts, Angew. Chem. Int. Ed. 57 (2018) 6104–6108.

[158] L. Wang, S. He, L. Wang, Y. Lei, X. Meng, F.-S. Xiao, Cobalt–nickel catalysts for selective hydrogenation of carbon dioxide into ethanol, ACS Catal. 9 (2019) 11335–11340.

[159] L. Ding, T. Shi, J. Gu, Y. Cui, Z. Zhang, C. Yang, T. Chen, M. Lin, P. Wang, N. Xue, L. Peng, X. Guo, Y. Zhu, Z. Chen, W. Ding, CO₂ hydrogenation to ethanol over Cu@Na-Beta, Chem 6 (2020) 2673–2689.

[160] D. Xu, Y. Yang, X. Hong, G. Liu, S.C.E. Tsang, Tandem catalysis of direct CO₂ hydrogenation to higher alcohols, ACS Catal. 11 (2021) 8978–8984.

[161] F.J. Caparrós, L. Soler, M.D. Rossell, I. Angurell, L. Piccolo, O. Rossell, J. Llorca, Remarkable carbon dioxide hydrogenation to ethanol on a palladium/iron oxide single-atom catalyst, ChemCatChem 10 (2018) 2365–2369.

[162] R. Yao, J. Wei, Q. Ge, J. Xu, Y. Han, Q. Ma, H. Xu, J. Sun, Monometallic iron catalysts with synergistic Na and S for higher alcohols synthesis via CO₂ hydrogenation, Appl. Catal. B 298 (2021), 120556.